

(THE EFFECT FACTORS OF THE PILE INTEGRITY TEST)

by

Xiaoming Zhu

B.S. Tongzi University, 1982

M.S. Tongzi University, 1985

A THESIS

submitted in partial fulfillment of the
requirements for the degree

MASTER OF SCIENCE

Department of Civil Engineering
College of Engineering

KANSAS STATE UNIVERSITY

Manhattan, Kansas
1989

Approved by:



Major Professor

TABLE OF CONTENTS



A11208 617666

Chapter 1	1
Introduction and Literature Review	
Introduction	1
1. Background	1
2. Purpose and Scope	2
Literature Review	3
1. Analysis Model	3
2. Applications	4
3. Test Equipment and Measurement Techniques	6
4. Computer Program	8
Chapter 2	9
Finite Element Method	
Governing Equations	9
1. Equilibrium	9
2. Strain-Displacement Relation	10
3. Stress-Strain Relation	11
4. Surface-Traction-Stress Relation	11
5. Integration Over the Body	12
6. Divide the Body into Elements and Integrate Over each Element	13
7. Numerical Integration	14
8. Interface Element	17
9. Axisymmetric Formulations	18
10. Dynamic Solution	18
11. Computer Program	19
Chapter 3	20
Low Strain Integrity Testing of Bored Piles	
1. The Background	20
2. Field Test	22
3. Equipment	23
4. Test in Cleveland, Ohio	23

Chapter 4	25
Results and Discussions	
Results from One-Dimension Wave Propagation Analysis	25
1. Pile without Defects	25
2. Pile with Crack Section	26
3. Pile with Void	27
Results from Low Strain Integrity Test	28
1. Test at Newark, New Jersey	28
2. Test at Houston, Texas	29
3. Test at Cleveland, Ohio	30
Chapter 5	32
Analysis	
1. Wave Propagation in an Elastic Infinite Medium	32
2. Wave Propagation in a Semi-Infinite Elastic Half-Space	35
3. The Noise of the Surface Wave	40
4. The Effect of the Soil	42
5. The Effect of Defect Cross Area	43
6. Continuous Medium	44
Chapter 6	46
Conclusions and Recommendations	
List of Tables	48
List of Figures	49
List of References	53

ACKNOWLEDGMENTS

I wish to express my most sincere appreciation and thanks to Professor Wayne W. Williams for his advise and assistance.

I also wish to show my appreciation to Dr. Daniel Swenson for his patience in helping me with the computer program. Also Mr. Charles Berkel of Berkel Construction Company for making is possible to travel to Cleveland, Ohio to observe the pile testing and furnishing much data on projects in New Jersey and Texas.

I want to express my sincere thanks to Mrs. Doreen Smith for helping me come to Kansas State University and providing me with much support and friendship during my time here at the University.

The Effect Factors of the Pile Integrity Test

CHAPTER 1

Introduction and Literature Review

INTRODUCTION

1. Background

With the developing of modern industry, the pile foundation is used more widely and has gained popularity because of it's high bearing capacity, low settlement and ability to carry dynamic loads.

Since the pile is a structure which is embedded in the soil, the interaction between the pile and soil makes the analysis very complex both in theory and practice. In recent years a lot of research has been done in pile technology and a lot has been achieved but many problems still require solutions. The pile integrity test belongs to such kind of problems.

Deep foundation elements require definitive and economical test procedures that can be used shortly after or during construction to evaluate their structural integrity. Driven piles may be damaged due to high axial or bending stresses and bored augured piles may suffer from poor concrete quality, or construction workmanship which may create voids in the shaft. After installation the pile can be damaged by large lateral movement such as those caused by heavy equipment, slope failures or vibrations due to seismic or other activites. Various papers and articles, Feld, (7) 1968; Baker and Khan, (2) 1971; Reese and Wright, (19) 1977, report that at the presence of defects or irregularities within drilled piles that are detrimental to the performance of the foundation system. These papers list twelve conditions that may lead to defective drilled piles.

- 1) Excess water at cold joints resulting in weak concrete.
- 2) Migration of water, washing out of cement, or segregation resulting in weak concrete at the top of the shaft.

- 3) Side cave-in of soil resulting in contaminated concrete.
- 4) Surface cave-in of soil resulting in contaminated concrete.
- 5) Development of voids in the shaft.
- 6) Casing collapse.
- 7) Improperly poured tremie concrete.
- 8) Concrete poured into surface water.
- 9) Inadequate bell sizes
- 10) Inadequate bearing material
- 11) Squeeze in or necking of the shaft
- 12) Poor concrete delivered to the site.

Many methods have been developed for the quality control of piles but none are satisfactory in engineering practices. Some are very expensive, and some are not accurate. The need for further study of the problem became obvious during the field observation of low strain testing of piling constructed by Berkel Construction Co. in Cleveland, Ohio and observed by the author in December of 1988.

2. Purpose and Scope

In the United States bored piles are used widely and the low strain integrity test is a simple, rapid, and inexpensive method for testing the pile integrity. Unfortunately, this data is very difficult to analyse since many factors effect the accuracy of the test.

The purpose of this study is to develop analytical analysis of the low strain integrity test as applied to bored cast-in-place piling.

The scope of the study will consist of the development of a finite element analytical procedure which can be used in computer analysis. The analysis will concentrate on the effects of varying soil and pile factors which, at the present time, have an unknown effect and thus may aid in an accurate interpretation of the data.

LITERATURE REVIEW

Using the stress wave method to design pile is a new technology field. The principle is based on one dimensional wave propagation. In the last 20 years the theory developing very rapidly. The following literature review includes the following areas: Models, Applications, Tests and Computer Programs.

1. Analysis Models

St. Venant 1800 (24) was the first to analyse pile driving by using the one dimensional wave propagation. He developed the differential equation governing one dimensional wave propagation in an elastic rod and its solution. He provided the basis for insight into wave propagation problems but only for some limited boundary cases.

Isaacs 1931 (15) furthered the St. Venant's work giving the theory practical meaning specifically for the analysis of pile driving. Since there are numerous difficulties in describing a real hammer-pile-soil system, this effort had only limited success.

With the developing of the digital computer, a practical solution of the wave equation became possible. Smith 1960 (22) developed the original model using a mass-spring system. His work was one of the very first applications of the digital computer in the solution of mechanics problems. This first model did not consider the effect factors.

Hansen and Denver (3) developed the wave equation analysis of pile considering the mantle reaction and unhomogenous pile (a pile with a discontinuity in section area and/or material properties). This model is not supported by accepted test data.

H. Van Koten et.al., (14) suggested a model consisting of a parallel coupled spring and dashpot model schematizing the skin friction. The solution was used to determine the skin friction and the tip resistance. This model has been verified by little test data.

Y. K. Chow and I. M. Smith, (25) used a numerical model based on the finite element method using three dimensional axisymmetric in geometry, 8-node, quadratic isoparametric elements. Relative move-

ment between the pile and the soil driving during the driving process is modeled using 6-node slip elements. At the boundaries, viscous dash pots are introduced to enable the absorption of radialactivity stress waves.

The usage of this concept is expensive so it isn't practical for individual pile analysis. The paper considered only frictional soils, but it can model other soil behavior and aid in understanding the mechanics of pile driving.

D. Levacher and J. G. Siffert (5), used a model based on one dimensional wave equation. The equation is solved by a finite difference method. Their studies showed the influence of the resistance of the soil.

N. F. Febecker et.al., (17) presented a solution for dynamic non-linear soil structure interaction problems by the finite element method. Their studies show the displacement time-histories of pile to confirm certain soil resistances.

All these numerical methods have been developed in recent years and has opened the door to understanding the pile driving process but they are far from perfect at this time, since the problem is so very complicated.

2. Applications

a. Prediction of Bearing Capacity

The method is: To measure the pile top force and acceleration at time t_1 and t_2 , then the static bearing capacity is

$$S = R - D$$

R - soil resistance

$$R = \frac{1}{2}\{F(t_1) + F(t_2)\} + \frac{mc}{2L}\{V(t_1) - V(t_2)\}$$

t_1 - some selected time during the blow

$$t_2 = t_1 + \frac{2L}{c}$$

$$D = JV_{toe}$$

J - damping constant

V_{toe} = pile bottom velocity

$$V_{toe} = 2V(t_1) - \frac{L}{mc}R$$

This method is widely used and there is an abundance of data available for this procedure.

The accuracy of the indicated bearing capacity is well established but depends on the availability of accurate soil data and a reliable driving system.

b. Driveability

When all hammer-pile-soil parameters are given and the blow count is known then the pile stress can be predicted. The difficulty is the non-linear character of the soil. When blow counts are high (over 120 blows/per foot), a small error in the capacity estimate will produce a large change in the predicted blow count or vice versa.

c. Driving Stress

The driving stresses have been analysed by a number of different methods. The results of these methods vary widely and most of the methods are very sensitive to changes in the driving system parameters.

d. Driving System Performance

The force and velocity can be recorded and displayed on an oscilloscope (or on a computer's screen) and this visual display can be used for system performance control.

e. Control of Integrity

There are two methods to determine pile integrity; High Strain and Low Strain Method.

The High Strain Method is best for longer pile where the soil resistance become correspondingly larger and the damage is usually in the lower part of the pile, but the cost is much higher. Testing all piles for a large site is generally economically prohibitive since the pile must be struck by large mass, generally requiring contractor assistance and the vibration may effect other buildings which are near the site.

Low Strain Integrity Testing is a simple, economical quick, and reliable means for the structural integrity of all kinds of bored piles

and can be accomplished shortly after construction of the pile. It requires a high level of experience on the part of the engineer and the analytical procedure needs to be studied and improved.

The author went to Cleveland, Ohio last December to observe and study the Low Strain Test. The test was done by Goble Rausche Likins and Associates, Inc. which has 12-year experience in this field. It took almost 4 months to receive the test data. The results are very difficult to analyse and this method needs to be further studied and improved.

3. Test Equipment and Measurement Techniques

Although theoretical investigations concerning the propagation of stress waves in elastic solids date back to the end of the nineteenth century, it was only comparatively recent that technology became sophisticated enough to allow comparisons between experimental evidence and theory.

The first attempt to make dynamic stress measurement in pile driving was made by Glanville et.al., in 1938 (10). Strain measurements were made using piezoelectric force transducers on concrete piles and recorded on an oscilloscope. In 1940, Shear and Focke (21) performed ultrasonic velocity and wavelength measurements on polycrystalline silver, nickel, and magnesium cylinders dusted with lycopodium powder. The wavelength was determined by direct measurement of the standing wave pattern produced on the coated rods at resonance. By knowing the excitation frequency and resulting wave length, it was possible to compute the phase velocity in the cylinder. Shear and Focke concluded that the theoretical solution was sufficiently accurate for prediction of material velocities, provided that the wavelength of the stress wave is several times greater than the diameter of the rod.

Further evidence supporting the accuracy of theoretical solution of stress wave propagation was provided by Davies (4), (1948). Davies devised a pressure bar similar in principle to the Hopkinson bar, whereby continuous electronic measurements could be recorded if the longitudinal displacement produced by a pressure pulse at the

free end of a cylindrical bar. Davies concluded from his experiments that the velocities predicted in theory were in excellent agreement with velocities measured in the pressure bar.

In about 1960 Michigan Department of Highway [13] used specially designed force transducer to measure the force at the pile top and also added a strain gage accelerometer on the transducer. The data was recorded on a high speed oscillograph.

In 1964, Goble, Ransche and Likings (11)(18), began work in this field and continued it for the next 12 years. During this time, measurement techniques and equipment were developed and theoretical studies were performed. At the beginning they used resistance strain gages mounted directly on the wall of steel pipe piles. The resulting signal was amplified by an AC amplifier and recorded on a high speed oscillograph (2 m/s). Acceleration measurements were made using high impedance quartz crystal accelerometers. The measurements were good but it was difficult and time consuming to use. As developments occurred in electronics, the improvements were included in the equipment. Force transducers were developed of low enough weight that they can practically be brought to the job site. Strain transducers were developed – light weight and reusable. Amplifiers were developed using currents which are much easier to use. The processing was developed from Analog tape signal to digital signal, can be stored. Further analysis and plotting can be accomplished using a minicomputer.

Steinbach and Vey (23), (1975) conducted a laboratory investigation by performing tests on a 31.5 in (80 cm) long aluminum bar that was freely suspended horizontally. Steinbach and Vey found that the velocity predicted in theory was approximately four percent greater than the velocity measured in the aluminum.

Harrell and Stokoe (12), (1984) tested 4 drilled piles in Texas, using digital recording equipment. The receivers were embedded in the piles. These tests were designed to study the effects of the cross-sectional area of defects on wave propagation measurements. Usage of the wave attenuation is an important parameter in detecting

defective piers.

4. Computer Program

Computer programs have been developed by numerous groups. The more important among these are;

- a) The Raymond Company program (proprietary)
- b) The TTI program which is similar to the Raymond Program and not very different from Smith's original program.
- c) The WEAP program which contains an accurate diesel hammer model.
- d) DIESEL-1 by Rempe (proprietary)
- e) DUKFOR, a program that is similar to the TTI program but it contains a residual pile and soil stress analysis (proprietary)
- f) SWEAP, a combination of WEAP and DUKFOR (proprietary)

CHAPTER 2

Finite Element Method

(Two Dimensional Elasco-Dynamic Problems)

Governing Equations.

See Fig. 2.1, the plane in dynamic equilibrium at an instant in time in two-dimensional Euclidean space.

1. Equilibrium.

Take a small element look at forces in x direction $\Sigma F_x = ma_x$ (Fig. 2.2)

$$\begin{aligned} & -\sigma_{x|x} \cdot \Delta y + \sigma_{x|x+\Delta x} \cdot \Delta y \\ & -\tau_{xy|y} \cdot \Delta x + \tau_{xy|y+\Delta y} \cdot \Delta x = \rho \ddot{u}_x \end{aligned}$$

divide by Δx and Δy :

$$\begin{aligned} & \frac{\sigma_{x|x+\Delta x} - \sigma_{x|x}}{\Delta x} + \frac{\tau_{xy|y+\Delta y} - \tau_{xy|y}}{\Delta y} = \rho \ddot{u}_x \\ & \lim_{\Delta x, \Delta y \rightarrow 0} \frac{\partial \sigma_x}{\partial x} + \frac{\partial \tau_{xy}}{\partial y} = \rho \ddot{u}_x \end{aligned}$$

In y direction same we can got:

$$\frac{\partial \sigma_y}{\partial y} + \frac{\partial \tau_{xy}}{\partial x} = \rho \ddot{u}_y$$

ρ - density

u - displacement

\dot{u} - velocity

\ddot{u} - acceleration

If we use Indicjal Notation

$$\sigma_{ij,j} = \rho \ddot{u}_i \tag{2.1}$$

- 1) Indicjals: i, j, k run over the values $1, \dots, nsd$. two-dimensional $nsd = 2$.

- 2) Differentiation denoted by a comma.
- 3) Repeated indicials imply cummation.

2. Strain-Displacement Relation.

u – displacement in the x direction

v – displacement in the y direction.

Normal strain (Fig. 2.3)

$$\epsilon_x = \lim_{\Delta x \rightarrow 0} \left(\frac{u|_{x+\Delta x} - u|_{x,y}}{\Delta x} \right)$$

$$\epsilon_x = \frac{\partial u}{\partial x}$$

Then;

$$\epsilon_y = \frac{\partial v}{\partial y}$$

Shear strain (Fig. 2.4)

$$\begin{aligned} \alpha_x &= \frac{\partial v}{\partial x} \\ \alpha_y &= \frac{\partial u}{\partial y} \end{aligned}$$

the total change in angle is:

$$\theta_1 - \theta_2 = \alpha_x + \alpha_y$$

engineering shear strain $\gamma_{xy} = \alpha_x + \alpha_y = \frac{\partial v}{\partial x} + \frac{\partial u}{\partial y}$

$$\epsilon_{xy} = \frac{1}{2} \gamma_{xy}$$

$$\epsilon_{ij} = \frac{1}{2} (u_{i,j} + u_{j,i}). \quad (2.2)$$

3. Stress-Strain Relation.

Hooke's law

$$\begin{aligned}\epsilon_x &= \frac{1}{E}[\sigma_x - \gamma(\sigma_y)] \\ \epsilon_y &= \frac{1}{E}[\sigma_y - \gamma(\sigma_x)].\end{aligned}$$

E - Young's Modulus.

γ - Posson's Ratio.

Use Lamé's constant

$$G = \frac{E}{2(1 + \nu)} \quad \text{and} \quad \lambda = \frac{\nu E}{(1 + \nu)(1 - 2\nu)},$$

$$\sigma_x = 2G\epsilon_x + \lambda\epsilon$$

$$\sigma_y = 2G\epsilon_y + \lambda\epsilon$$

$$\tau_{xy} = 2G\epsilon_{xy}.$$

Combining the above three equations yields;

$$\sigma_{ij} = 2G\epsilon_{ij} + \lambda\epsilon\delta_{ij} \tag{2.3}$$

in which

$$\epsilon = \epsilon_x + \epsilon_y + \epsilon_z \quad \sigma_{xy} = \tau_{xy}$$

δ_{ij} is the Kronecker delta

$$\delta_{ij} = \begin{cases} 0 & i \neq j \\ 1 & i = j \end{cases}$$

4. Surface-Traction-Stress Relation.

See Fig. 2.5

Using the equilibrium in x direction. $\Sigma F_x = ma_x$

$$T_x \ell - \sigma_x \ell \cos \theta - \sigma_{xy} \ell \sin \theta = \rho \cdot \frac{1}{2}(\ell \cos \theta)(\ell \sin \theta)a_x$$

dividing by ℓ ;

$$T_x = \sigma_x \cdot \cos \theta + \sigma_{xy} \cdot \sin \theta + \rho \cdot \frac{1}{2}(\ell \cos \theta)(\sin \theta) \cdot a_x$$

Taking a limit as $\ell \rightarrow 0$

$$T_x = \sigma_x \cdot \cos \theta + \sigma_{xy} \cdot \sin \theta$$

in y direction then;

$$T_y = \sigma_{xy} \cdot \cos \theta + \sigma_y \cdot \sin \theta.$$

Since: $\cos \theta = n_x$ $\sin \theta = n_y$. Combining the above we obtain;

$$T_i = \sigma_{ij} \cdot n_j. \quad (2.4)$$

5. Integrating over the body.

Using the above relations we can integrate over the body. Recalling that

$$\sigma_{ij,j} = \rho \ddot{u}_i \quad (2.1)$$

(1) First multiply by an arbitrary weighting function (displacement) that is zero at boundary conditions.

$$\sigma_{ij,j} u_i = \rho \ddot{u}_i u_i.$$

Then

$$\int_{\Omega} \sigma_{ij,j} u_i d\Omega = \int_{\Omega} \rho \ddot{u}_i u_i d\Omega \quad (2.5)$$

(2) Using $\int_{\Omega} (\sigma_{ij} u_i)_{,j} d\Omega = \int_{\Omega} \sigma_{ij,j} u_i d\Omega + \int_{\Omega} \sigma_{ij} u_{i,j} d\Omega$ (2.5) becomes

$$\int_{\Omega} (\sigma_{ij} u_i)_{,j} d\Omega - \int_{\Omega} \sigma_{ij} u_{i,j} d\Omega = \int_{\Omega} \rho \ddot{u}_i u_i d\Omega. \quad (2.6)$$

(3) Applying the divergence theorem to (2.6)

$$\int_{\Omega} f_{i,i} d\Omega = \int_{\Omega} f_{i,n_i} d\Omega$$

$$\int_{\Omega} \sigma_{ij} u_{i,j} d\Omega - \int_{\Omega} \sigma_{ij} u_{i,j} d\Omega = \int_{\Omega} \rho \ddot{u}_i u_i d\Omega. \quad (2.7)$$

(4) Applying surface traction $T_i = \sigma_{ij} n_j$ into (2.7)

$$\int_S T u_i d\Omega - \int_{\Omega} \sigma_{ij} u_{i,j} d\Omega = \int_{\Omega} \rho \ddot{u}_i u_i d\Omega. \quad (2.8)$$

(5) Use the symmetry of the stress tensor

$$\sigma_{ij} = \sigma_{ji}$$

$$\frac{\sigma_{ij} u_{i,j}}{2} = \frac{\sigma_{ji} u_{i,j}}{2} = \frac{\sigma_{ij} u_{j,i}}{2}$$

$$\begin{aligned} \sigma_{ij} u_{i,j} &= \frac{1}{2} (\sigma_{ij} u_{i,j} + \sigma_{ij} u_{j,i}) \\ &= \sigma_{ij} \frac{1}{2} (u_{i,j} + u_{j,i}) = \sigma_{ij} \epsilon_{ij} \end{aligned}$$

Applying this to (2.8)

$$- \int_{\Omega} \sigma_{ij} \cdot \epsilon_{ij} \cdot d\Omega + \int_S T_i u_i \cdot ds = \int_{\Omega} \rho \ddot{u}_i u_i \cdot d\Omega \quad (2.9)$$

6. Divide the Body into Elements and Integrate Over Each Element.

At this point it's convenient to use matrix notation. The matrix is indicated by $[]$, vector is indicated by $'-'$.

For each element we assume the displacement to be functions of the values at the nodes over that element;

$$\underline{u} = [N] \underline{u}_a$$

then;

$$\underline{T} = [N] \underline{T}_a$$

\underline{u}_a is the nodal displacement

\underline{T}_a is the nodal surface traction.

The strains follow the equation (2.2)

$$\underline{\epsilon} = [B] \underline{u}_a$$

The stress follow the Hooke's law

$$\underline{\sigma} = [D]\underline{\epsilon}$$

Then;

$$\left\{ \int_S T_i u_i ds - \int_{\Omega} \sigma_{ij} \epsilon_{ij} d\Omega - \int_{\Omega} \rho \ddot{u}_i u_i d\Omega \right\} = 0$$

↓

$$\sum_{e=1}^N \left\{ \int_S \underline{u}^T \underline{T} ds - \int_{\Omega} \underline{\epsilon}^T \underline{\sigma} d\Omega - \int_{\Omega} \rho \underline{u}^T \ddot{\underline{u}} d\Omega \right\} = 0$$

↓

$$\begin{aligned} \sum_{e=1}^N \left\{ \int_S \underline{u}_a^T [N]^T [N] \underline{T}_a ds - \int_{\Omega} \underline{u}_a^T [B]^T [D] [B] \underline{u}_a d\Omega \right. \\ \left. - \int_{\Omega} \rho \underline{u}_a^T [N]^T [N] \ddot{\underline{u}}_a d\Omega \right\} = 0 \end{aligned}$$

\underline{u}_a is arbitrary and;

$$\sum_{e=1}^N \left\{ \int_S [N]^T [N] \underline{T}_a ds - \int_{\Omega} [B]^T [D] [B] \underline{u}_a d\Omega - \int_{\Omega} \rho [N]^T [N] \ddot{\underline{u}}_a d\Omega \right\} = 0 \quad (2.10)$$

7. Numerical Integration.

Up to now closed form integration has been used but this is difficult with computers and it is more convenient to use numerical integration. It is thus more convenient to pursue the following course of action;

(1) Choose an Element.

The choose six-noded triangle element is used. The reason is that we want to study the discontinuity in the pile. This means we need to develop an automatic remeshing scheme to move the crack tip. In general, it is easier to mesh an arbitrary region using triangular shapes than using quadrilateral shapes.

(2) "Natural" Coordinate System.

Using the natural coordinates, we can transform the original integral over the element in Cartesian space (close form) to an equivalent integral in the natural coordinate space (numerical). A standard triangular “natural” coordinate system is used, where each coordinate (r, s, t) is the ratio of the perpendicular distance to the height of a side. See Fig. 2.6.

Gauss Point	Natural Coord.			Weight
	r	s	t	
a	3/5	1/5	1/5	25/48
b	1/5	3/5	1/5	25/48
c	1/5	1/5	3/5	25/48
d	1/3	1/3	1/3	-27/48

These coordinates are symmetric with respect to the triangular geometry. The relationship between them is

$$r + s + t = 1$$

(3) Shape Functions.

Quadratic shape functions are used. Table 2.1 gave these functions and their derivatives.

Num.	Shape Functions	In terms of r and s ($r + s + t = 1$)	$\frac{\partial N}{\partial r}$	$\frac{\partial N}{\partial s}$
N1	$2r^2 - r$	$2r^2 - r$	$4r - 1$	0
N2	$2s^2 - s$	$2s^2 - s$	0	$4s - 1$
N3	$2t^2 - t$	$2r^2 + 2s^2 + 4rs - 3r - 3s + 1$	$4r + 4s - 3$	$4s + 4r - 3$
N4	$4rs$	$4rs$	$4s$	$4r$
N5	$4st$	$4s - 4rs - 4s^2$	$-4s$	$4 - 4r - 8s$
N6	$4tr$	$4r - 4rs - 4r^2$	$4 - 4s - 8r$	$-4r$

(4) Strain-Displacement Relations.

See $[B]$ in above equations.

$$\sum_{e=1}^N \int_{\Omega} [B]^T [D] [B] d\Omega \Rightarrow [K]$$

$$\begin{aligned}
U &= N_1 U_1 + N_2 U_2 + \cdots + N_6 U_6 \\
V &= N_1 V_1 + N_2 V_2 + \cdots + N_6 V_6 \\
\epsilon_x &= \frac{\partial u}{\partial x} \\
\epsilon_y &= \frac{\partial v}{\partial y} \\
\epsilon_{xy} &= \frac{\partial u}{\partial y} + \frac{\partial v}{\partial x}
\end{aligned}$$

$$\begin{Bmatrix} \epsilon_x \\ \epsilon_y \\ \epsilon_{xy} \end{Bmatrix} = \begin{bmatrix} \frac{\partial N_1}{\partial x} & 0 & \frac{\partial N_2}{\partial x} & 0 & \cdots & \frac{\partial N_6}{\partial x} & 0 \\ 0 & \frac{\partial N_1}{\partial y} & 0 & \frac{\partial N_2}{\partial y} & \cdots & \cdots & \frac{\partial N_6}{\partial y} \\ \frac{\partial N_1}{\partial y} & \frac{\partial N_1}{\partial x} & \frac{\partial N_2}{\partial y} & \frac{\partial N_2}{\partial x} & \cdots & \frac{\partial N_6}{\partial y} & \frac{\partial N_6}{\partial x} \end{bmatrix} \begin{Bmatrix} u_1 \\ v_1 \\ u_2 \\ v_2 \\ \vdots \\ u_6 \\ v_6 \end{Bmatrix}$$

\Downarrow
 B

(5) Jacobian.

Transfer to natural system.

$$\begin{Bmatrix} \frac{\partial N_1}{\partial \mathbf{r}} \\ \frac{\partial N_1}{\partial s} \end{Bmatrix} = \begin{bmatrix} \frac{\partial \mathbf{x}}{\partial \mathbf{r}} & \frac{\partial y}{\partial \mathbf{r}} \\ \frac{\partial \mathbf{x}}{\partial s} & \frac{\partial y}{\partial s} \end{bmatrix} \begin{Bmatrix} \frac{\partial N_1}{\partial \mathbf{x}} \\ \frac{\partial N_1}{\partial y} \end{Bmatrix}$$

\Downarrow
Jacobian.

(6) Numerical Integration.

$$\begin{aligned}
\int_{\Omega} [B]^T [D] [B] d\Omega &= \int_0^1 \int_0^{1-s} [B(r, s)]^T [D] [B(r, s)] \det J dr ds \\
&= \sum_{i=1}^N \sum_{j=1}^N [B(r_i, s_j)]^T [D] [B(r_i, s_j)] \det J(r_i, s_j) w_i w_j
\end{aligned}$$

The computer can do these operations very effectively.

8. Interface Element.

(1) Six-Noded Surface Element.

In many situations we want to model contact between bodies. One way to do that is to define an element having nodes on each body where a force-displacement rule is specified between pairs of nodes.

Fig 2.7 shows the six noded interface element and its numbering, Natural Coordinate, and weight is shown by the following:

Gauss Point	Natural Coord(s).	Weight
a	0.112702	5/18
b	0.5	8/18
c	0.88798	5/18

(2) Traction-Displacement Relation.

An “interface element” is a special case of surface tractions, where the surface tractions are prescribed as a function of nodal displacements. A typical multi-linear description of the normal traction for modeling a process zone is shown in Fig. 2.8. The response is linear in compression, but weakens after cracking.

(3) Geometry Relation.

See Fig. 2.9.

$$\begin{aligned} dL &= (dx^2 + dy^2)^{\frac{1}{2}} \\ dx &= \frac{\partial x}{\partial s} ds & dy &= \frac{\partial y}{\partial s} ds \\ dL &= \left[\left(\frac{dx}{ds} \right)^2 + \left(\frac{dy}{ds} \right)^2 \right] ds \\ &\Downarrow \\ &J \\ T_x &= P \cdot \frac{dy}{dL} = P \cdot \left(\frac{dy}{ds} \right) / J \\ T_y &= P \cdot \frac{dx}{dL} = P \cdot \left(\frac{dx}{ds} \right) / J \end{aligned}$$

(4) Numerical Integration.

$$\begin{aligned}\int_{se} [N][N] ds \underline{T}_a &= \int_{-1}^1 [N]^T [N] \det J ds \underline{T}_a \\ &= \sum_{i=1}^N [N(s_i)]^T [N(s_i)] \det J \underline{T}_a w_i\end{aligned}$$

9. Axisymmetric Formulations.

(1) An axisymmetric model is used in the integrity evaluation of bored piles by stress waves. Axisymmetric formulations are expressed in terms of cylindrical coordinates

r - the radial coordinate

z - the axial coordinate

ϕ - the circumferential coordinate

The basic hypothesis of axisymmetry is that all functions under consideration are independent of ϕ . That is, they are functions of r and z only. Thus three-dimensional problem classes are reduced to two-dimensional ones.

(2) The axisymmetric formulation for pile vibration is almost identical to the two-dimensional case considered previously. The only difference is that a factor of $2\pi r$ need to be included in each integrand of the variational equation to account for the correct volumetric weighting, e.g., $2\pi r dr dz$ replaces $dx dy$.

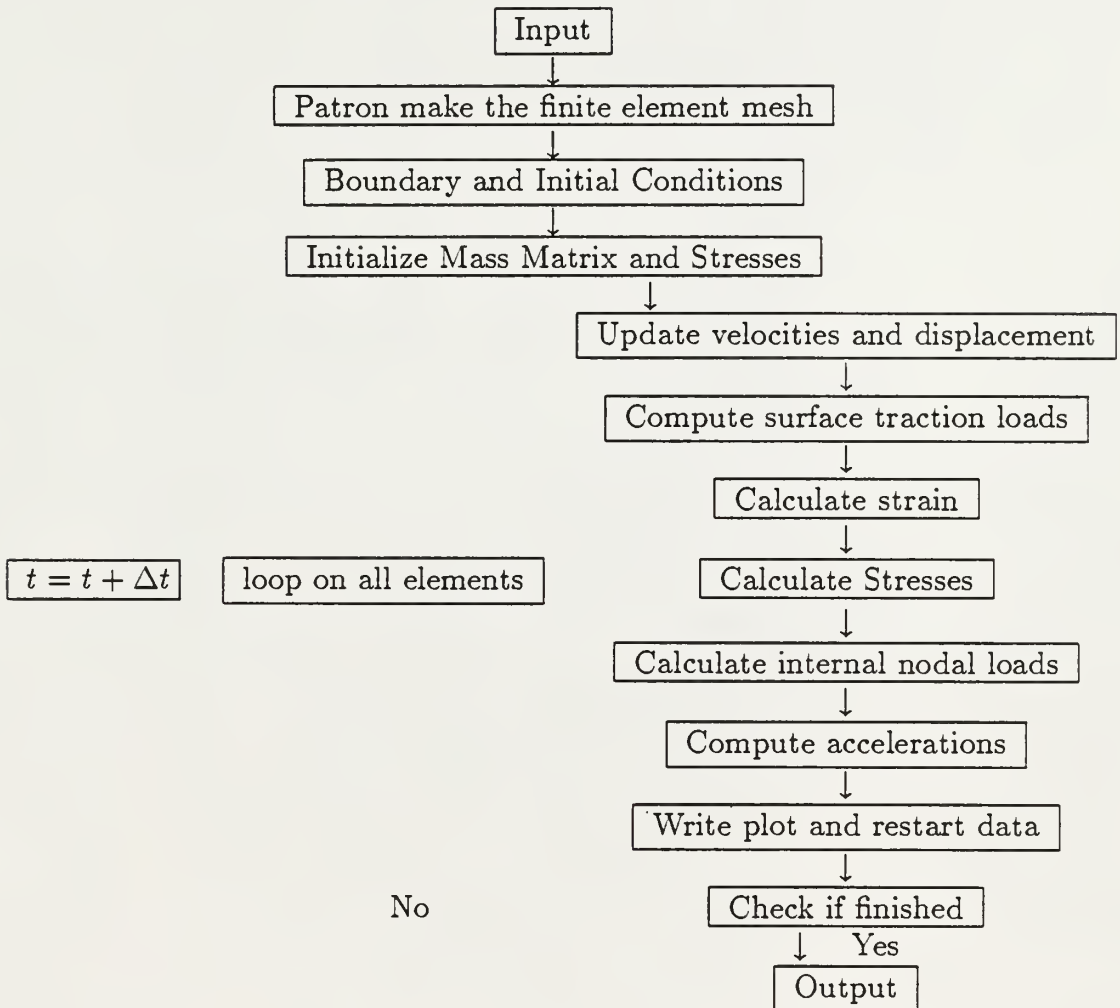
10. Dynamic Solution.

The explicit central difference approach is used. (Fig. 2.10)

$$\begin{aligned}\ddot{u}_n &= \frac{\dot{u}_{n+\frac{1}{2}} - \dot{u}_{n-\frac{1}{2}}}{\Delta t} \\ \dot{u}_{n+\frac{1}{2}} &= \dot{u}_{n-\frac{1}{2}} + \Delta t \cdot \ddot{u}_n \\ \dot{u}_{n+\frac{1}{2}} &= \frac{u_{n+1} - u_n}{\Delta t} \\ u_{n+1} &= u_n + \dot{u}_{n+\frac{1}{2}} \cdot \Delta t\end{aligned}$$

From the current state and previous solution the future velocities and displacements can be predicted.

11. Computer Program.



CHAPTER 3

Low Strain Integrity Testing of Bored Piles

1. The Background.

Up to now the basis for the low strain integrity testing has been the linear one-dimensional wave equation.

One-dimensional wave equation.

The pile is assumed to be an elastic rod. (See Fig. 3.1.) It is assumed that each cross section remains plane during motion and the stress is uniform over the area. The stress on a transverse plane at x is σx and the stress on a transverse plane at $x+dx$ is $\sigma x + \frac{\partial \sigma x}{\partial x} dx$.

According to Newton's second law,

$$-\sigma x A + \sigma x A + \frac{\partial \sigma x}{\partial x} dx \cdot A = dx \cdot A \frac{\gamma}{g} \frac{\partial^2 u}{\partial t^2} \quad (3.1)$$

$$\frac{\partial \sigma x}{\partial x} = \frac{\gamma}{g} \frac{\partial^2 u}{\partial t^2} \quad (3.2)$$

u - the displacement of the element in the x direction

g - acceleration due to gravity

γ - unit weight

A - cross-section area.

$$\text{According to Hooke's law: } \sigma x = E \frac{\partial u}{\partial x} \quad (3.3)$$

in which E - Young's modulus then $\frac{\partial \sigma x}{\partial x} = E \frac{\partial^2 u}{\partial x^2}$.

Let the mass density $\rho = \frac{\gamma}{g}$. Put 3.3 and ρ into 3.2

$$E \frac{\partial^2 u}{\partial x^2} = \rho \frac{\partial^2 u}{\partial t^2}$$

$$\frac{\partial^2 u}{\partial t^2} = \frac{E}{\rho} \frac{\partial^2 u}{\partial x^2} \text{ or } \frac{\partial^2 u}{\partial t^2} = V_p^2 \frac{\partial^2 u}{\partial x^2}$$

in which $V_p^2 = \frac{E}{\rho}$.

V_p is defined as the Longitudinal-wave-propagation velocity.

The solution to the wave equation developed for the infinite elastic rod can be written in the form

$$u = f(V_p t + x) + h(V_p t - x) \quad (3.4)$$

where f and h are arbitrary functions depending on the initial boundary conditions (Timoshenko and Goodier, 1934, (24)).

Boundary Conditions

The theory that has been developed is based on the stress wave propagate in infinite elastic rods. However, drilled piles have finite lengths and therefore, to apply the wave equation theory to the study of drilled piles, boundary conditions must be imposed on the general solution.

When an elastic rod of finite length is subjected to an impulse at one end, a stress wave is generated that travels the length of the rod at the velocity of V_p . As the vibrational wave reaches the end of the rod, the stress wave is reflected. The nature of the wave reflection is dependent on conditions at the end of the rod. Kolsky (1963), (26) presents the theoretical study of wave propagation in finite rods by applying various boundary conditions to the wave equation.

Though the piles are embedded in soil, the boundary conditions are close to free end conditions.

From Equation (3.4) the displacement due to the incident wave is represented by:

$$\begin{aligned} u_1 &= f(V_p t + x) \\ u_2 &= h(V_p t - x) \end{aligned}$$

The stresses will be:

$$E\{f'(V_p t + x) - h'(V_p t - x)\}$$

Here $f'(V_p t + x)$ is the differentiation of function f in x direction. So $f'(V_p t + x)$ is the strain in x direction.

At the free end of the rod the normal stress is zero, we get:

$$f'(V_p t) - h'(V_p t) = 0$$

this states that the shape of the reflected wave is the same as that of incident wave but is of the opposite sign. So a compression wave will be reflected from the free end of a rod as a tension wave identical magnitude and shape. Similarly, a tension wave propagating in an elastic rod will be reflected from a free end as a compression wave of the same magnitude and shape.

2. Field Test.

The compressive wave is created by the blow of a hand-held impact hammer. If the pile is uniform the compression wave travels unchanged and axially through the shaft from the pile top to the pile tip and is reflected back to the top. The direction of travel is identical with the direction of the particles motions in the compressive waves but is opposite to that of the tensile waves. The travel time of the wave is measured from the first maximum peak to the peak of the pile tip reflection,

$$T = \frac{2L}{V_p}$$

L - the length of the pile.

If the pile isn't uniform, if there exists an irregularity in the pile shaft, then when the downward traveling wave arrives at this point, part of the wave is reflected up and part transmitted down, therefore additional signals are recorded before the first reflection wave from the pile tip.

A decrease in either area A or modulus E produces a tension reflection, an increase in either of these produces a compressive reflection.

3. Equipment.

The basic test equipment for integrity testing are the impact device, receiver, recorder, signal conditioning, and the equipment for the analysis and plotting.

Impact Device

In most cases a hand-held hammer is used.

Receiver

The piezoelectric accelerometers are used. These accelerometers are of high natural frequency and sensitivity, for the acceleration of the impact is low.

Recorder

A magnetic tape or a storage oscilloscope is used.

Signal Conditioning

Further analysis and plotting can be done by using a computer and a variety of peripheral devices after analog-to-digital conversion of the recorded signals.

The equipment must be capable of providing signals with frequency of up to 5 kHz. It is desirable to integrate the acceleration to velocity immediately. This is done by the Pile Driving Analyzer-PDA.

The proceeding see Fig. 3.2 and Fig. 3.3.

4. Test in Cleveland, Ohio

a. Pile data:

The pile's diameter is 12 in (0.3048 m)

The pile's length is 30 ft. (9.14 m)

Plain concrete pile with unconfined compressive strengths in the range of 4000 psi.

b. Test process:

The whole test process is shown from Fig. 3.4 to Fig. 3.13.

The first step was the measurements in the field to locate the pile (Fig. 3.4). Then the piles were bored (Figure 3.5) to excavate the

bore holes. After completing the bore hole (Fig. 3.6), the concrete was emplaced using a concrete mixer (Fig. 3.7) to form the pile (Fig. 3.8). Fig. 3.9 shows the formed piles used for testing with the surface of the piles made smooth and planar for testing (Fig. 3.10). The Honda generator was used as a power supply (Fig. 3.11). A hand hammer was used to impact the pile (Fig. 3.12) producing the wave. The PDA (pile dynamic analysis) and computer were used to record and plot the test results (Fig. 3.13).

CHAPTER 4

Results and Discussions

Results from One-Dimension Wave Propagation Analysis.

PATRAN was used to mesh the pile as shown in Figure 4.1. The pile's diameter was taken as 12 in. (0.3048 m) and the length as 30 ft. (9.144 m), which is the same as the piles tested in Cleveland, Ohio. The finite elements are shown in Figure 4.2. These are triangular elements, 3.6 in (9.14 cm) in the Y direction and 3 in (7.62 cm) in the X direction. An axisymmetric case is used. The displacement boundary condition are shown in Figure 4.3. Along the central line X direction is fixed and Y direction is free. The impulse is depicted in Figure 4.4. The period of impulse should match the size of the finite element.

The pile was assumed to have a Young's modulus of $57,000 \sqrt{f'_c}$ and a value of 4000 psi (27579 kN/m^2) was used for the compressive strength of the concrete. This results in a value of 3.6410^6 psi ($124.8 \times 10^6 \text{ kN/m}^2$)

The unit weight of concrete accepted is 145 psf (6.94 kN/m^2), then the density of the concrete is 0.00022473 pci (6.22 kg/m^3) and one-dimension wave propagation, $\nu = 0$.

1. Pile without Defects:

a. Response at the Top of the Pile:

The response at the top of the pile is shown in Figure 4.5.

The first peak is caused directly by the impulse. The second peak appears when the reflection from the bottom of the pile is received. The impulse produces a compression wave traveling in the negative Y -direction. When the wave arrives at the bottom of the pile, which is a free end, the compression wave is reflected upward as a tension wave traveling in the positive Y -direction. When this wave arrives at the top of the pile, the tension wave is again reflected as a compression wave. The top of the pile is a crossover zone, in which two waves pass each other. According to wave propagation, the particle velocity in a tension wave is opposite to the direction of wave travel.

but the particle velocity in a compression wave is in the direction of wave travel. Since the compression and tension waves are traveling in opposite directions at the top of the pile, the particle velocities associated with both waves are additive and the particle velocity on the top equals twice the particle velocity in either wave. The second peak in Figure 4.5 is thus twice as the first peak.

b. Response at the Mid-Point of the Pile:

As shown in Figure 4.6 and Figure 4.7 the node number 255 is 5 ft (1.524 m) below the top and the node number 55 is 5 ft (1.524 m) above the pile tip. The first peak is a compression wave caused by the impulse and the second peak is a tension wave reflected from the bottom. Before the waves arrived and after the wave passed the particle velocity is zero. After passing the crossover point, both compression and tension waves return to their initial shape and magnitude. The response at the down middle point is shown in Figure 4.7.

c. Response at the Bottom of the Pile:

The response at the bottom of the pile is shown in Figure 4.8. The bottom of the pile is another crossover zone. The compression wave is reflected as a tension wave. The particle velocity is again equal twice as either wave.

2. Pile with Cracked Section:

The crack was assumed to be in the middle of the pile as shown in Figure 4.9. The mesh of the crack is shown in Figure 4.10.

The response on the top of the pile is shown in Figure 4.11 The first peak is caused by the impulse. The compression wave is reflected by the crack as a tension wave. The tension wave is then reflected to the top boundary as a compression wave forming a second peak. The third peak is received when a part of the compression wave is reflected from bottom to the top of the pile.

The response in the pile above the crack is shown in Figure 4.12. The second peak is the first reflection of the wave from the crack and the third peak is the second reflection from the crack. The response

at the crack is shown in Figure 4.13. The second peak is received by both: the part of the wave reflected at the crack and the part reflected at the bottom.

The response in the pile below the crack is shown in Figure 4.14. The third peak is reflected directly from the crack. The response at the bottom of the pile is shown in Figure 4.15. The second peak is the reflection from the crack.

3. Pile with Void:

The mesh of the void is shown in Figure 4.16. The void is 10.2 ft (3.1 m) below the top of the pile. The cross-area of the void is equal to one half the total area of the pile.

The response on the top of the pile is shown in Figure 4.17. The first peak is caused by the impulse and the second peak is caused by a reflection wave from the void. When the compression wave meets the upside of the void, part of the wave is reflected upward as a tension wave (the upside of the void is a free end) and part of the wave is retracted downward as a compression wave. When the compression wave meets the downside of the void, which is a fixed end it's reflected as a compression wave. Thus the second peak has a velocity in both positive Y direction and negative Y directions. The third peak is caused by both the tension and the compression waves reflection at the void boundary the second time.

The response at the upside of the void is shown in Figure 4.18. Response at the downside of the void is shown in Figure 4.19. The first peak appears when the compression wave produced by impulse passes the void and the second peak is the reflection at the void boundary. The third peak is the second reflection at the void boundary and the fourth peak is the reflection that came from the bottom.

The response at the bottom of the pile is shown in Figure 4.20. The first peak appears when the compression wave caused by the impulse arrives at the bottom. The second and third peak are reflections from the void.

Result from Low Strain Integrity Test

1. Tests at Newark, New Jersey

The 24 drilled piles were tested in Newark, NJ using the low strain integrity test method. The impact source is a hand held hammer which weighed 10 lb (4.54 kg). The receiver is an accelerometer which was placed on the top of the pile. The piles diameter was 18" (0.4572 m) and the piles length was 45 ft (13.716 m). The surrounding soil conditions are shown in Figure 4.21 and 4.22.

The test record for the pile 41 is shown in Figure 4.23. The reflection depth is equal to; (compression wave velocity * reflection arrival time)/2.

$$b = (V_p * t)/2$$

Assuming $V_p = 12,000$ fps (3657.6 m/s)

The first reflection arrival was at $t = 4.7$ ms. Then $b = 12,000 \times 4.7/2 = 28$ ft (8.13 m) which is the depth of reflection from defect.

The second reflection arrival was at $t = 26$ ms thus, $b = 12,000 \times 7.6/2 = 46$ ft (14.02 m) which is the estimated length of a pile.

The test record for pile 47 is shown in Figure 4.24 the reflector depth calculations are the same as that for pile 41. The first reflection came from a defect at a depth of 16 ft (4.88 m) and the second reflection came from the tip of the pile at depth 46 ft (14.02 m).

The test record for pile 50 is shown in Figure 4.25. The first reflection came from a defect at a depth of 10 ft (3.048 m) and the second reflection came from tip of pile at depth 49 ft. (14.94 m).

The test record for pile 125 is shown in Figure 4.26 which was a pile without defects. The deflection came from tip of pile at depth 47 ft. (14.33 m).

The test record for pile 128 is shown in Figure 4.27. The first reflection came from a defect at a depth of 16 ft (4.88 m) and the second reflection came from tip of pile at depth 43 ft (13.11 m).

The test record for pile 130 is shown in Figure 4.28 which was a pile without defects. The reflection came from the tip of pile at depth 46 ft (14.02 m).

From these results we can see the reflection peaks are less clear than those obtained from the theory. The ones chosen were felt to be the best curves from the lot of test data. Most of the curves were impossible to interpret, see Figure 4.29.

2. Test at Houston, Texas:

The test location is shown in Figure 4.30. The surrounding soil conditions are shown in Figure 4.31. The pile dimensions are shown in Figure 4.32 to be; 2.5 ft (0.762 m) in diameter and 50 ft (15.24 m) in length. Pile A is a sound pile and pile B has a defect at middle which has a 1/4 section of the cross sectional area. Pile C has a defect at the middle which reduces the cross sectional area by a half. Pile D has defect at middle which interrupts the whole cross-area. The test records are shown in the following figures;

Pile A see Figure 4.33

Pile B see Figure 4.34

Pile C see Figure 4.35 and Figure 4.36

Pile D see Figure 4.37

Wave propagation measurements on pile A used a velocity transducer (natural frequency of 8-Hz) as the surface receiver. The test was generated using a 15 lb (6.8 kg) drop hammer. The receiver output was filtered at 2.5 kHz low pass.

Wave propagation measurement on pile B and D made use of an accelerometer surface receiver and a drop hammer source, and was filtered at 1.8 kHz low pass.

Wave propagation measurements on pile C used two sources: one is drop hammer 15 lb (6.8 kg) the output see Figure 4.35 and the other is hand hammer 5 lb (2.3 kg) the output see Figure 4.36. The accelerometer was used as a surface receiver and it was filtered at 2-kHz low pass.

From these test results we can see that:

- a. Test measurements using a velocity transducer as the surface receiver proved to be less successful.

- b. Test output using a lighter hand hammer as the impact source proved to be less successful.
- c. With smaller defect cross-area the reflection peak from the defect is smaller.

3. Test at Cleveland, Ohio:

Integrity tests were performed on 136 auger cast piles. The testing is performed by affixing a high sensitivity accelerometer to the pile top and then striking the pile with a hand held hammer. Other hardware used were an accelerometer power supply, amplifier, and a portable computer capable of converting analog data to digital form.

The acceleration record created from each hammer impact was integrated to velocity and displayed on the PC console and digitally stored for later reprocessing.

An amplification routine is used to amplify wave reflections which are weak due to pile and soil damping.

The output is the average of several records to separate the effects of random noise.

The stress wave speed for all piles was assumed to be 12,500 ft/s.

The piles tested were 12 in. (0.3048 m) diameter auger cast concrete piles with a designed length of 30 ft. (9.14 m).

The subsurface conditions can be generally described as variable soils which include fill (upper 5 ft.), medium dense silts, loose to firms sands and soft to very stiff clays.

The test record for pile A1.EAST (see Figure 4.38) indicates a sound pile. The length is 32 ft. (9.75 m).

The test record for pile C1.EAST (see Figure 4.39) indicates that the pile has a crack at the 5 ft. (1.5 m) level.

The test record for pile E1.EAST (see Figure 4.40) indicates that there is a 15% area reduction at 8 ft. (2.4 m).

The test record for pile A4.3A (see Figure 4.41) indicates that there are reductions in pile diameter at 6 ft. (1.8 m) and 10 ft. (3.048 m). From these test results we can see after the first peak caused by hammer impact that the signal received at the top travels

downward. The amplification routine is helpful, otherwise the second peak reflected from the bottom of the pile would be very weak.

Questions raised by these data are:

1. The differences between the results from theory and test?
2. Which factors effected these differences?

These questions are addressed in Chapter V.

CHAPTER 5

Analysis

The Propagation of Stress Wave in Pile-Soil System.

Since the pile is embedded in soil, the propagation of stress wave in a pile is different from the propagation of stress wave in a rod. First examining the wave propagation in an elastic infinite medium suitable equations can be derived.

1. Wave Propagation in an Elastic Infinite Medium.

The wave propagation was described in Chapter 2. Using equilibrium of force and Newton's second law in x, y, z directions. We can get

$$\rho \frac{\partial^2 u}{\partial t^2} = \frac{\partial \sigma_x}{\partial x} + \frac{\partial \tau_{xy}}{\partial y} + \frac{\partial \tau_{xz}}{\partial z} \quad (5-1a)$$

$$\rho \frac{\partial^2 v}{\partial t^2} = \frac{\partial \tau_{yx}}{\partial x} + \frac{\partial \sigma_y}{\partial y} + \frac{\partial \tau_{yz}}{\partial z} \quad (5-1b)$$

$$\rho \frac{\partial^2 w}{\partial t^2} = \frac{\partial \tau_{zx}}{\partial x} + \frac{\partial \tau_{zy}}{\partial y} + \frac{\partial \sigma_z}{\partial z} \quad (5-1c)$$

in which u, v , and w are displacements in the x, y , and z directions, respectively. The relationship between strain and stress for elastic medium:

$$\sigma_x = \lambda \bar{\epsilon} + 2G\epsilon_x \quad \tau_{xy} = \tau_{yx} = G\gamma_{xy} \quad (5-2a)$$

$$\sigma_y = \lambda \bar{\epsilon} + 2G\epsilon_y \quad \tau_{yz} = \tau_{zy} = G\gamma_{yz} \quad (5-2b)$$

$$\sigma_z = \lambda \bar{\epsilon} + 2G\epsilon_z \quad \tau_{zx} = \tau_{xz} = G\gamma_{zx} \quad (5-2c)$$

$$G = \frac{E}{2(1 + \nu)} \quad (5-3a)$$

$$\lambda = \frac{\nu E}{(1 + \nu)(1 - 2\nu)} \quad (5 - 3b)$$

in which

ν - Poisson's ratio

λ, G - Lamé's constants

and G is the shear modulus

$$\bar{\epsilon} = \epsilon_x + \epsilon_y + \epsilon_z.$$

The relationship between strains and displacements

$$\epsilon_x = \frac{\partial u}{\partial x} \quad \gamma_{xy} = \frac{\partial v}{\partial x} + \frac{\partial u}{\partial y} \quad (5 - 4a)$$

$$\epsilon_y = \frac{\partial v}{\partial y} \quad \gamma_{yz} = \frac{\partial w}{\partial y} + \frac{\partial v}{\partial z} \quad (5 - 4b)$$

$$\epsilon_z = \frac{\partial w}{\partial z} \quad \gamma_{zx} = \frac{\partial u}{\partial z} + \frac{\partial w}{\partial x} \quad (5 - 4c)$$

The relationship between rotations and displacements

$$2\bar{\omega}_x = \frac{\partial w}{\partial y} - \frac{\partial v}{\partial z} \quad (5 - 5a)$$

$$2\bar{\omega}_y = \frac{\partial u}{\partial z} - \frac{\partial w}{\partial x} \quad (5 - 5b)$$

$$2\bar{\omega}_z = \frac{\partial v}{\partial x} - \frac{\partial u}{\partial y} \quad (5 - 5c)$$

Where $\bar{\omega}_x, \bar{\omega}_y$, and $\bar{\omega}_z$ are rotations about x, y , and z axes respectively.

Substituting (5-2), (5-3), (5-4), and (5-5) into (5-1), we get

$$\rho \frac{\partial^2 u}{\partial t^2} = (\lambda + G) \frac{\partial \bar{\epsilon}}{\partial x} + G \nabla^2 u \quad (5 - 6a)$$

$$\rho \frac{\partial^2 v}{\partial t^2} = (\lambda + G) \frac{\partial \bar{\epsilon}}{\partial y} + G \nabla^2 v \quad (5 - 6b)$$

$$\rho \frac{\partial^2 w}{\partial t^2} = (\lambda + G) \frac{\partial \bar{\epsilon}}{\partial z} + G \nabla^2 w \quad (5-6c)$$

where ∇^2 is the Laplacian operator in Cartesian coordinates:

$$\nabla^2 = \left(\frac{\partial^2}{\partial x^2} + \frac{\partial^2}{\partial y^2} + \frac{\partial^2}{\partial z^2} \right)$$

There are two solutions for the above equation. One solution describes the propagation of an irrational wave while the other describes the propagation of a wave of pure rotation. Differentiating eqs. (5-6) with respect to x, y and z respectively and adding all three expressions together, we get:

$$\rho \frac{\partial^2 \bar{\epsilon}}{\partial t^2} = (\lambda + 2G) \nabla^2 \bar{\epsilon} \quad (5-7)$$

using

$$v_c^2 = \frac{\lambda + 2G}{\rho} \quad (5-8)$$

which is exactly the form of wave eqs.

$$\frac{\partial^2 \bar{\epsilon}}{\partial t^2} = v_p^2 \nabla^2 \bar{\epsilon} \quad (5-9)$$

Substituting (5-3) into (5-8) we get the velocity of compression waves in the infinite medium

$$v_p^2 = \frac{E(1 - \nu)}{\rho(1 + \nu)(1 - 2\nu)} \quad (5-10)$$

The other solution of the equations for motion can be obtained by differentiating eq. (5-6b) with respect to z and eq. (5-6c) with respect to y and then eliminating $\bar{\epsilon}$ by subtracting these two equations we get

$$\rho \frac{\partial^2}{\partial t^2} \left(\frac{\partial w}{\partial y} - \frac{\partial v}{\partial z} \right) = G \nabla^2 \left(\frac{\partial w}{\partial y} - \frac{\partial v}{\partial z} \right) \quad (5-11)$$

using eq. (5-5a) we get:

$$\rho \frac{\partial^2 \bar{w}_x}{\partial t^2} = G \nabla^2 \bar{w}_x \quad (5 - 12)$$

using

$$V_s^2 = \sqrt{\frac{G}{\rho}} \quad (5 - 13)$$

$$\frac{\partial^2 \bar{w}_x}{\partial t^2} = V_s^2 \nabla^2 \bar{w}_x \quad (5 - 14)$$

This is the exact wave form equation also, so v_s is the velocity of shear wave.

2. Wave Propagation in a Semi-Infinite Elastic Half Space.

Since piles are supported on the soil, the boundary conditions approximating this situation are those of a semi-infinite half space. If the medium is assumed homogeneous, isotropic and elastic, it is found that there are two types of body waves – the compression wave and the shear wave. In an elastic half space, it will be seen that another wave, the Rayleigh wave appears. The motion of a Rayleigh wave is confined to a zone near the boundary of the half space. The solution for this wave was first obtained by Rayleigh (1885) and later described in detail by Lamb (1904).

The half space can be defined as a xy plane with z assumed positive in the downward direction (Fig. 5.1). For a plane wave traveling in the x direction, particle displacement is independent of y direction

$$\frac{\partial u}{\partial y} = \frac{\partial w}{\partial y} = 0$$

and $v = 0$. Then, if the body force is neglected, we get the equations same with (5-6a) and (5-6c).

$$(\lambda + G) \frac{\partial \bar{\epsilon}}{\partial x} + G \nabla^2 u = \rho \frac{\partial^2 u}{\partial t^2} \quad (5 - 6a)$$

$$(\lambda + G) \frac{\partial \bar{\epsilon}}{\partial z} + G \nabla^2 w = \rho \frac{\partial^2 w}{\partial t^2} \quad (5 - 6c)$$

u and w can be written in terms of two potential functions Φ and ψ :

$$u = \frac{\partial \Phi}{\partial x} + \frac{\partial \psi}{\partial z} \quad (5-15a)$$

$$w = \frac{\partial \Phi}{\partial z} - \frac{\partial \psi}{\partial x} \quad (5-15b)$$

The dilatation $\bar{\epsilon}$ of the wave defined by u and w is:

$$\begin{aligned} \bar{\epsilon} &= \frac{\partial u}{\partial x} + \frac{\partial w}{\partial z} = \frac{\partial}{\partial x} \left(\frac{\partial \Phi}{\partial x} + \frac{\partial \psi}{\partial z} \right) + \frac{\partial}{\partial z} \left(\frac{\partial \Phi}{\partial z} - \frac{\partial \psi}{\partial x} \right) \\ &= \nabla^2 \Phi \end{aligned}$$

and the rotation $2\bar{\omega}_y$ in the $x - z$ plane is

$$\begin{aligned} 2\bar{\omega}_y &= \frac{\partial u}{\partial z} - \frac{\partial w}{\partial x} = \frac{\partial}{\partial z} \left(\frac{\partial \Phi}{\partial x} + \frac{\partial \psi}{\partial z} \right) - \frac{\partial}{\partial x} \left(\frac{\partial \Phi}{\partial z} - \frac{\partial \psi}{\partial x} \right) \\ &= \nabla^2 \psi. \end{aligned}$$

Now it can be seen that the potential functions Φ and ψ have been chosen such that Φ is associated with dilatation of the medium and ψ associated with rotation of the medium.

Substituting (5-15) into (5-6a) and (5-6b) we get:

$$\rho \frac{\partial}{\partial x} \left(\frac{\partial^2 \Phi}{\partial t^2} \right) + \rho \frac{\partial}{\partial z} \left(\frac{\partial^2 \psi}{\partial t^2} \right) = (\lambda + 2G) \frac{\partial}{\partial x} (\nabla^2 \Phi) + G \frac{\partial}{\partial z} (\nabla^2 \psi) \quad (5-16a)$$

$$\rho \frac{\partial}{\partial z} \left(\frac{\partial^2 \Phi}{\partial t^2} \right) - \rho \frac{\partial}{\partial x} \left(\frac{\partial^2 \psi}{\partial t^2} \right) = (\lambda + 2G) \frac{\partial}{\partial z} (\nabla^2 \Phi) - G \frac{\partial}{\partial x} (\nabla^2 \psi) \quad (5-16b)$$

Eqs. (5-16) are satisfied if

$$\frac{\partial^2 \Phi}{\partial t^2} = \left(\frac{\lambda + 2G}{\rho} \right) \nabla^2 \Phi = v_p^2 \nabla^2 \Phi \quad (5-17a)$$

$$\frac{\partial^2 \psi}{\partial t^2} = \left(\frac{G}{\rho} \right) \nabla^2 \psi = v_s^2 \nabla^2 \psi \quad (5-17b)$$

(5-17) are wave motion eqs. Assuming a solution for a sinusoidal wave traveling in the positive x -direction, expressions for Φ and ψ can be expressed as:

$$\Phi = F(z) \exp[i(\omega t - Nx)] \quad (5-18a)$$

$$\psi = G(z) \exp[i(\omega t - Nx)] \quad (5-18b)$$

The functions $F(z)$ and $G(z)$ describe the variation in amplitude of the wave as a function of depth and N is the wave number defined by

$$N = \frac{2\pi}{L}$$

where L is the wave length. Substituting (5-18) into (5-17) and rearranging we get

$$F''(z) - \left(N^2 - \frac{\omega^2}{v_p^2} \right) F(z) = 0 \quad (5-19a)$$

$$G''(z) - \left(N^2 - \frac{\omega^2}{v_s^2} \right) G(z) = 0 \quad (5-19b)$$

where $F''(z)$ and $G''(z)$ are derivatives with respect to z . If

$$q^2 = \left(N^2 - \frac{\omega^2}{v_p^2} \right) \quad (5-20a)$$

$$s^2 = \left(N^2 - \frac{\omega^2}{v_s^2} \right) \quad (5-20b)$$

Eqs. (5-19) can be rewritten as

$$F''(z) - q^2 F(z) = 0 \quad (5-21a)$$

$$G''(z) - s^2 G(z) = 0 \quad (5-21b)$$

The solutions of eqs. (5-21) are

$$F(z) = A_1 \exp(-qz) + B_1 \exp(qz) \quad (5 - 22a)$$

$$G(z) = A_2 \exp(-sz) + B_2 \exp(sz) \quad (5 - 22b)$$

A solution that allows the amplitude of the wave to become infinite with depth cannot be tolerated; therefore

$$B_1 = B_2 = 0$$

Then eqs. (5-18) becomes

$$\Phi = A_1 \exp[-qz + i(\omega t - Nx)] \quad (5 - 23a)$$

$$\psi = A_2 \exp[-sz + i(\omega t - Nx)] \quad (5 - 23b)$$

Boundary conditions: No stress at the surface of the half-space

$$z = 0 \rightarrow \sigma_z = 0 \text{ and } \tau_{zx} = 0$$

therefore at surface

$$\sigma_z = \lambda \bar{\epsilon} + 2G\epsilon_z = \lambda \bar{\epsilon} + 2G \frac{\partial w}{\partial z} = 0 \quad (5 - 24a)$$

$$\tau_{zx} = G\gamma_{zx} = G \left(\frac{\partial w}{\partial x} + \frac{\partial u}{\partial z} \right) = 0 \quad (5 - 24b)$$

Using the definitions of u and w and the solutions for Φ and ψ from eqs. (5-23), (5-24) can be written

$$\sigma_z|_{z=0} = A_1[(\lambda + 2G)q^2 - \lambda N^2] - 2iA_2GN_s = 0 \quad (5 - 25a)$$

$$\tau_{zx}|_{z=0} = 2iAiNq + A_2(s^2 + N^2) = 0 \quad (5 - 25b)$$

Rearranging eqs. (5-25)

$$\frac{A_1}{A_2} \frac{(\lambda + 2G)q^2 - \lambda N^2}{2iGN_s} - 1 = 0 \quad (5-26a)$$

$$\frac{A_1}{A_2} \frac{2qiN}{(s^2 + N^2)} + 1 = 0 \quad (5-26b)$$

adding (5-26b) to (5-26a) we get

$$\frac{(\lambda + 2G)q^2 - \lambda N^2}{2iGN_s} = -\frac{2qiN}{s^2 + N^2} \quad (5-27)$$

Cross-multiplying eqs. (5-27) we get

$$4qG_sN^2 = (s^2 + N^2)[(\lambda + 2G)q^2 - \lambda N^2] \quad (5-28)$$

Squaring both sides of eqs. (5-28) and substituting (5-20) into (5-28) we get

$$16G^2N^2 \left(N^2 - \frac{\omega^2}{v_p^2} \right) \left(N^2 - \frac{\omega^2}{v_s^2} \right) =$$

$$[(\lambda + 2G) \left(N^2 - \frac{\omega^2}{v_p^2} \right) - \lambda N^2]^2 [N^2 + \left(N^2 - \frac{\omega^2}{v_s^2} \right)]^2 \quad (5-29)$$

dividing through by G^2N^8 , we get

$$16 \left(1 - \frac{\omega^2}{v_p^2 N^2} \right) \left(1 - \frac{\omega^2}{v_s^2 N^2} \right) = \left[2 - \left(\frac{\lambda + 2G}{G} \right) \left(\frac{\omega^2}{v_p^2 N^2} \right) \right]^2 \left(2 - \frac{\omega^2}{v_s^2 N^2} \right)^2 \quad (5-30)$$

Recalling we define

$$N = \frac{2\pi}{L} \text{ then } L = \frac{2\pi}{N}.$$

Let L_R and V_R be the wave length and velocity, respectively, of the surface wave, then also

$$L_R = \frac{V_R}{f} = \frac{2\pi V_R}{\omega} = \frac{2\pi}{N}$$

therefore,

$$N = \frac{\omega}{V_R} \quad N^2 = \frac{\omega^2}{V_R^2}$$

Let K and α be defined such that

$$\frac{V_R^2}{V_s^2} = K^2 \text{ and } \frac{V_R^2}{V_p^2} = \alpha^2 K^2$$

Then

$$\frac{\omega^2}{V_p^2 N^2} = \frac{V_R^2}{V_p^2} = \alpha^2 K^2 \quad (5-31a)$$

$$\frac{\omega^2}{V_s^2 N^2} = \frac{V_R^2}{V_s^2} = K^2 \quad (5-31b)$$

$$\alpha^2 = \frac{V_s^2}{V_p^2} = \frac{\frac{G}{\rho}}{\frac{\lambda+2G}{\rho}} = \frac{G}{\lambda+2G} = \frac{1-2\nu}{2-2\nu} \quad (5-31c)$$

Substituting eqs. (5-31) into (5-30)

$$16(1 - \alpha^2 K^2)(1 - K^2) = \left(2 - \frac{1}{\alpha^2} \alpha^2 K^2\right)^2 (2 - K^2)^2 \quad (5-32)$$

After expansion and rearrangement

$$K^6 - 8K^4 + (24 - 16\alpha^2)K^2 + 16(\alpha^2 - 1) = 0 \quad (5-33)$$

Eq. (5-32) can be considered a cubic equation in K^2 and real valued solutions can be found for given values of ν . The quantity K represents a ratio between the velocity of the surface wave and the velocity of the shear wave.

$$\text{For } \nu = 0.5 \quad V_R = 0.9553V_s.$$

$$\text{For } \nu = 0.25 \quad V_R = 0.9194V_s.$$

3. The Noise of the Surface Wave

The mesh of the soil-pile interaction system is shown in Figure 5.2. The basic problem is the way in which the elastic half space

should be considered. The real system is infinite but the ability for calculation by the computer is limited. An assumption from soil mechanics and foundation design is used here. The assumption is that the effect of the soil to the pile is limited in the range of $2D$ (D is pile's diameter.)

The impulse and boundary condition are the same as for a single pile. The remesh of soil material properties is based on real materials and the soil surrounding the pile is clay. The Young's modulus is about 1250 ksf ($59850kN/m^2$) and the density is about 90 pcf ($14.14kFN/m^3$). The real soil is layered from top to bottom of pile and the different soil layers have different properties. Since the effect of the surface wave is desired a homogeneous model is used but it isn't a one dimension model, so Poisson's ratio is considered. The Poisson's ratio of the pile is 0.15 and the soil Poisson's ratio is 0.25. All the data for the soil are the average taken from tables 5.1, 5.2 and 5.3.

The response at the top of the pile is shown in Fig. 5.3. It is more close to the test result of the response on a single sound pile (see Figure 4.28).

The effectiveness of the surface wave is reduced with depth. The response at the depth of 5' is shown in Fig. 5.4. The noise of the surface wave almost disappears at this depth. The test data from Houston, Texas gives the same conclusion. The response received by the accelerometers, which were embedded below the 5' depth, is only slightly effected by the surface wave noise.

The existing noise of the surface wave presented the response at the top of the soil-pile interaction system with greater complexity than the response on the single pile since the attenuation has not been considered yet. Considering the attenuation the reflection received at the top of the pile may be very weak since the wave energy is dissipated by the frictional resistance and radiation.

The existing of the surface wave in an elastic half space is the one important reason to make a difference between the field test results and one-dimensional wave propagation theory.

4. The Effect of Soil

a. Unhomogeneous

The real soil medium is not homogeneous which is assumed in the theory but rather it is usually layered. It has been shown that elastic waves will be at least partially reflected at an interface between two media, and if horizontal layering occurs in a half-space (as shown in Fig. 5.5) some energy originating at the surface and traveling into the half-space will return to the surface. If more than one interface exists, waves may be reflected back to the surface from each layer interface.

These reflections and refractions can make the records very complex, but fortunately the P-wave propagation velocity in soil is much less than it is in concrete. Thus the reflection from the bottom of the pile arrives at the top of the pile much earlier than those which come from soil as shown in Table 5.4. The response at the top of the pile soil medium that is meshed using different layers is shown in Fig. 5.6. Comparing Fig. 5.6 with Fig. 5.3 we can see that they are similar.

b. The Friction Between Pile and Soil

When waves propagate in a rod, the compression wave is reflected at the bottom of the rod as a tension wave with the same magnitude according to theory. The real situation of wave propagation in a pile-soil system is different since there is friction between the pile surface and the soil and this friction reduces the wave energy. The reflection that is received at the top of the pile is thus, much smaller than that computed by the theory.

The Cracker Program doesn't consider the friction between the pile surface and soil but this has proved to be an important factor which effects the accuracy of the test.

A principle which is often used in structural mechanics is used here. Separate the pile from the pile-soil system. Then the interaction between pile and soil acts on the pile side surface as a shear stress (see Figure 5.7).

The shear stress along the pile surface is to model the friction.

The mesh is shown in Fig. 5.8.

The response on the top of pile with uniform shear stress 0.005 lb/in^2 (0.0344 kN/m^2) along the side surface is shown in Fig. 5.9.

The response on the top of the pile with uniform shear stress 0.01 lb/in^2 (0.06895 kN/m^2) along the side surface is shown in Fig. 5.10.

The response on the top of pile with uniform shear stress 0.05 lb/in^2 (0.344 kN/m^2) along the side surface is shown in Fig. 5.11.

The response on the top of the pile with different shear stress along the side surface is shown in Fig. 5.12.

Comparing these Figures we can see: a) that with increasing friction, the magnitude of the reflection is reduced, b) different soil layer has different coefficient of friction, which effects the response on the top of the pile.

5. The effect of defect cross area

The mesh for four different defect cross area pile models are shown in the following figures;

Pile with $1/4$ defect cross area – see Fig. 5.13

Pile with $1/2$ defect cross area – see Fig. 5.14

Pile with $3/4$ defect cross area – see Fig. 5.15

Pile with whole defect cross area – see Fig. 5.16

The pile's diameter is 18 in. (0.4752 m), the piles length is 45 ft. (13.716 m), which is the same as the test pile in Texas.

The response on the top of the pile with $1/4$ defect cross area is shown in Fig. 5.17. The peak of the reflection came from defeat (second peak) is equal to $1/2$ of peak caused by impulse (first peak).

The response on the top of the pile with $1/2$ defect cross area is shown in Fig. 5.18. The peak of the reflection came from defect (second peak) is equal to the peak caused by impulse (first peak).

The response on the top of the pile with $3/4$ defect cross area is shown in Fig. 5.19. The peak of the reflection came from defect (second peak) is equal to $3/2$ of the peak caused by impulse (first peak).

The response on the top of the pile with whole defect cross area is shown in Fig. 5.20. The peak of the reflection came from defect (second peak) is equal to two of the peaks caused by impulse (first peak). According to the theory the response returning from a defect to the top of the pile is proportional to the defect cross area.

According to the test data (in Texas), the received reflection on the top of the pile with 1/2 defect cross area is equal to that coming from a pile with an interruption in the entire cross section. The received reflection at the top of the pile with a 1/4 defect cross area is unclear. This indicated that the defect cross sectional area is another factor which effects the accurate of the test.

6. Continuous Medium

Estimating P-wave velocity is important when testing the pile integrity. After knowing P-wave velocity and the receiving time then the length of the pile can be known according to the one dimension wave propagation theory $V_p^2 = \frac{E}{\rho}$. According to concrete theory the modulus of elasticity E_c can be computed:

$$\begin{aligned}
 E_c &= 33W_c^{1.5}\sqrt{f'_c} && \text{(ACI Code)} \\
 & && (W_c = 90 \text{ to } 155 \text{ pcf}) \\
 E_c &= 57000\sqrt{f'_c} && (W_c = 145 \text{ pcf}) \\
 E_c &= (40,000\sqrt{f'_c} + 1,000,000) && (W_c/145)^{1.5} \\
 & && \text{(Based on recent research} \\
 & && \text{at Cornell University)}
 \end{aligned}$$

These values are based upon the assumptions that the concrete compressive strength is the range of 4000 psi (27.6 MPa/m^2) and the unit weight W_c is 145 pcf (22.78 kN/m^3). (These are typical data for concrete.)

Then $V_p = 10600 \text{ ft/s}$ (3231 m/s).

According to some test measurements shown on Table 5.5 and Table 5.6. The measured P-wave velocity is greater then the calculated P-wave velocity. This difference from that of the theory is due to the one dimension wave propagation and the real pile is in a half-space

medium.

a. Poisson's Ratio

When waves propagate in a infinite continuous or half-space medium and then the P-wave velocity is computed the Poisson's Ratio must be considered by formula (5-10).

$$V_p = \sqrt{\frac{E}{p} \frac{(1 - \nu)}{(1 + \nu)(1 - 2\nu)}}$$

Using $\nu = 0.15$, $V_p = 11920$ ft/s (3411 m/s) the results are closer to the measurements.

b. *P*-wave velocity is increased with the depth

When waves propagate in soil the velocity of wave is not a constant. Some data test from China done by the author is shown in Fig. 5.21 and Fig. 5.22. These curves shown the shear wave velocity is increased with increases in depth. Since there is relationship between shear wave velocity and compression wave velocity we assume that the compression wave velocity is increased with the depth. For soil it's easy explain since the soil properties E , ν are changed with the depth with E generally increasing with depth. But the concrete properties should be constant, then the question is why is the p-wave velocity increased with the depth, as shown in the test data at Houston, Texas, (see table 5.7). Since the piles are embedded in soil there is interaction between pile and soil. When the elastic modulus of the soil is increased then the combined P-wave velocity is increased. This also explains increased measured velocity as compared to the computed velocity. Fig. 5.21 and Fig. 5.22 shows that the increase is not linear. The details and the reason need further studies.

CHAPTER 6

Conclusions and Recommendations

1. The principle for low strain pile integrity test is technically correct. It is based on the one dimension wave propagation and has been proven by both the Finite Element Method analysis and by field testing. It is a simple economical and rapid test procedure which increases its practical usage.
2. There are however, factors which effect the accuracy of the test results. The most important factors are: the noises of surface waves and the friction between the pile's side surface and the soil.
3. The surfaces waves extend to depths of no more than 5 feet (1.52 m) below the surface of the ground. Two methods could be used to avoid this disturbance. One is embedment of the receiver below a depth of 5 ft. (1.52 m) and the second method would be by usage of a filter. This method requires a very careful selection of the frequency of the filter.
4. The friction effects the magnitude of reflection received on the top of the pile. Amplification equipment can be used to increase this signal. Piles are surrounded by soil with high friction coefficients dampen the wave and greatly weaken the reflections. In these soils high strain pile integrity test is recommended.
5. For estimating the P-wave propagation velocity prior to testing it's recommended that the formula which is used for wave propagate in continuous medium be used. Since it agrees more closely to the field measurements.
6. The wave velocity propagated in a continuous medium is not a constant. It increases with the depth and the increase is non-linear. The reason and the details need to be further studied.

7. The magnitude of reflection at the top of the pile is also proportional to the defect cross sectional area. When the defect is small it is very difficult to interpret the reflected signals and thus to discover the defect.

List of Tables

Number	Title
5.1	Value Ranges for Modulus E_s
5.2	Value Ranges for Poisson's Ratio μ
5.3	Typical Values of Void Ratios and Dry Unit Weights for Granular Soils
5.4	Velocities of Compression Wave V_c and Shear Wave V_s
5.5	Compression Wave Velocity (Malhotra, 1976)
5.6	Compression Wave Velocity (Harrell, 1984)
5.7	Compression Wave Velocity vs Depth

List of Figures

Number	Title
2.1	Problem Description
2.2	Force Equilibrium on a Small Element
2.3	Normal Strain
2.4	Shear Strain
2.5	Surface-Traction-Stress Relations
2.6	Triangular "Natural" coordinate system
2.7	Six Noded Interface Element
2.8	Traction-Displacement Relation
2.9	Geometry Relation
2.10	Central Difference Approach
3.1	Longitudinal Vibration of a Rod
3.2	Impact Pulse and Reflections
3.3	Proceeding of Pile Integrity Test
3.4	Pile Location
3.5	Boring of the Piles
3.6	The Excavated Bore Hole after Completion
3.7	Concrete Emplacement
3.8	Concrete Mixer Used to Form Pile
3.9	Test Piles
3.10	Preparing the Surface of the Pile
3.11	Power Supply for Test
3.12	Impacting the Pile
3.13	Electronic Pile Test Equipment
4.1	Mesh of a Single Pile
4.2	Triangular Finite Elements
4.3	Boundary Condition of Single Pile
4.4	Impulse
4.5	Response at the Top of a Sound Pile
4.6	Response in the Up Middle of a Sound Pile
4.7	Response in the Down Middle of a Sound Pile

List of Figures (continued)

- 4.8 Response at the Bottom of a Sound Pile
- 4.9 Crack Location
- 4.10 Mesh of Crack
- 4.11 Response on the Top of Pile with Crack in the Middle
- 4.12 Response in the Pile above the Crack
- 4.13 Response at the Crack
- 4.14 Response in the Pile Below the Crack
- 4.15 Response at the Bottom of Pile with Crack
- 4.16 Mesh of Void
- 4.17 Response on the Top of the Pile with Void
- 4.18 Response at the Upside of the Void
- 4.19 Response at the Downside of the Void
- 4.20 Response at the Bottom of the Pile with Void
- 4.21 Surrounding Soil Conditions in Newark, NJ
- 4.22 Surrounding Soil Conditions in Newark, NJ
- 4.23 Test Record for Pile 41
- 4.24 Test Record for Pile 47
- 4.25 Test Record for Pile 50
- 4.26 Test Record for Pile 125
- 4.27 Test Record for Pile 128
- 4.28 Test Record for Pile 130
- 4.29 Test Record for Pile 53
- 4.30 Test Location of Test at Houston, Texas
- 4.31 Soil Condition in Houston, Texas
- 4.32 Test Pile Dimensions
- 4.33 Test Record for Pile A
- 4.34 Test Record for Pile B
- 4.35 Test Record for Pile C (drop hammer)
- 4.36 Test Record for Pile C (hand held hammer)
- 4.37 Test Record for Pile D
- 4.38 Test Record for Pile A1.EAST

List of Figures (continued)

- 4.39 Test Record for Pile C1.EAST
- 4.40 Test Record for Pile E1.EAST
- 4.41 Test Record for Pile A4.3A
- 5.1 Coordinate Convention for Elastic Half-Space
- 5.2 Soil - Pile Interaction System
- 5.3 Response on the Top of Pile Surrounded by Soil
- 5.4 Response at the depth of 5 ft (1.52m) of Pile Surrounded by Soil
- 5.5 Multiple Wave Reflection and Refraction in a Layered Half-Space
- 5.6 Response on the Top of Pile Surrounded by Layered Soil
- 5.7 Shear Stress Acts Along the Side Surface of a Pile
- 5.8 Mesh of Shear Stress
- 5.9 Response at the Top of the Pile with Uniform Shear Stress 0.005 lb/in^2 along the side surface
- 5.10 Response at the Top of the Pile with Uniform Shear Stress 0.01 lb/in^2 Along the Side Surface
- 5.11 Response at the Top of the Pile with Uniform Shear Stress 0.05 lb/in^2 Along the Side Surface
- 5.12 Response at the Top of the Pile with Ununiform Shear Stress Along the Side Surface.
- 5.13 Pile with $1/4$ Defect in the Cross Sectional Area
- 5.14 Pile with $1/2$ Defect in the Cross Sectional Area
- 5.15 Pile with $3/4$ Defect in the Cross Sectional Area
- 5.16 Pile with Whole Defect in the Cross Sectional Area

List of Figures (continued)

- 5.17 Response on the Top of the Pile with $1/4$
Defect in the Cross Sectional Area
- 5.18 Response on the Top of the Pile with $1/2$
Defect in the Cross Sectional Area.
- 5.19 Response on the Top of the Pile with $3/4$
Defect in the Cross Sectional Area
- 5.20 Response on the Top of the Pile with $4/4$
Defect in the Cross Sectional Area
- 5.21 Velocity of Shear Wave vs. Depth
(Up-Down Hole Method)
- 5.22 Velocity of Shear Wave vs. Depth
(Cross-Hole Method)

List of References

1. A. Scot Harrell and Kenneth H. Stokoe II, "Integrity Evaluation of Drilled Piers by Stress Waves", Research Report 257-1F, Center for Transportation Research, The University of Texas at Austin, January, 1984.
2. Baker, C.N. and F. Khan, "Caisson Construction Problems and Correction in Chicago", Journal of the Soil Mechanics and Foundation Division, ASCE, February, 1971, Vol. 97, pp. 417-440.
3. Bent, Hansen and Hons, Denver, "Wave Equation Analysis of a Pile - An Analytic Model, Aplice of Stress-Wave Theory on Piles", First International Conference, Stockholm, 1981, pp. 3-22.
4. Davis, R.M., "A critical Study of the Hopkinson Pressure Bar", Philographical Transactions of the Royal Scoiety, Jan. 1948, Vol. 240, pp. 375-457.
5. D. Levacher and J.G. Sieffert, "Effects of Dynamical Devices on Tension Piles Behavior", Application of Stress-Wave Theory on Piles, 1984, pp. 194.
6. D. R. Levacher, J.G. Sieffert, "A Finite Difference Method Applied to the Behavior of Frictional Driven Piles", Application of Stress-Wave Theory on Piles Second International Conference. Swedish Pile Commission, Stockholm, 1985, pp. 334-341.
7. Feld, J., "Construction Failure", John Wiley and Sons Leds., 1968, p. 78.
8. F.E. Richard and R.D. Woods, "Vibrations of Soils and Foundations", Prentice-Hall International Series in Theoretical and Applied Mechanics, 1970.
9. Frank Ransche, "Soil Response from Dynamic Analysis and Measurement on Piles", Case Western Reserve University, 1970. Thesis for a PhD report.

10. Glanville, W.H., Grime, G., Fox, E.N., Davies, W.W., "An Investigation of the Stress in Reinforced Concrete Piles During Driving", British Building Research Board, Technical Paper No. 20, Long, 1938.
11. Gooble, G.G., Likins, G.E., Ransche, F., "Bearing Capacity of Piles from Dynamic Measurements", Final Report, Department of Civil Engineering, Case Western Reserve University, March, 1975.
12. Hearne, T., Stokoe, K. and Reese, L., "Drilled Shaft Integrity by Wave Propagation Method", Journal of the Geotechnical Engineering Division (107), GT 10, 16582 (1981), pp. 1327-1344.
13. Housel, W.S., "Michigan Study of Pile Driving Hammers", Proceedings of the American Society of Civil Engineers", Vol. 91, SM5, S. 33-64, 1965.
14. H. Van Koten, P. Middendorp Sr., P. Van Brederode, "An Analysis of Dissipative Wave Propagation in a Pile", Application of Stress-Wave Theory on Piles First International Conference, Stockholm, 1981, pp. 23-40.
15. Isaacs, D.V., "Reinforced Concrete Pile Formulas", Transactions of the Institution of Engineers, Australia, XII, 1931, pp. 305-323.
16. Joseph E. Bowles, "Foundation Analysis and Design", McGraw-Hill, 1988.
17. N.F. Febecken, E.C. Lima, L. London, A.L.G.A. Coutinho. "Numerical Simulation of Pile Driving by Finite Elements. Some Practical Applications on the Brazilian Coast", Application of Stress-Wave Theory on Piles Second, pp. 340-359.
18. Rausche, F., Seitz, J., "Integrity Testing of Shafts and Caissons". Symposium on Dynamic Measurements for Capacity and Integrity Evaluation of Piles and Piers, ASCE, Philadelphia. May 1983.

19. Reese, L.C., and S.G. Wright, "Construction of Drilled Shafts and Design for Axial Loading", Drilled Shaft Design and Construction Guidelines Manual, Vol. 1, U.S. Department of Transportation, July, 1977.
20. Shansher Prakash, Soil Dynamics, McGraw Hill Book Company, 1981.
21. Shear, S.K., and A.B. Focke, "The Dispersion of Supersonic Waves in Cylindrical Rods of Polycrystalline Silver, Nickel and Magnesium", Physical Review, March, 1940, Vol. 57, pp. 532-537.
22. Smith, E.A.L., "Pile Driving Analysis by the Wave Equation", Journal of Soil Mechanics and Foundations, ASCE Vol. 86, SM, August 1960, pp. 35-61.
23. Steinbach, J., Vey, E., "Caission Evaluation by Stress Wave Propagation Method", Journal of the Geotechnical Engineering Division ASCE, GT4, 112454, 1975, pp. 311-378.
24. Timoshenko, S. and Goodier, J.M., Theory of Elasticity, McGraw Hill, Second Edition, 1951, pp. 438.
25. Y. K. Chow, I. M. Smith, "A Numerical Model for the Analysis of Pile", pp. 319-323.
26. Yolsky, H., "Stress Wave in Solids", Dover Publications, Inc., 1963.

Typical range of values for the static stress-strain modulus E_s for selected soils

Field values depend on stress history, water content, density, etc.

Soil	E_s	
	ksf	Mpa
Clay		
Very soft	50-250	2-15
Soft	100-500	5-25
Medium	300-1000	15-50
Hard	1000-2000	50-100
Sandy	500-5000	25-250
Glacial till		
Loose	200-3200	10-150
Dense	3000-15 000	150-720
Very dense	10 000-30 000	500-1440
Loess	300-1200	15-60
Sand		
Silty	150-450	5-20
Loose	200-500	10-25
Dense	1000-1700	50-81
Sand and gravel		
Loose	1000-3000	50-150
Dense	2000-4000	100-200
Shale	3000-300 000	150-5000
Silt	40-400	2-20

Table 5.1

Values or value ranges for Poisson's ratio μ

Type of soil	μ
Clay, saturated	0.4-0.5
Clay, unsaturated	0.1-0.3
Sandy clay	0.2-0.3
Silt	0.3-0.35
Sand, gravelly sand	-0.1-1.00
commonly used	0.3-0.4
Rock	0.1-0.4 (depends somewhat on type of rock)
Loess	0.1-0.3
Ice	0.36
Concrete	0.15

Table 5.2

Table 5.3 Typical values of void ratios and dry unit weights for granular soils

Soil type	Void ratio e		Dry unit weight γ_d			
			Minimum		Maximum	
	Maximum	Minimum	lb/ft ³	kN/m ³	lb/ft ³	kN/m ³
Gravel	0.6	0.3	103	16	127	20
Coarse sand	0.75	0.35	95	15	123	19
Fine sand	0.85	0.4	90	14	118	19
Standard Ottawa sand	0.8	0.5	92	14	110	17
Gravelly sand	0.7	0.2	97	15	138	22
Silty sand	1	0.4	83	13	118	19
Silty sand and gravel	0.85	0.15	90	14	144	23

Table 5.4 Velocities of Compression Waves v_c and Shear Waves v_s †

Soil	$\rho, \text{kg} \times \text{s}^2/\text{cm}^4$	$v_c, \text{m/s}$	$v_s, \text{m/s}$
Moist clay	1.8×10^{-6}	1500‡	150
Loess at natural moisture	1.67×10^{-6}	800	260
Dense sand and gravel	1.70×10^{-6}	480	250
Fine-grained sand	1.65×10^{-6}	300	110
Medium-grained sand	1.65×10^{-6}	550	160
Medium-sized gravel	1.8×10^{-6}	750	180

† After Barkan (1962).

‡ This value is close to the velocity of wave propagation in water.

Compression Wave Velocity		General Conditions
ft/sec	m/sec	
Above 15,000	Above 4570	Excellent
12,000 to 15,000	3660 to 4570	Good
10,000 to 12,000	3050 to 3660	Questionable
7,000 to 10,000	2133 to 3050	Poor
Below 7,000	Below 2130	Very Poor

Table 5.5 Compression Wave velocity (Malhotra,1976)

P-Wave Velocity, fps	E, psi**	General Condition
Above 13,500	5.90	Excellent
10,800 to 13,500	3.77 to 5.90	Good
9,000 to 10,800	2.62 to 3.77	Questionable
6,300 to 9,000	1.28 to 2.62	Poor
Below 6,300	1.28	Very Poor

*Assuming wavelength is greater than two times diameter of pier
 **Assuming of concrete equals 150 pcf

Table 5.6 Compression Wave Velocity (Harrell,1984)

<u>Receiver</u> <u>Depth</u> <u>f_t</u>	Compression Wave Velocity	
	ft/sec	
	<u>Direct</u>	<u>Interval</u>
10	13,510	13,700
20	13,610	13,330
30	13,510	14,290
40	<u>13,700</u>	
Avg.		13,580

Table 5.7 Compression Wave Velocity vs. Depth

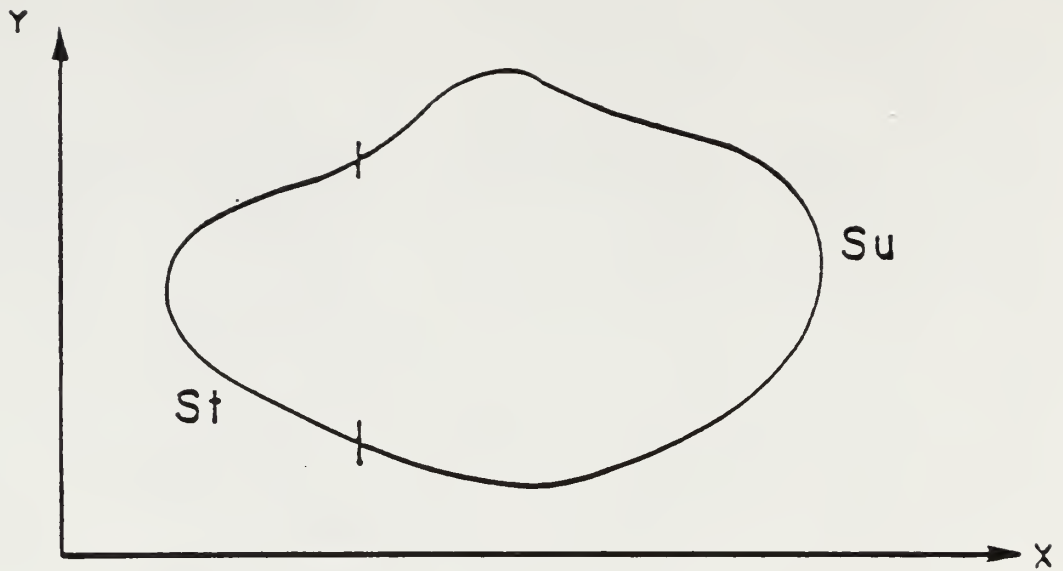


Fig.2.1 Problem Description

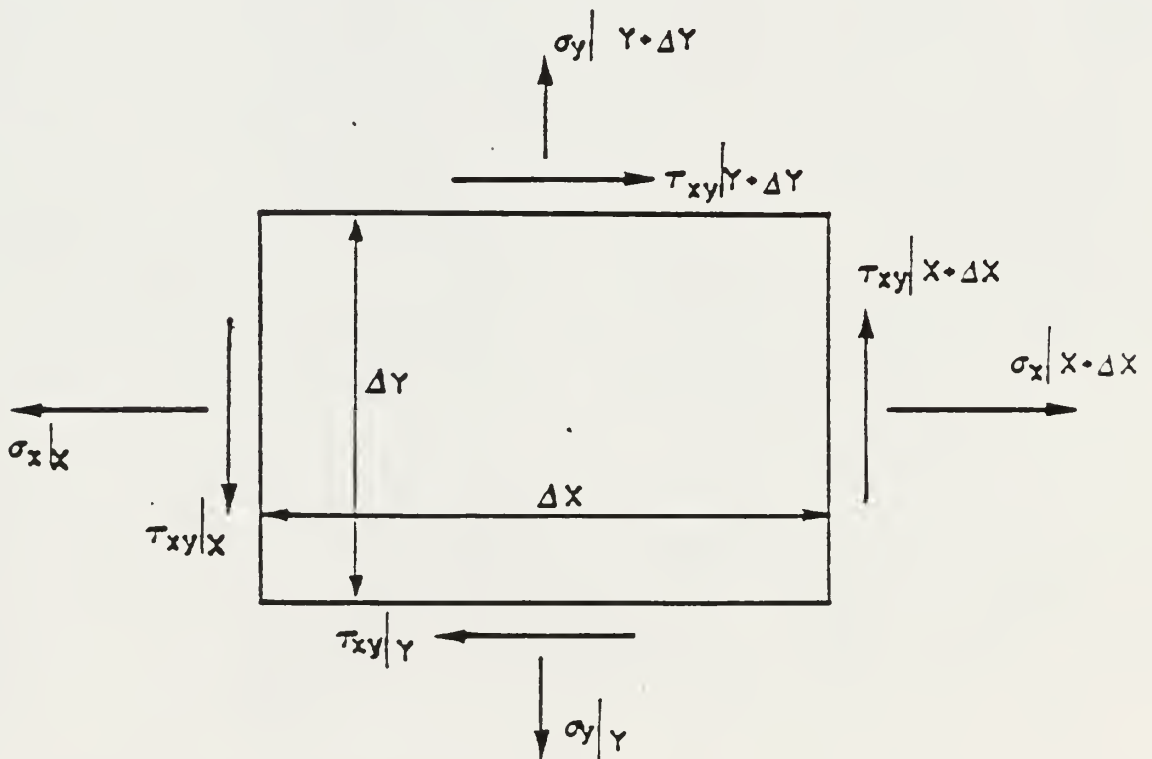


Fig.2.2 Force Equilibrium on a Small Element

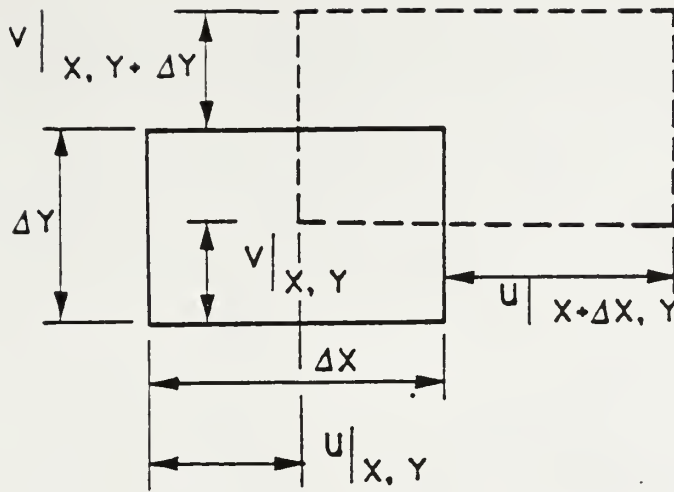


Fig.2.3 Normal Strain

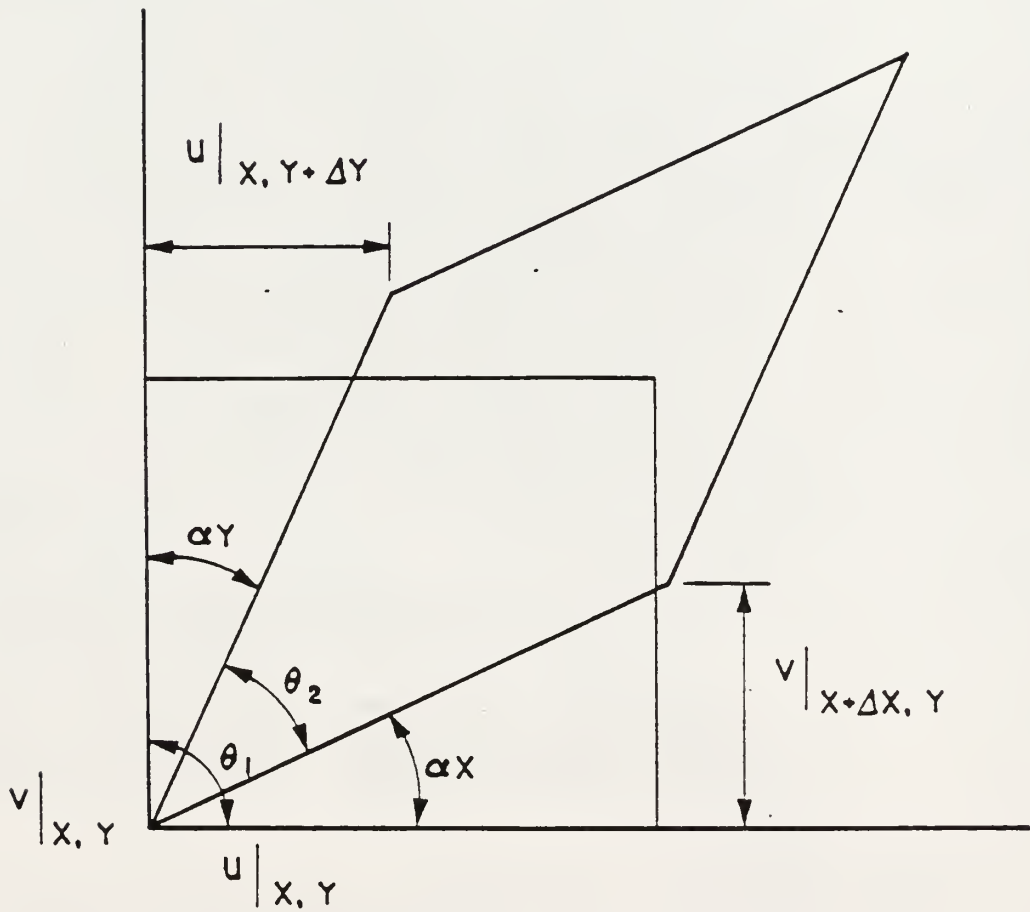


Fig.2.4 Shear Strain

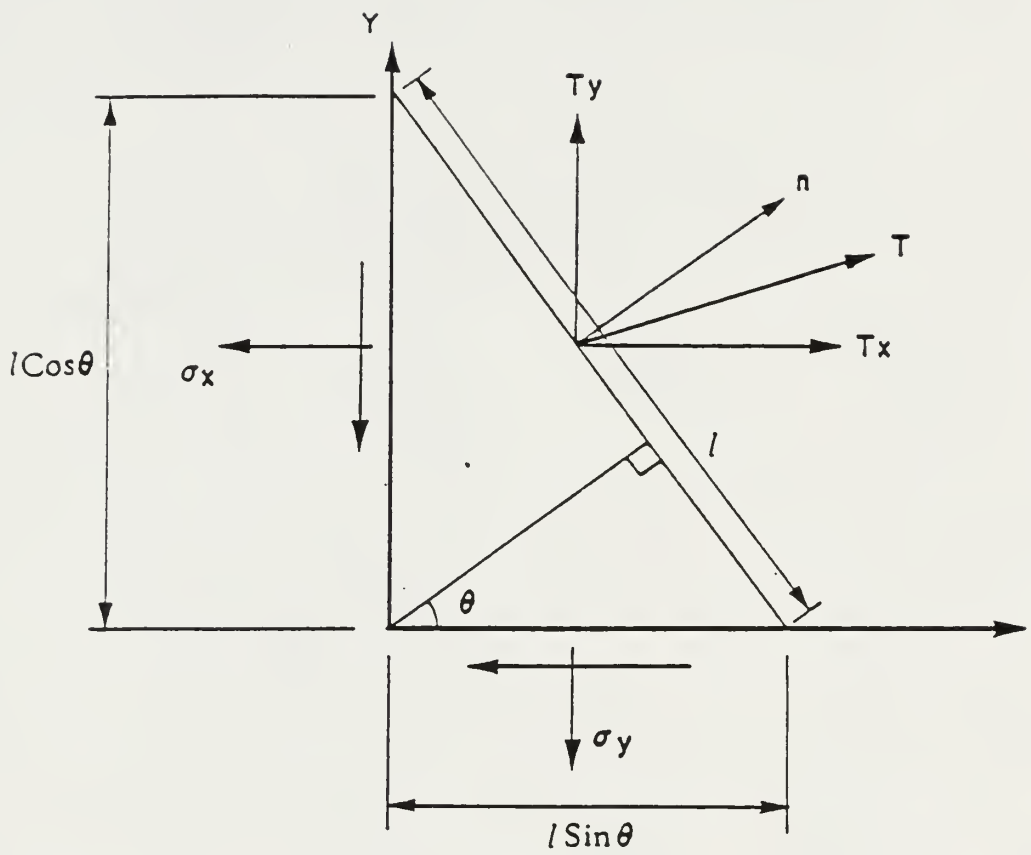


Fig. 2.5 Surface-Traction-Stress Relation

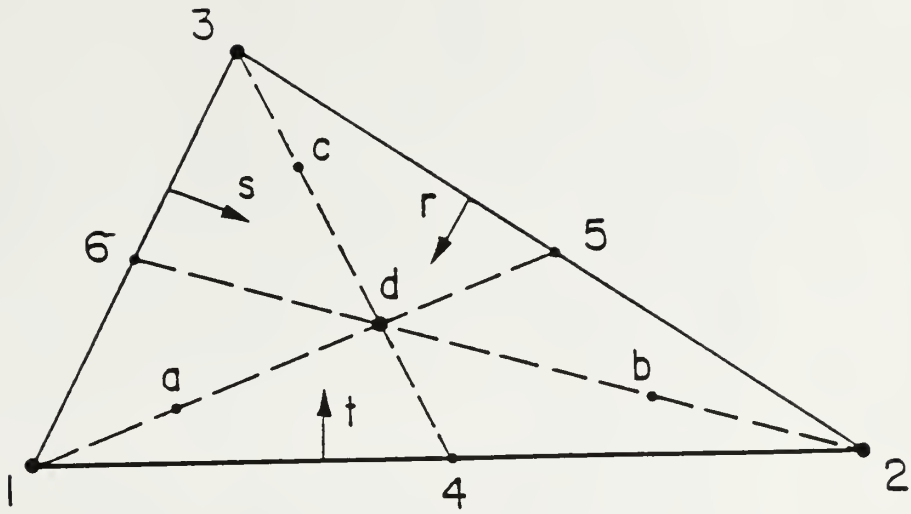


Fig. 2.6 Triangular "Natural" Coordinate System

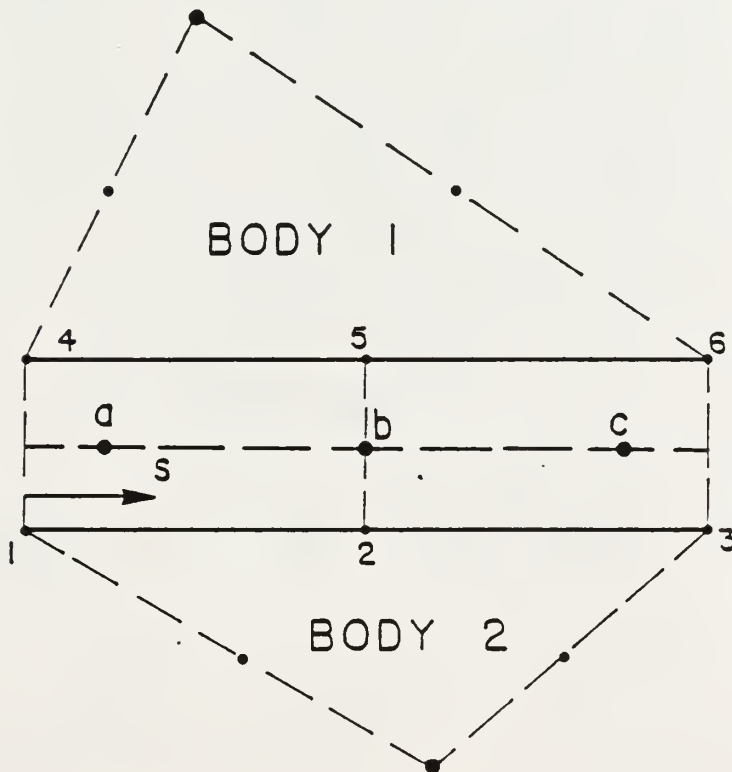


Fig. 2.7 Six Noded Interface Element

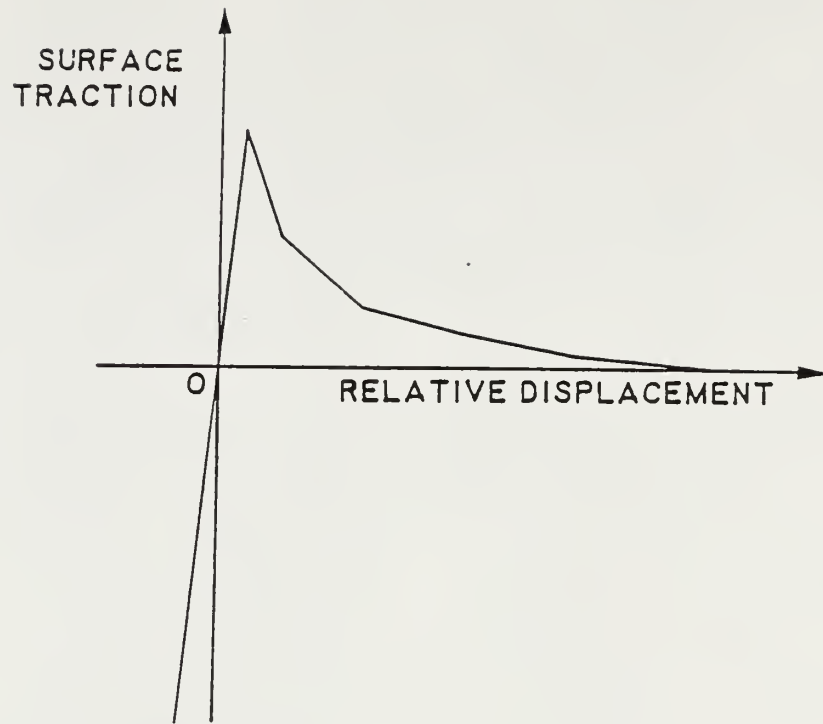


Fig. 2.8 Traction-Displacement Relation

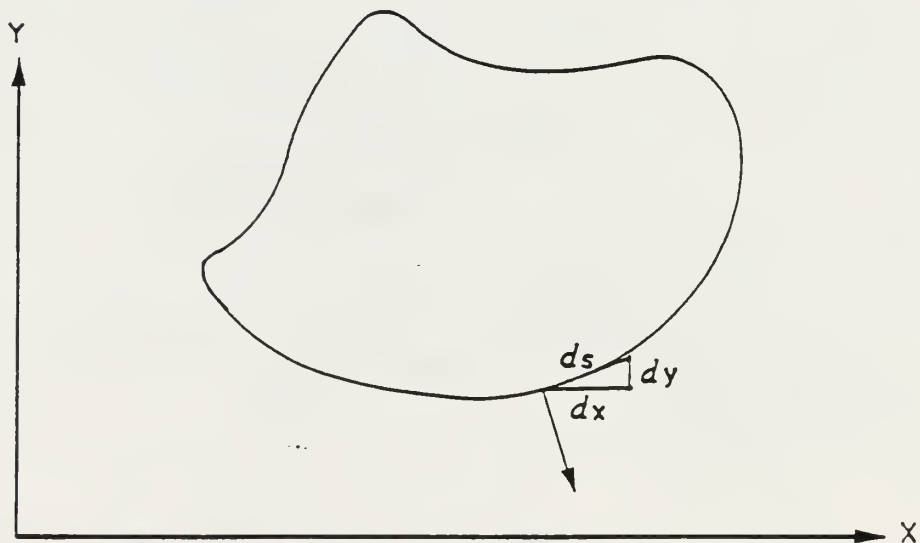


Fig. 2.9 Geometry Relation

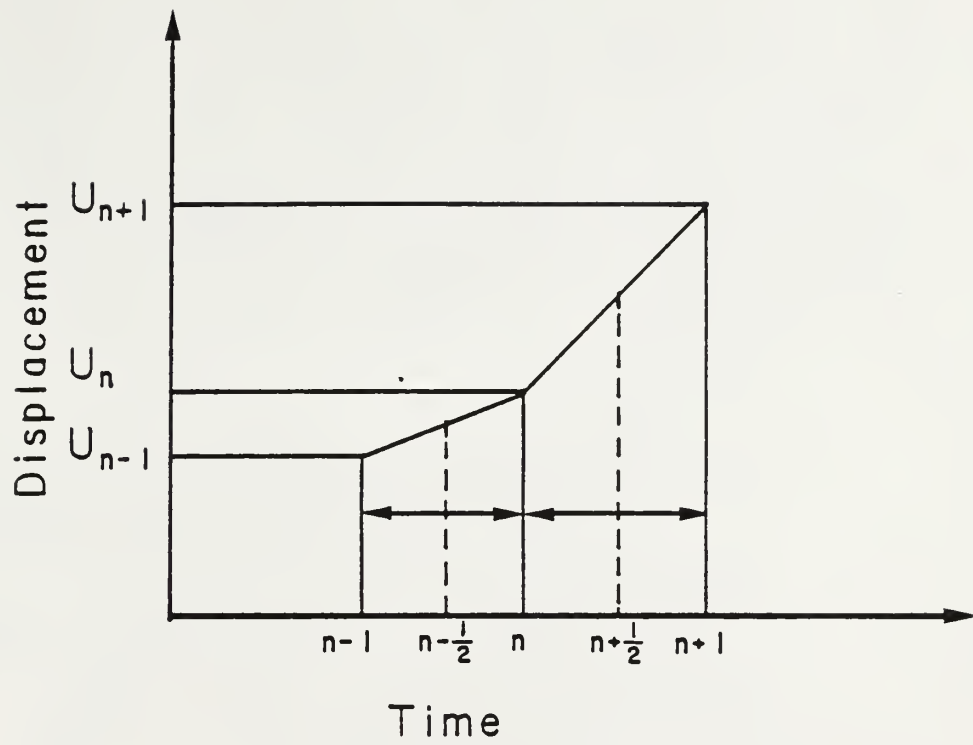


Fig. 2.10 Central Difference Approach

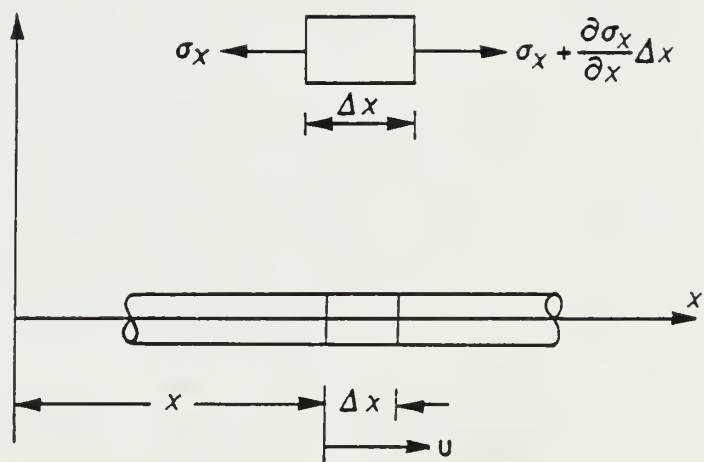


Fig. 3.1... Longitudinal Vibration of a Rod

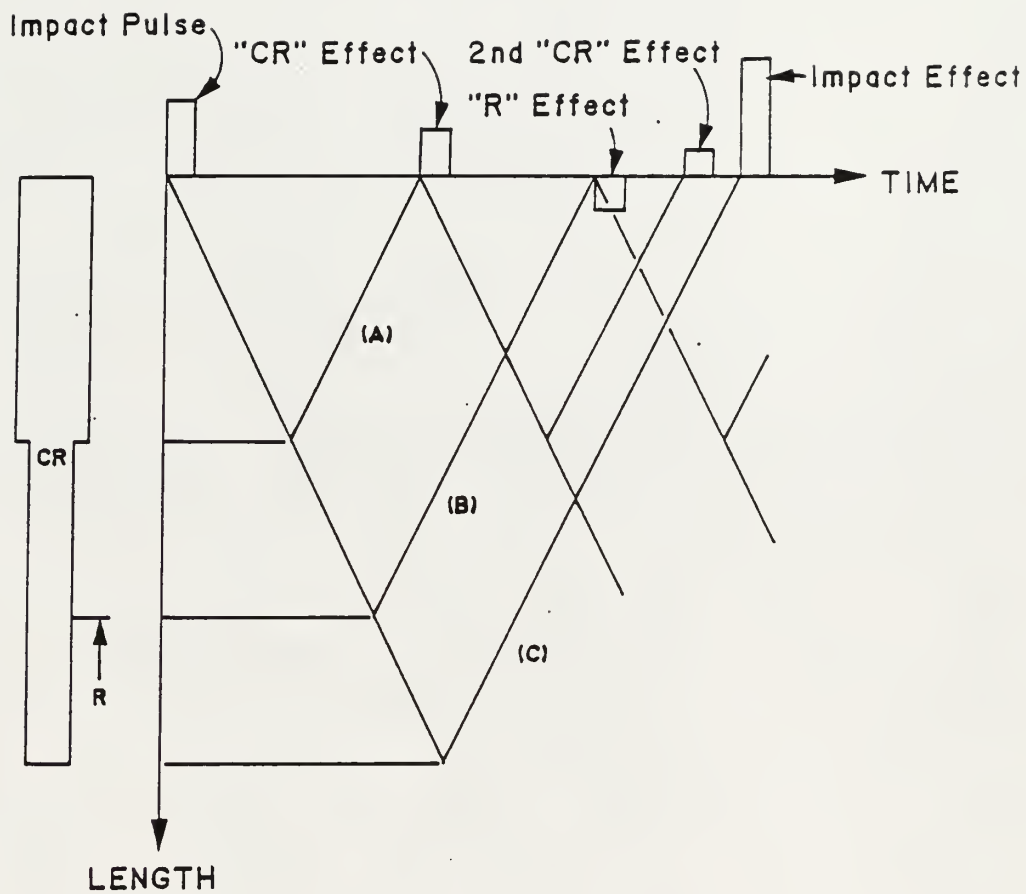


Fig. 3.2 Impact Pulse and Reflections

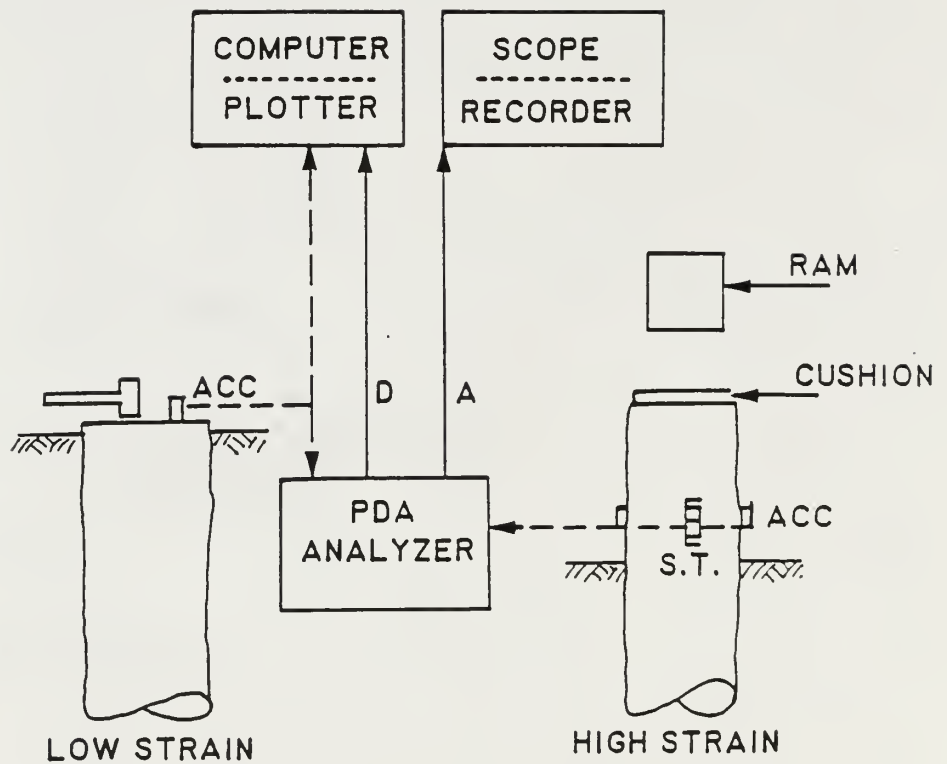


Fig. 3.3 Proceeding of Pile Integrity Test

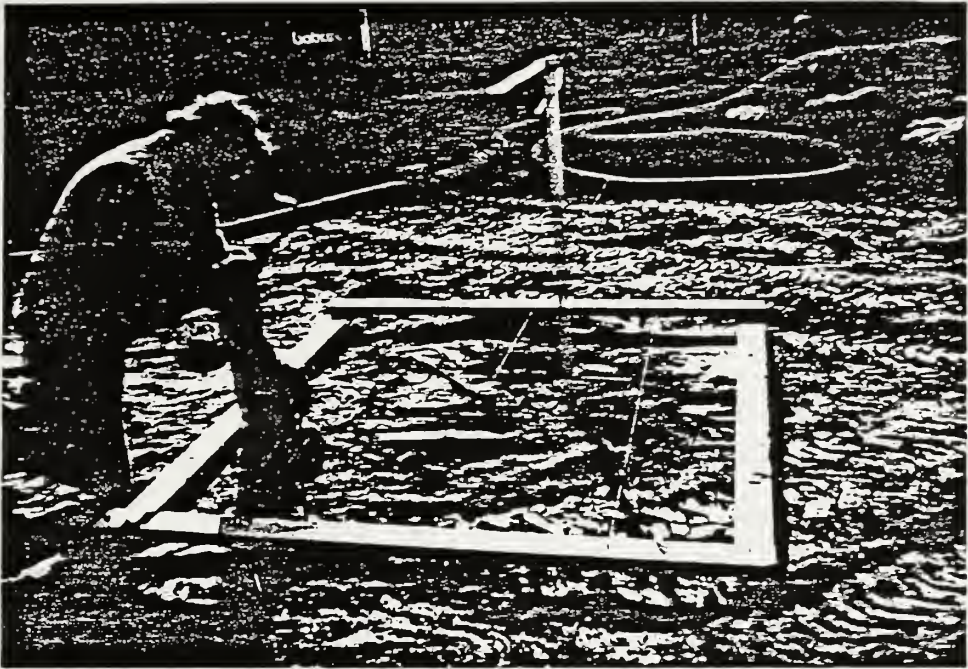


Fig. 3.4 Pile Location

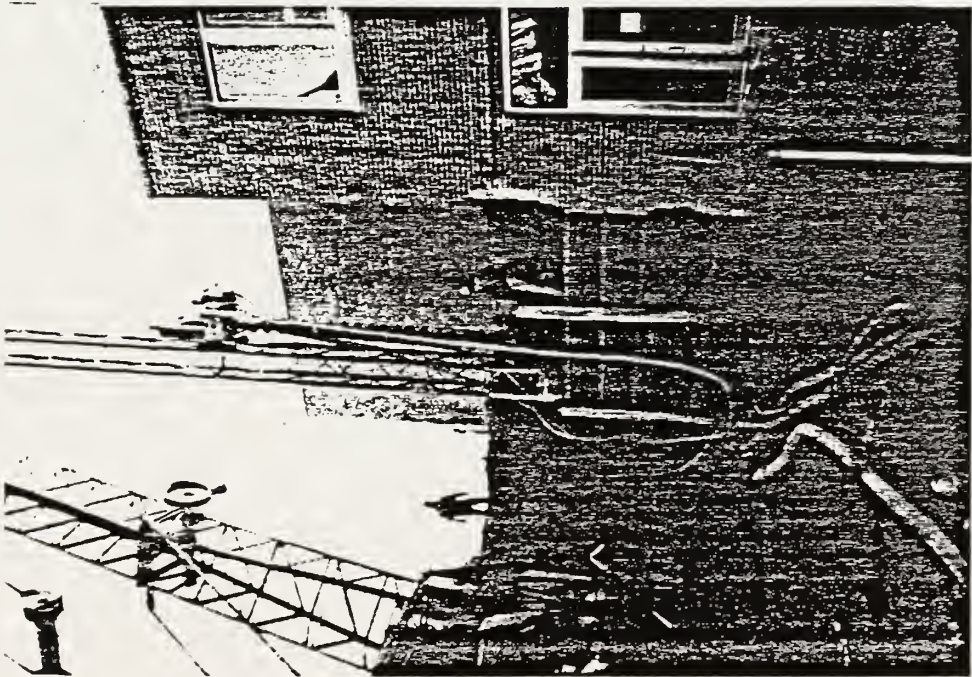


Fig. 3.5 Boring of the Piles

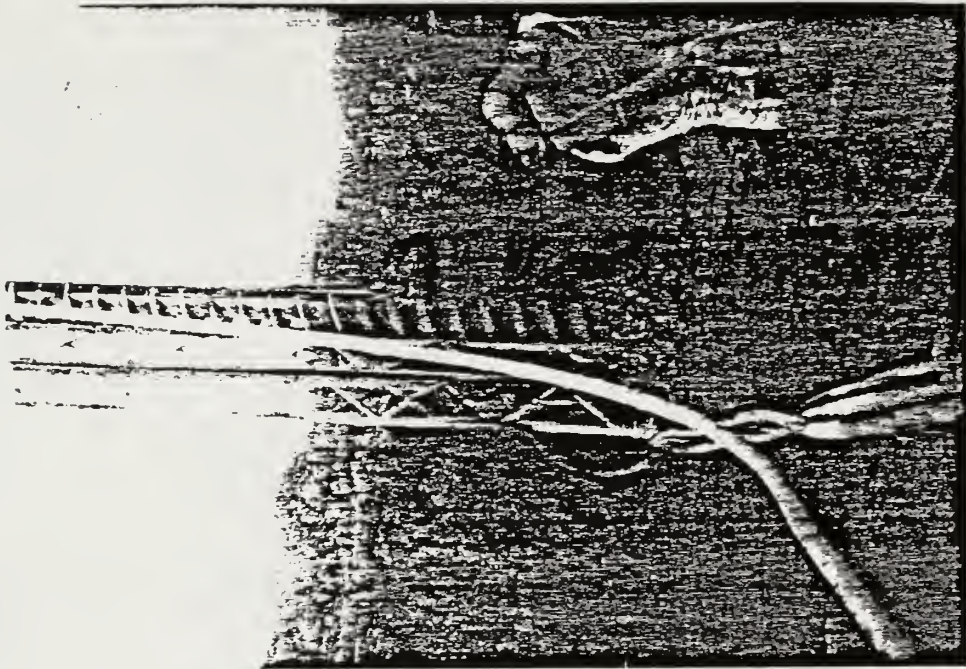


Fig. 3.7 Concrete Emplacement

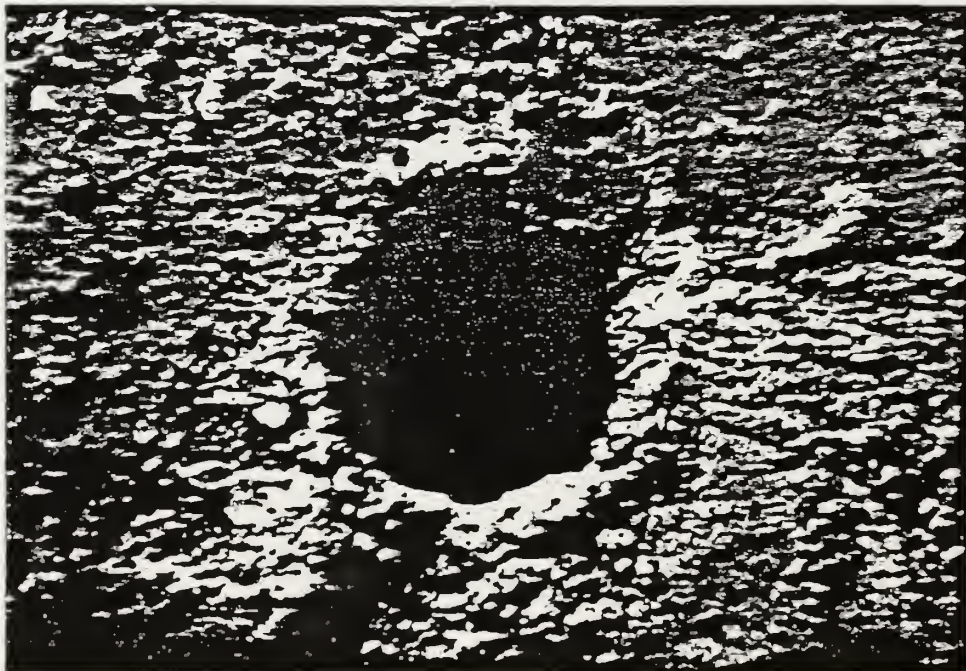


Fig. 3.6 The Excavated Bore Hole after Completion

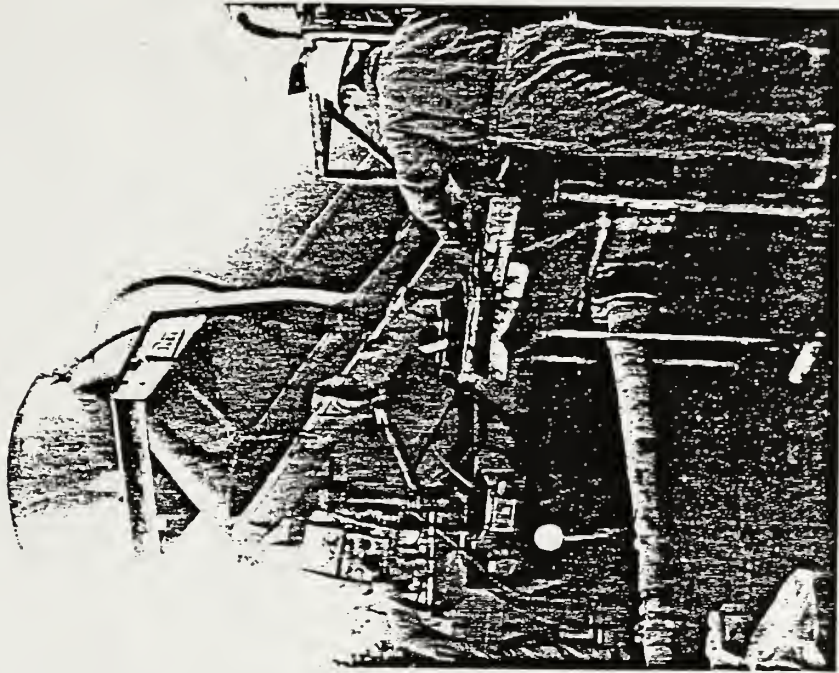


Fig 3.8 Concrete Mixer Used to form Pile

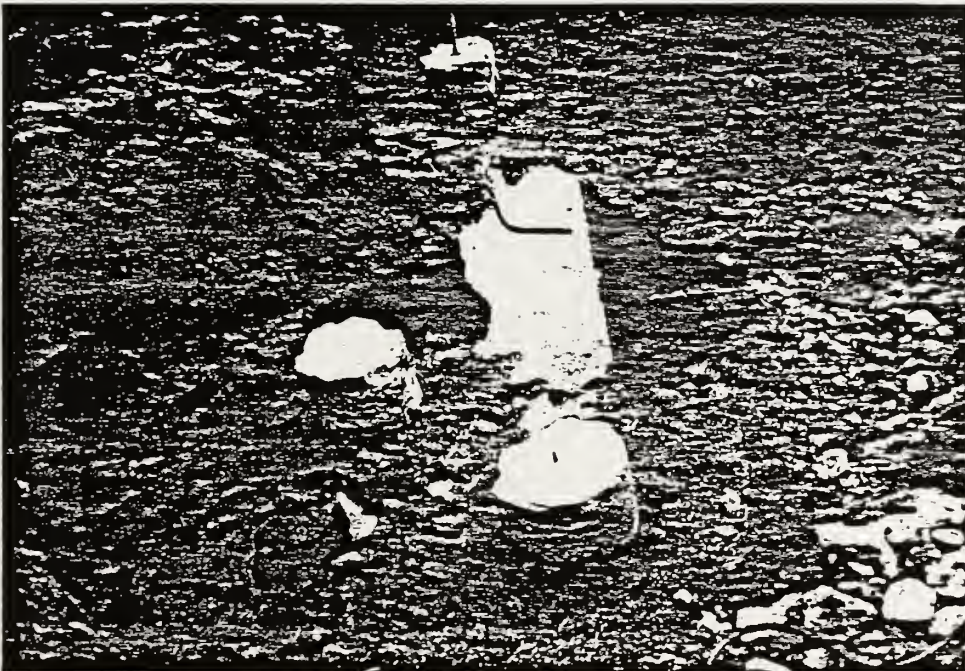


Fig 3.9 Test Piles

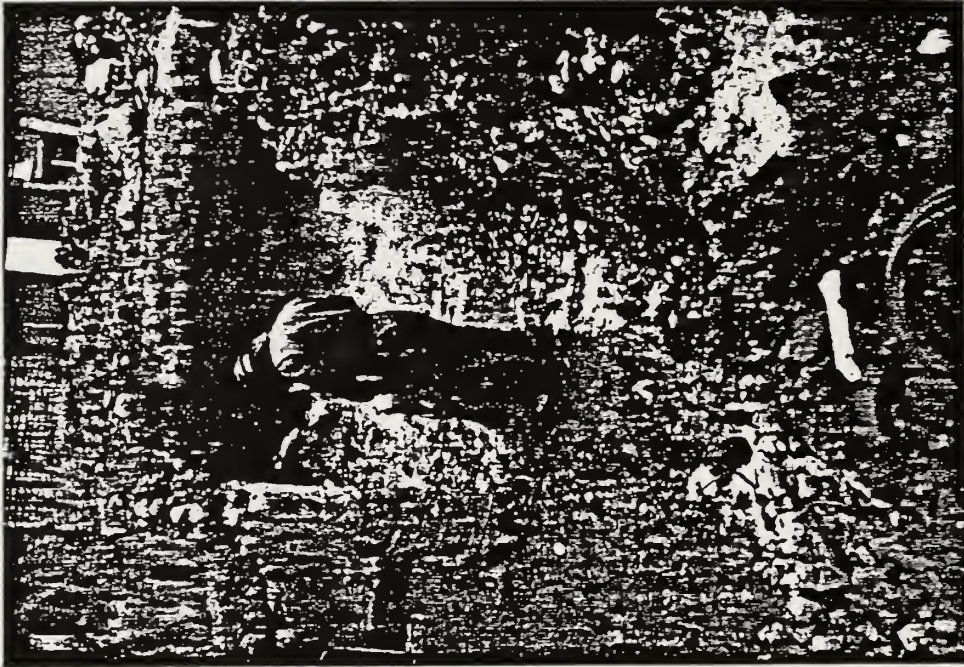


Fig. 3.10 Preparing the Surface of the Pile

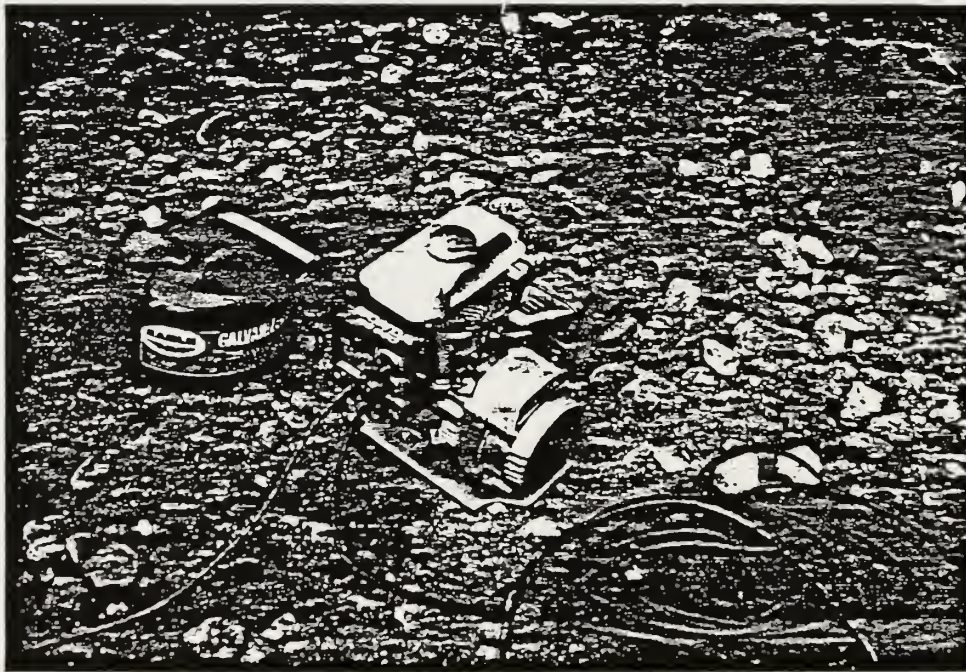


Fig. 3.11 Power Supply for Test

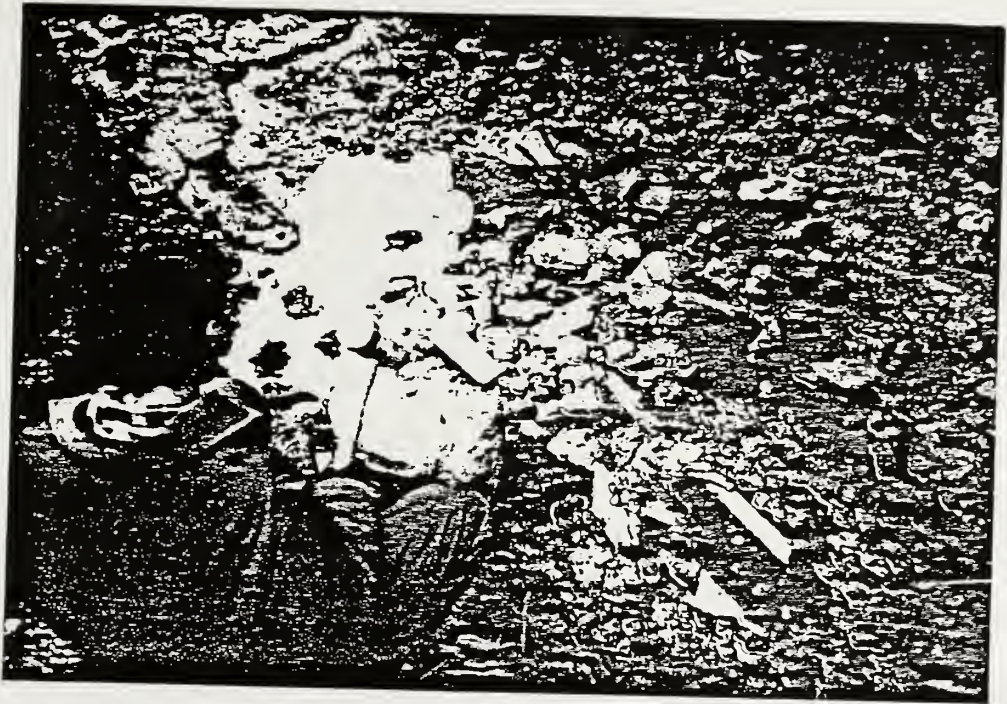


Fig. 3.12 Impacting the pile

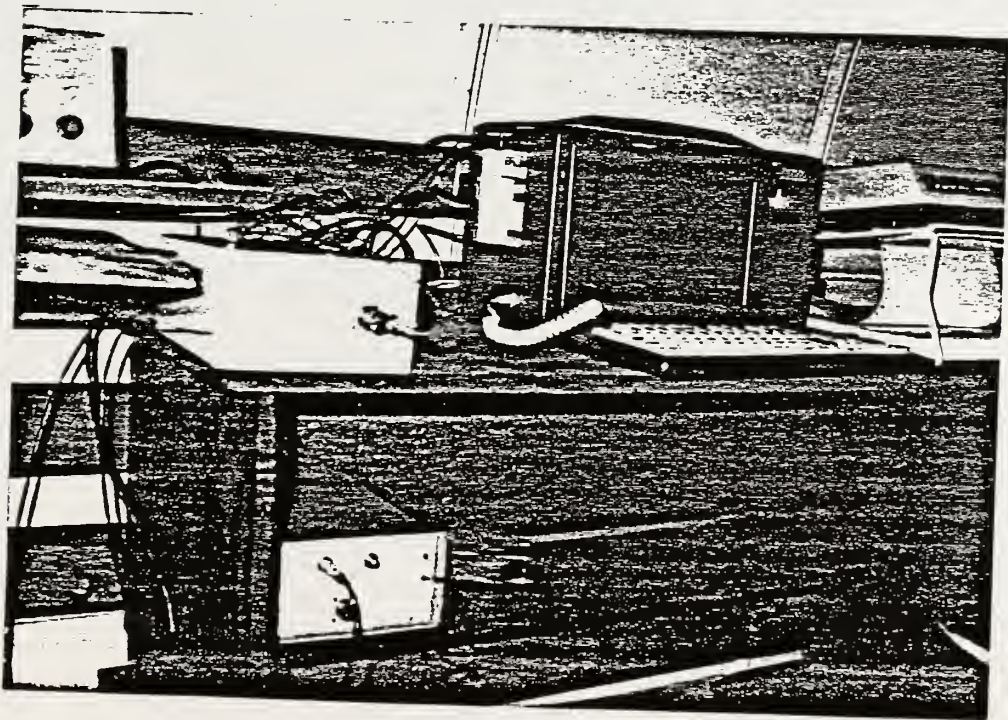


Fig 3.13 Electronic Pile Test Eguipment

Time = 0.00000E+00 Time step = 0



Fig. 4.1 Mesh of a Single pile

Time = 0.00000E+00 Time step = 0



Fig. 4.2 Triangular Finite Elements

Time = 0.00000E+00 Time step = 0

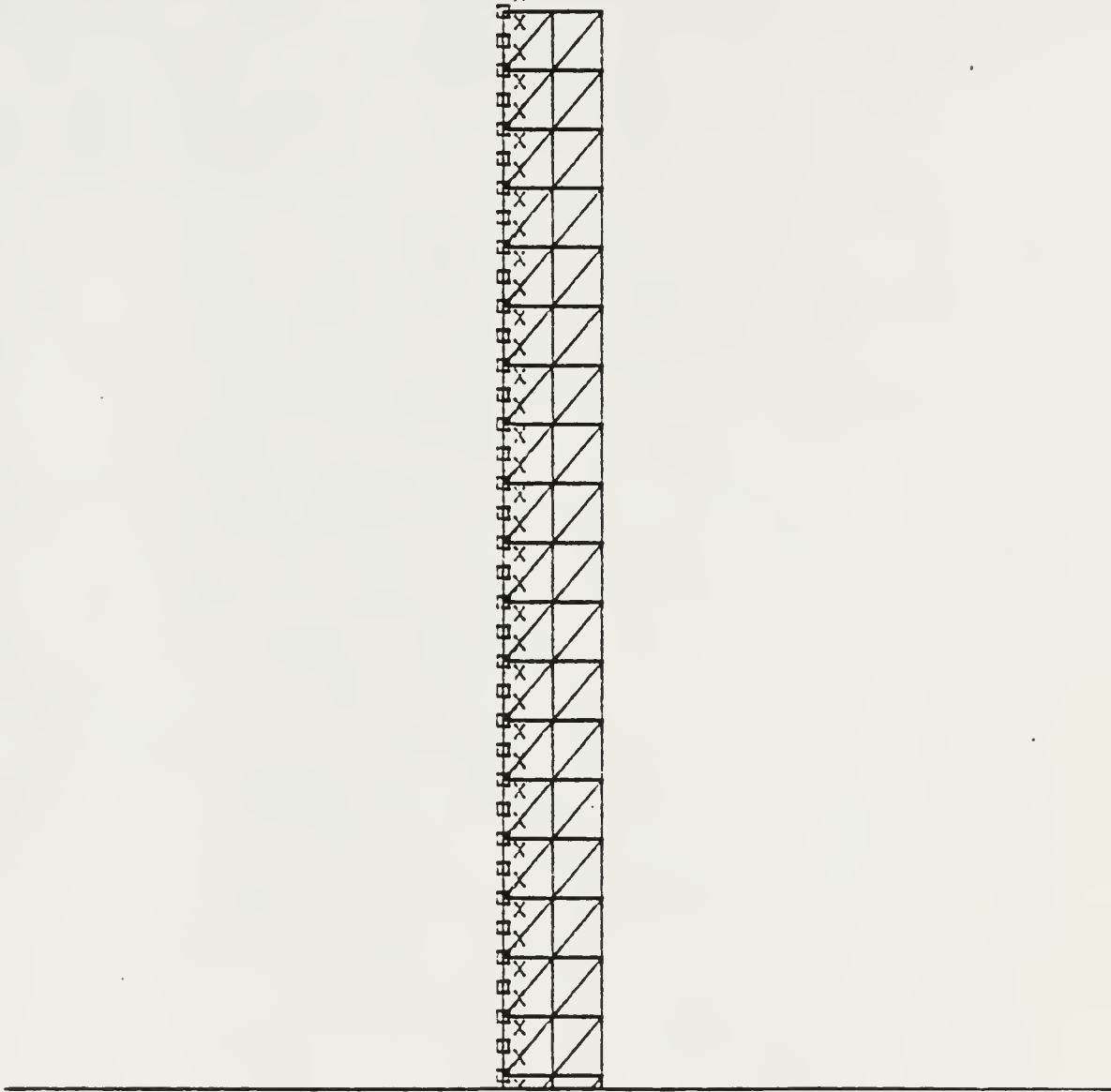


Fig. 4.3 Boundary Condition of a Single Pile

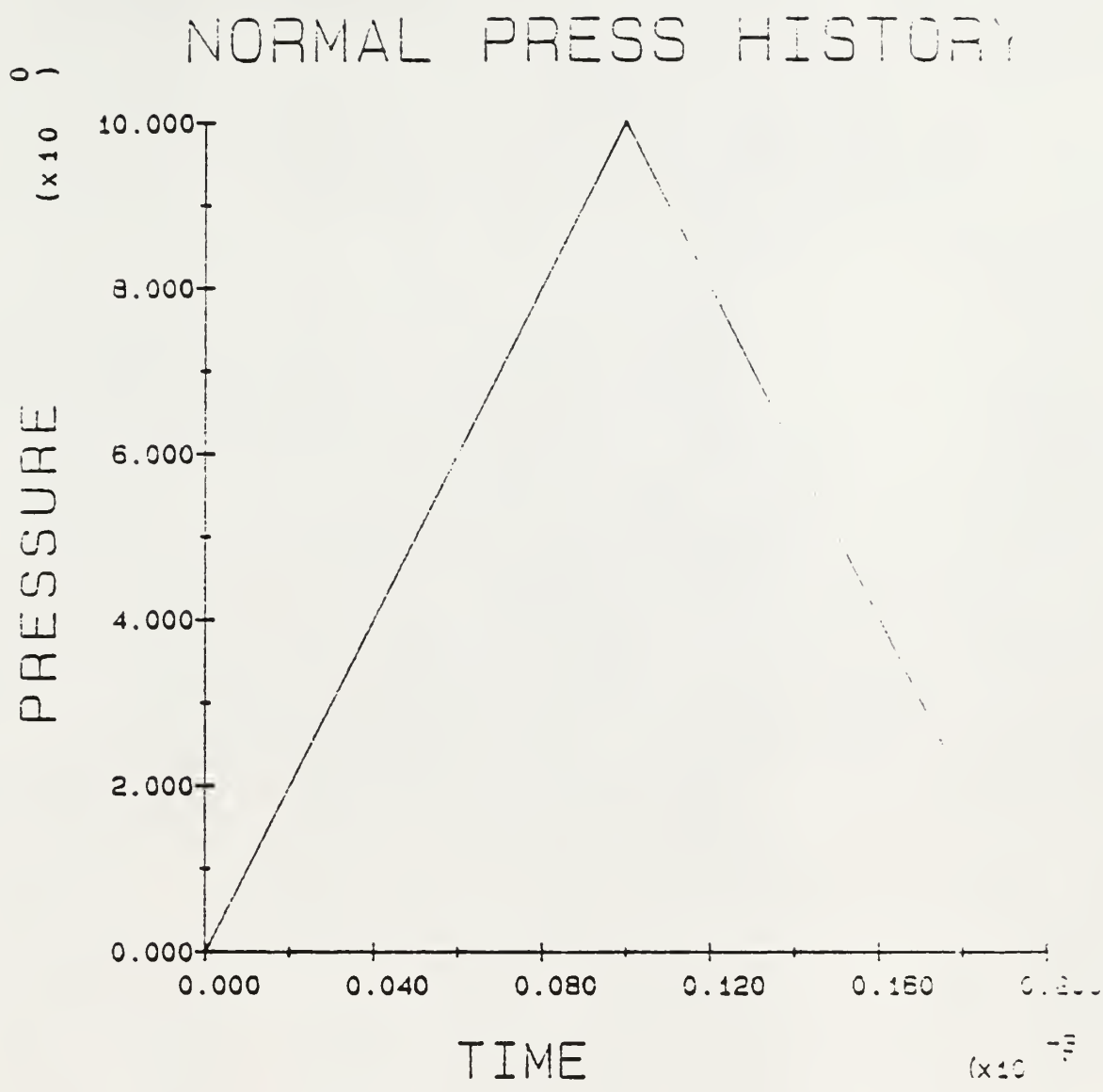


Fig. 4.4 Impulse

NODE NUMBER 300

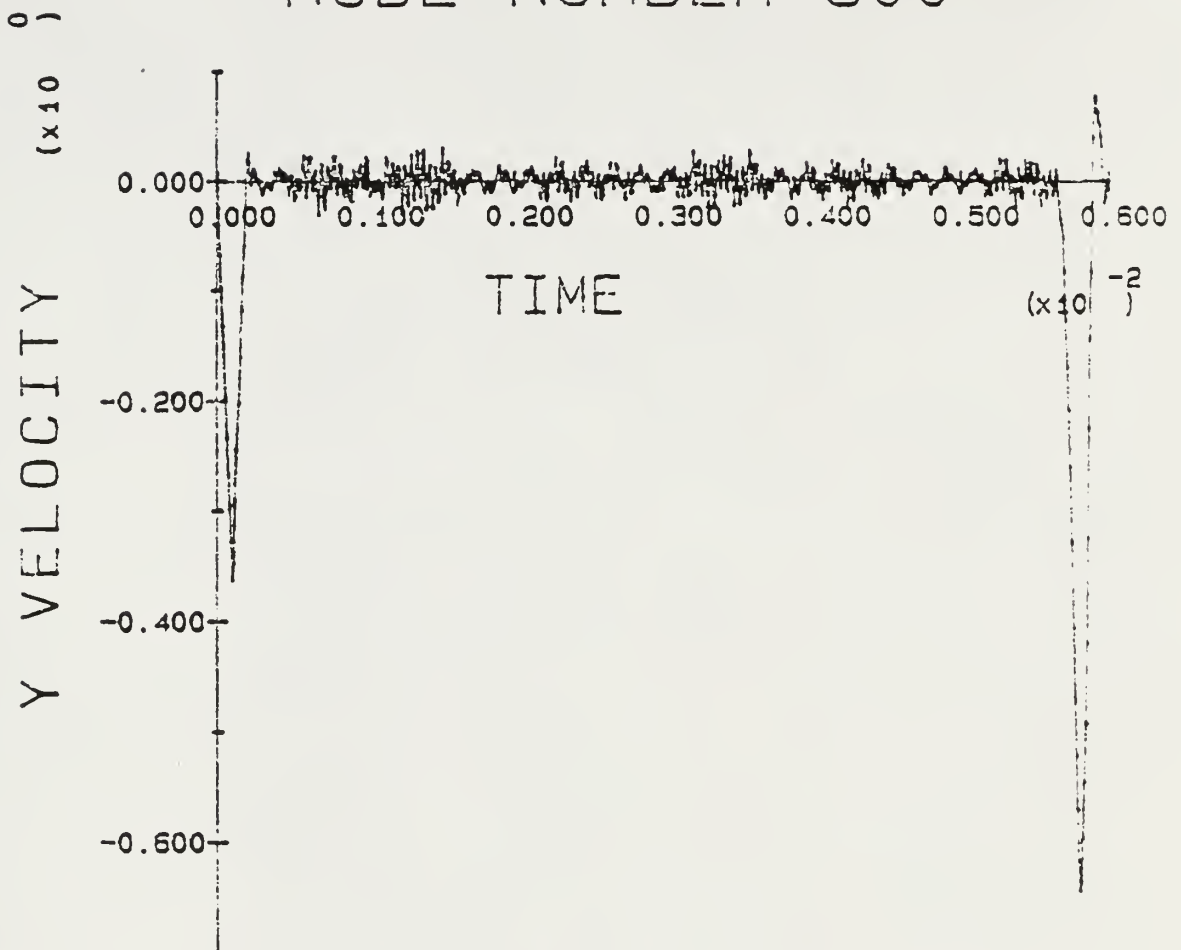


Fig. 4.5 Responce at the Top of a Sound Pile

NODE NUMBER 255

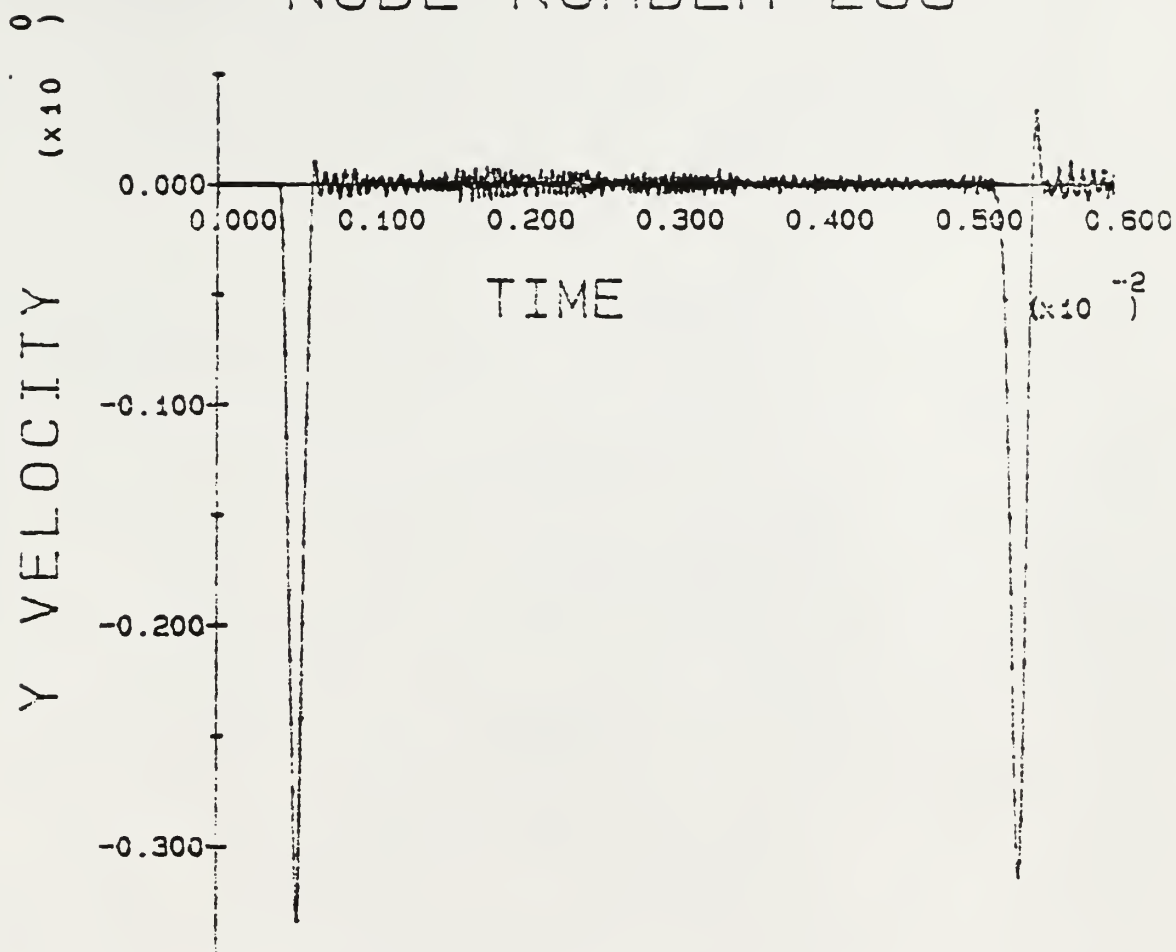


Fig. 4.6 Responce in the Up-Middle of a Sound Pile

NODE NUMBER 55

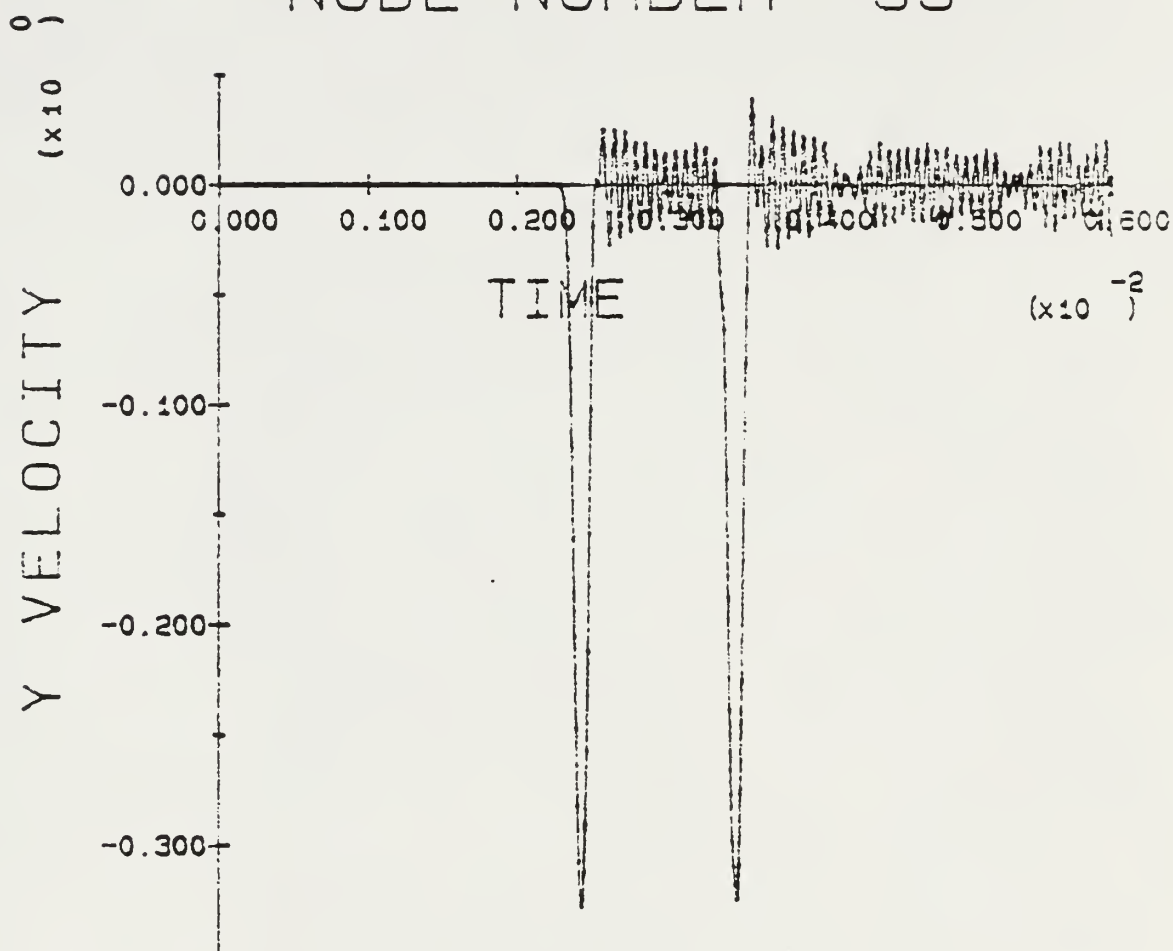


Fig. 4.7 Responce in the Down-Middle of a Sound Pile

NODE NUMBER 3

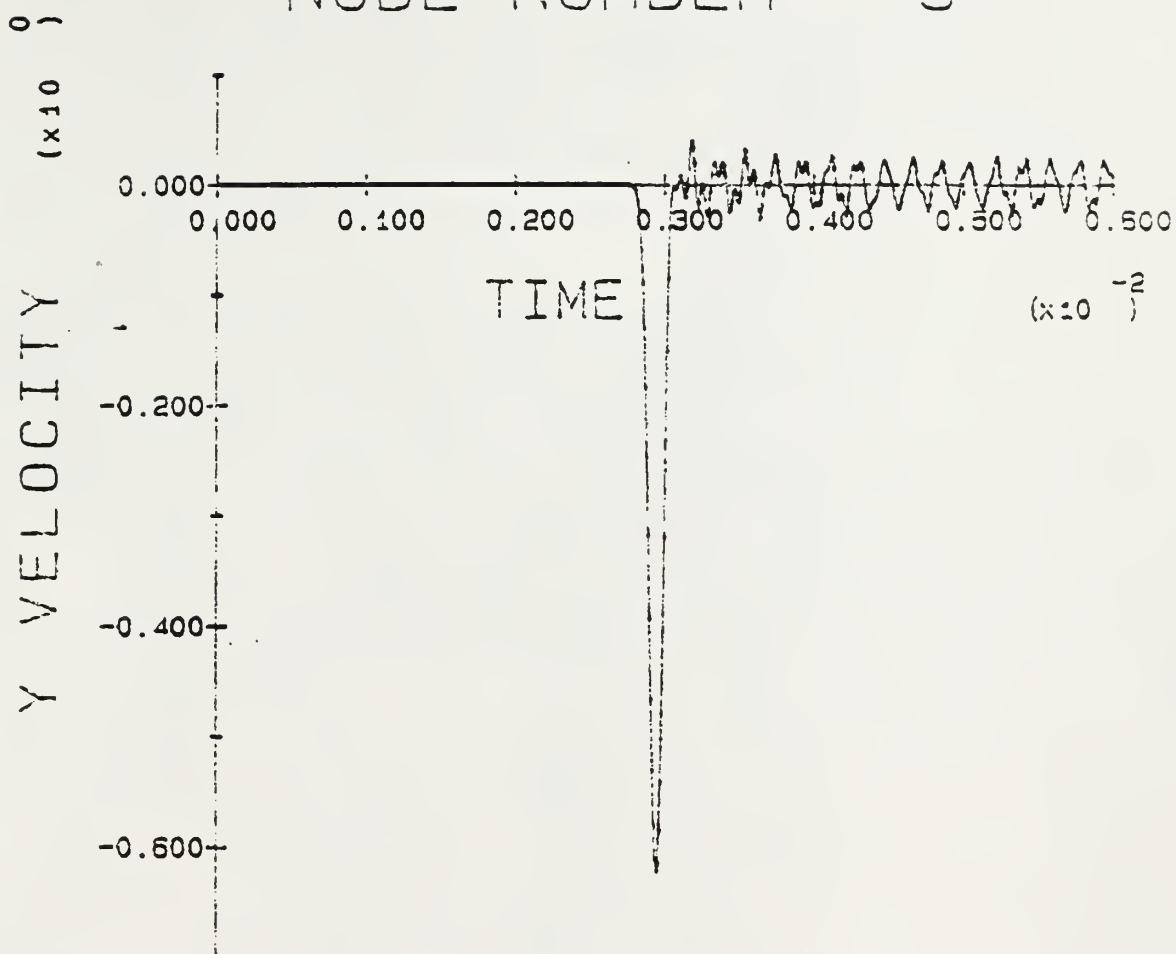


Fig. 4.8 Responce at the Bottom of a Sound Pile

Time = 0.00000E+00 Time step = 0



Fig. 4.9 Crack Position

Time = 0.00000E+00

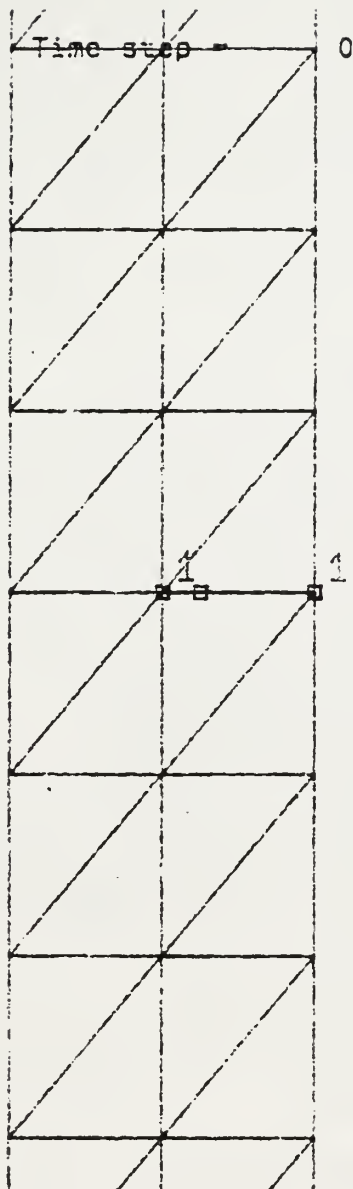


Fig. 4.10 Mesh of Crack

NODE NUMBER 303

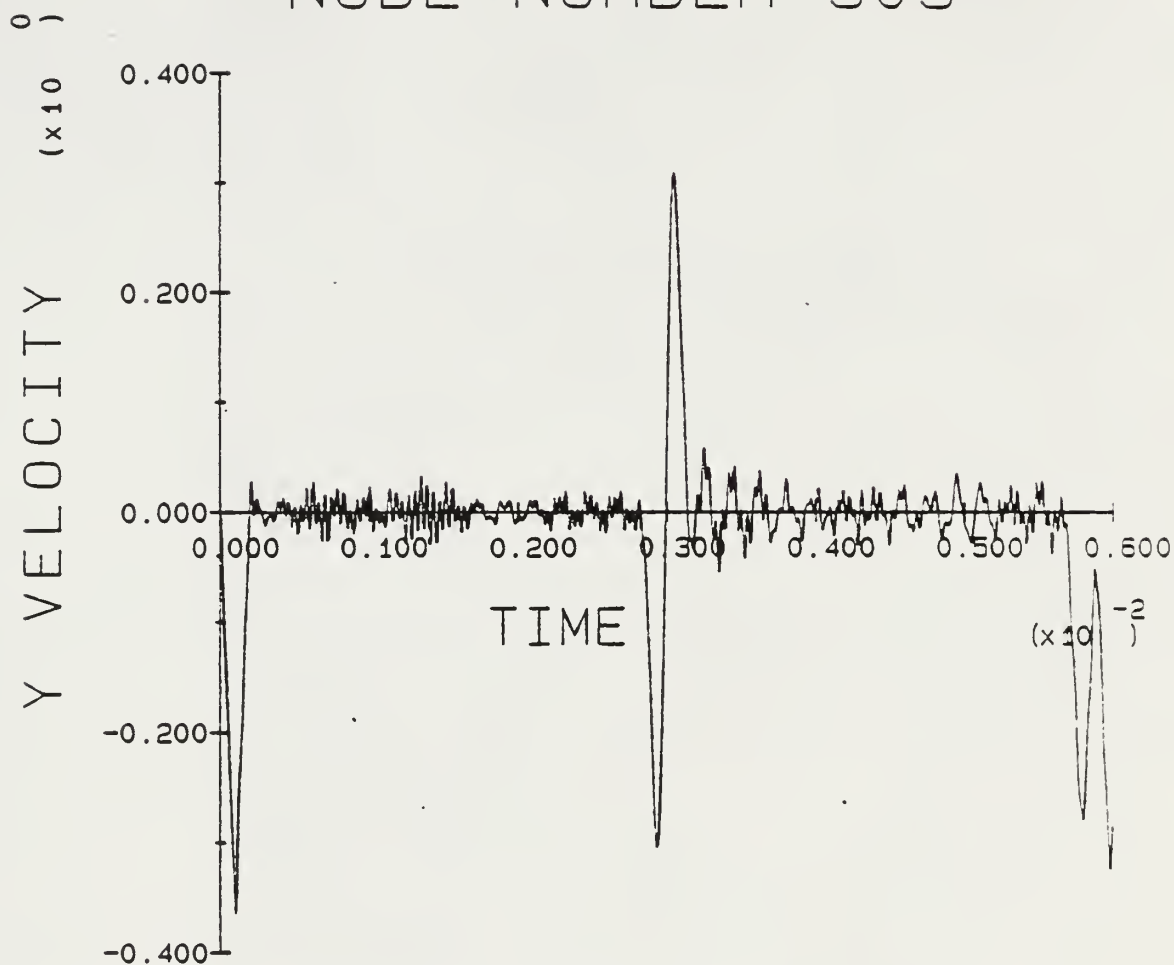


Fig. 4.11 Responce on the Top of the Pile
with Crack in the Middle

NODE NUMBER 179

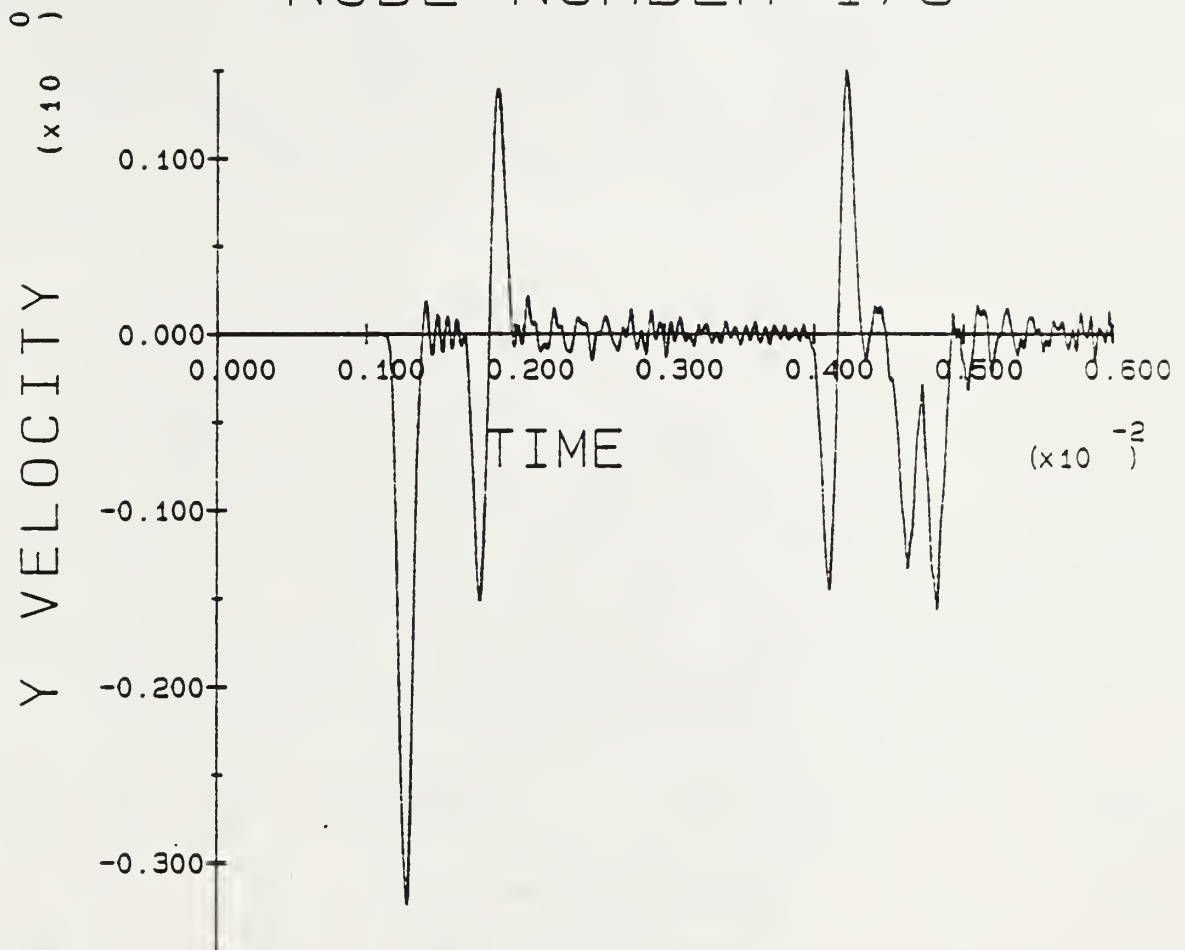


Fig. 4.12 Response in the Pile above the Crack

NODE NUMBER 153

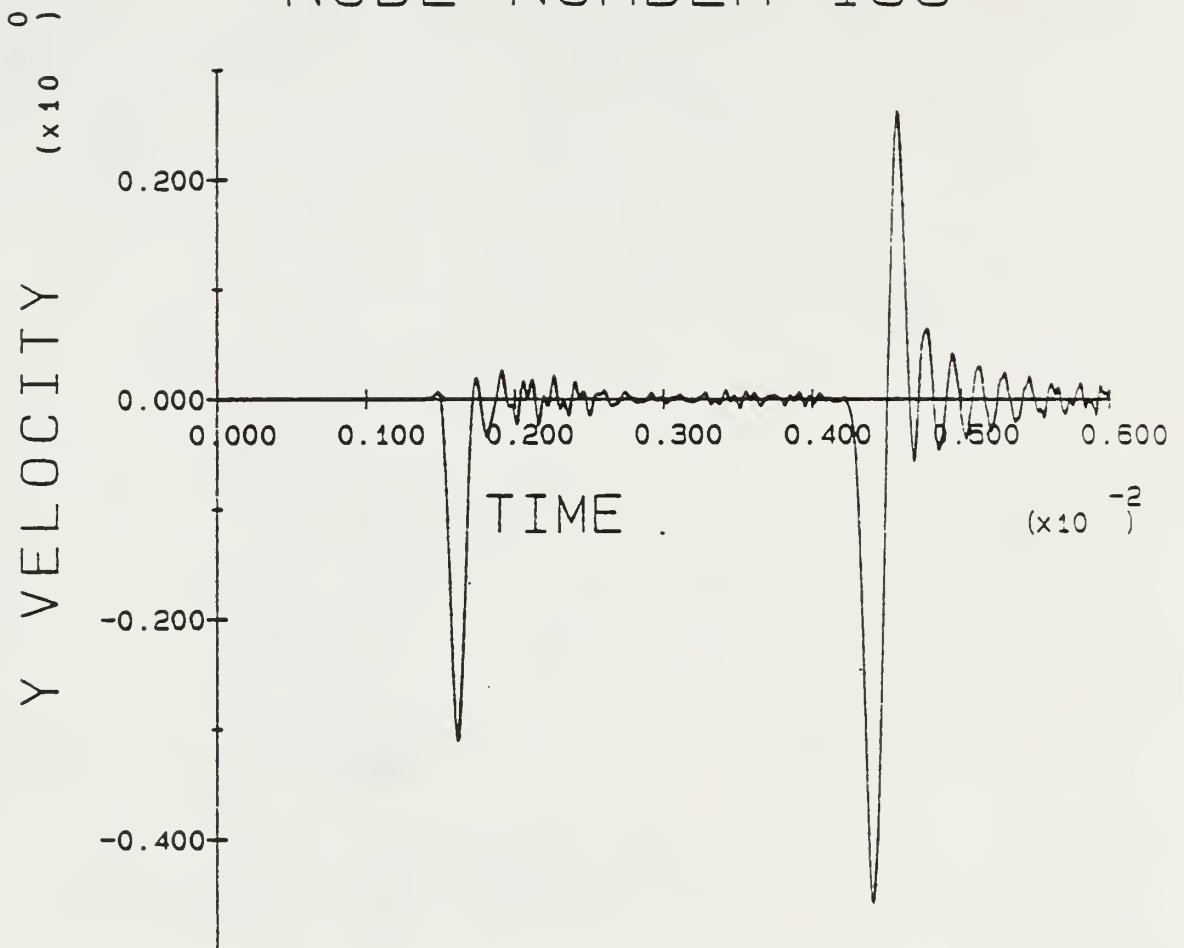


Fig. 13 Responce at the Crack

NODE NUMBER 68

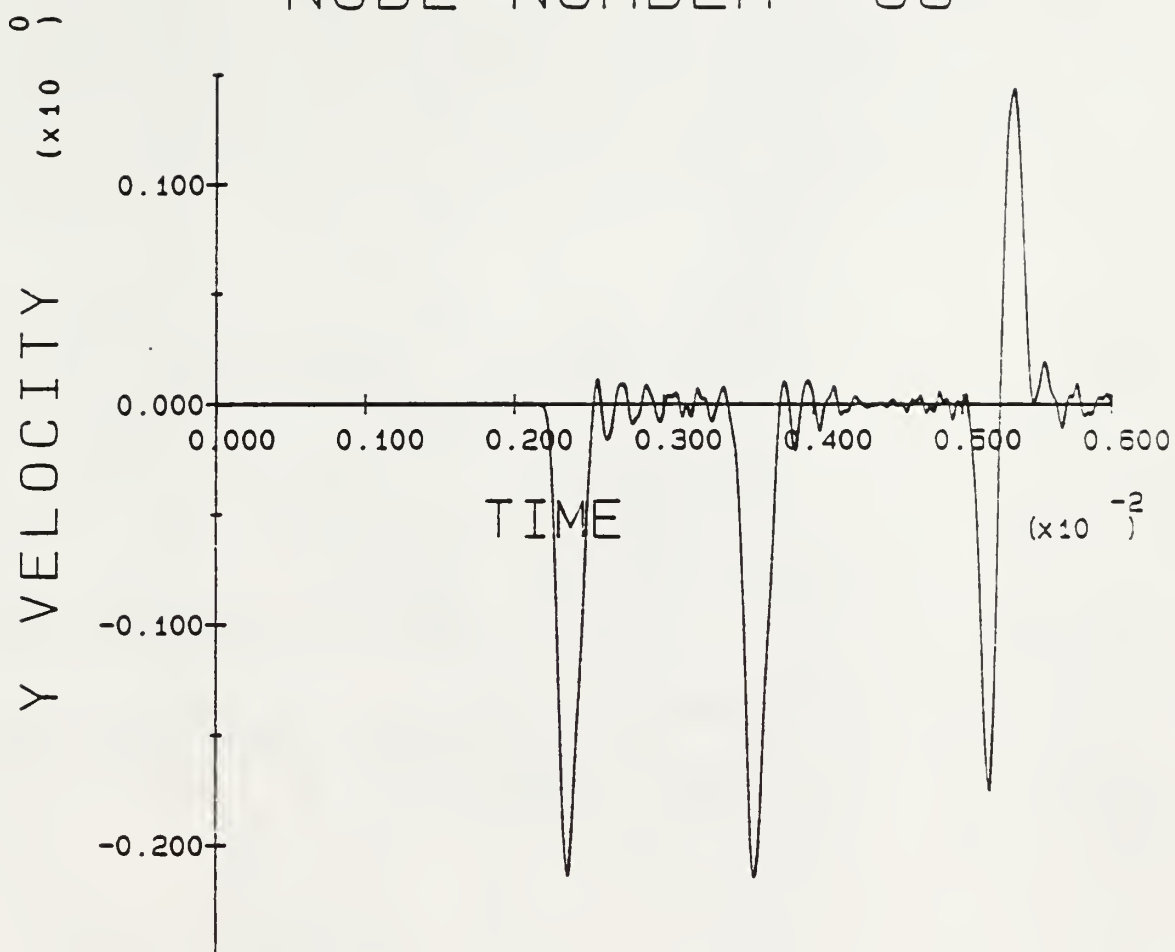


Fig. 4.14 Response in the Pile Below the Crack

NODE NUMBER 3

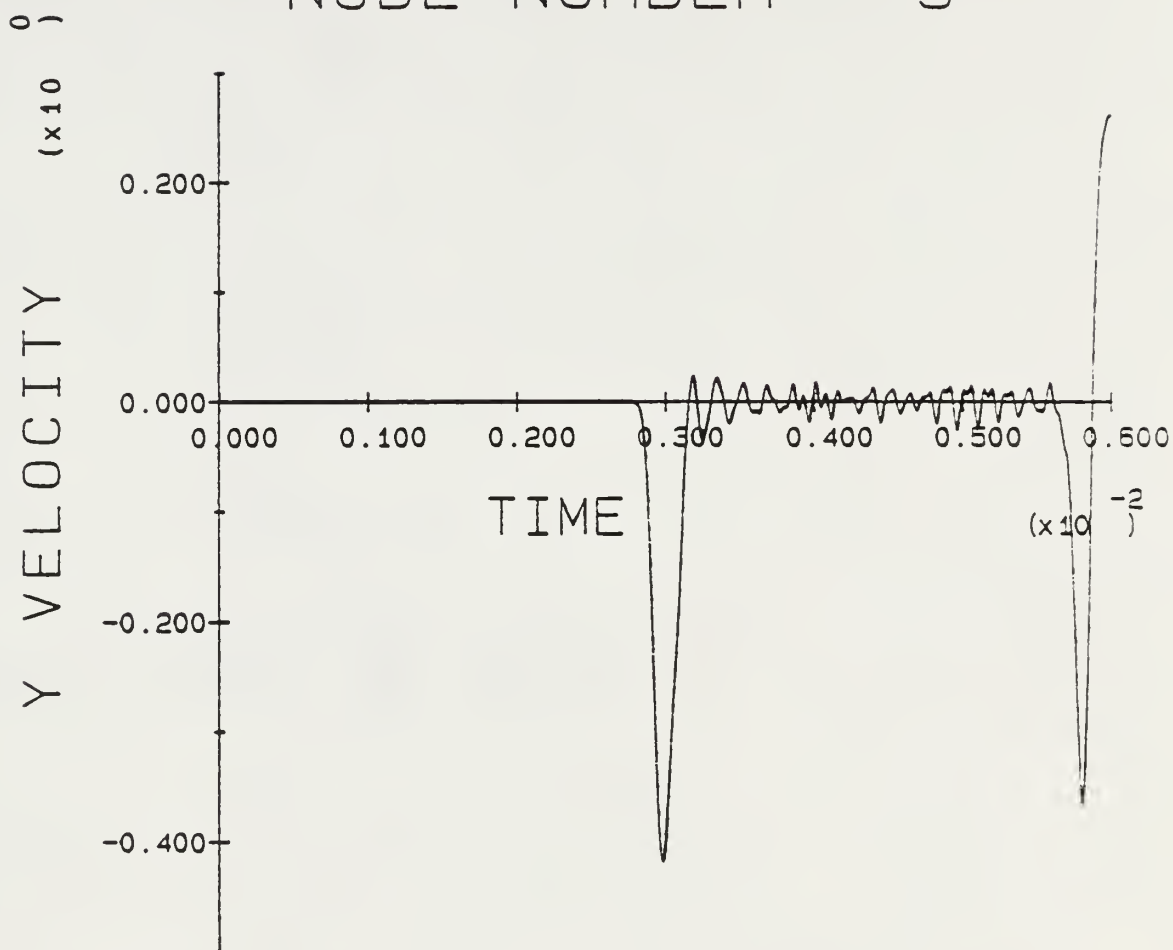


Fig. 4.15 Responce at the Bottom of the Pile
with the Crack in the Middle

Time = 0.70033E-02 Time step = 1546



Fig. 4.16 Mesh of the Void

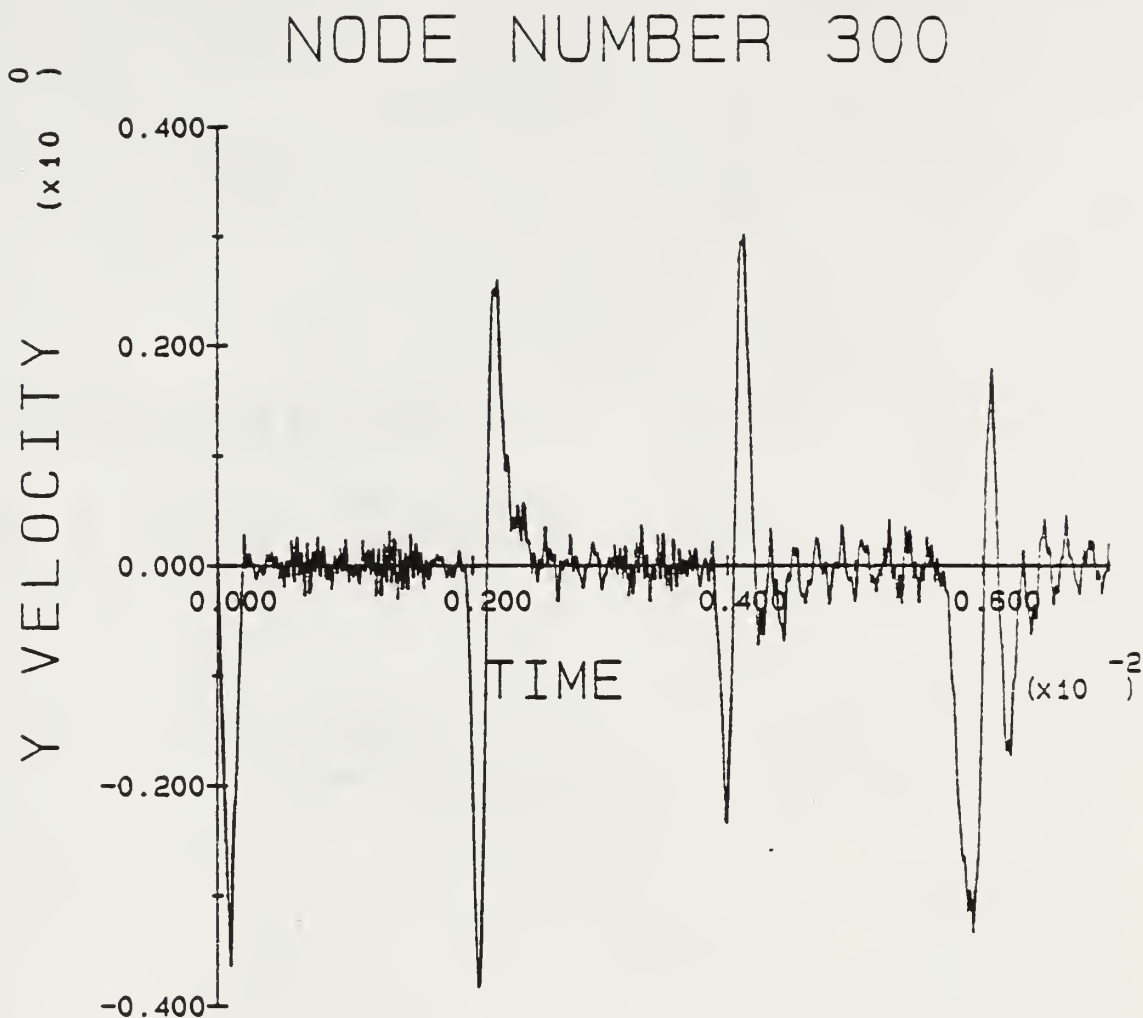


Fig. 4.17 Responce on the Top of the Pile with Void

NODE NUMBER 198

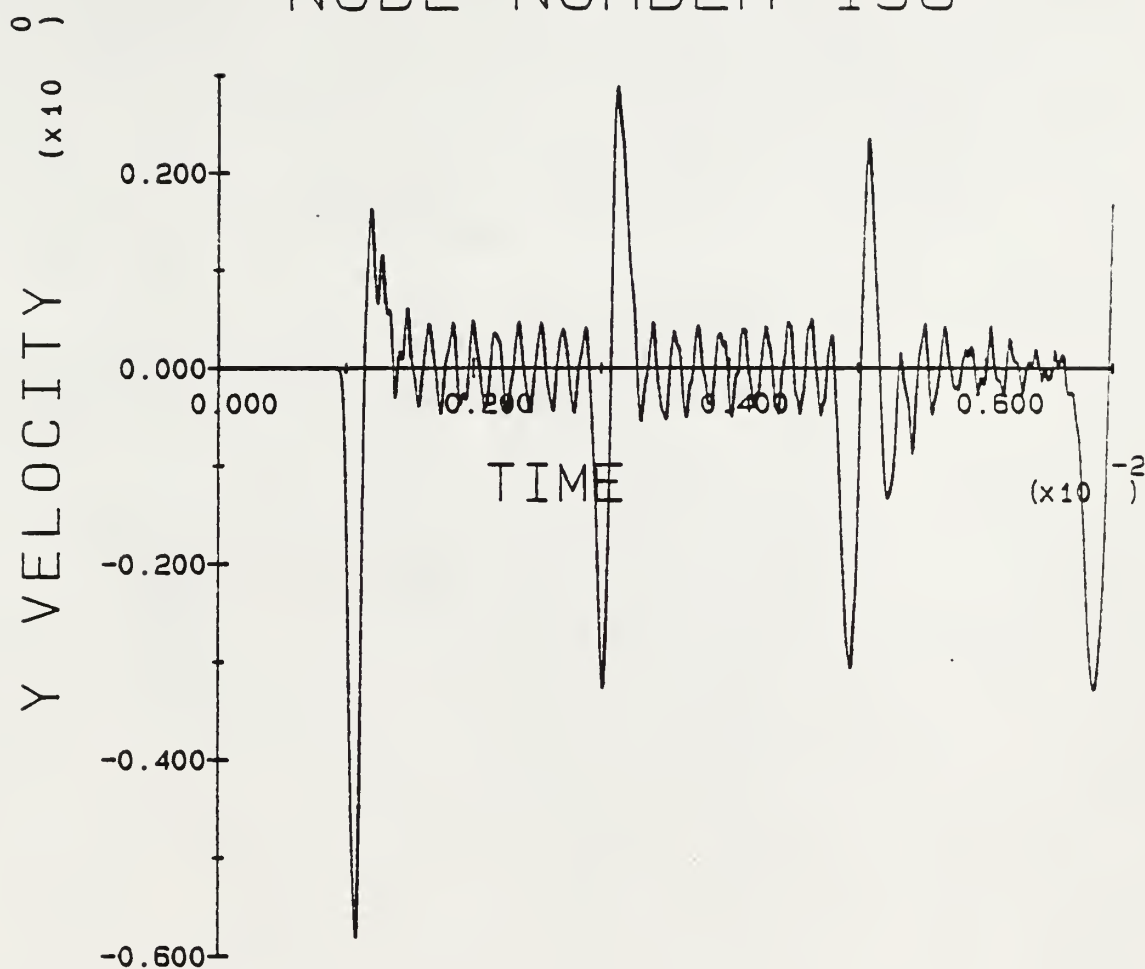


Fig. 4.18 Responce at the Upside of the Void

NODE NUMBER 195

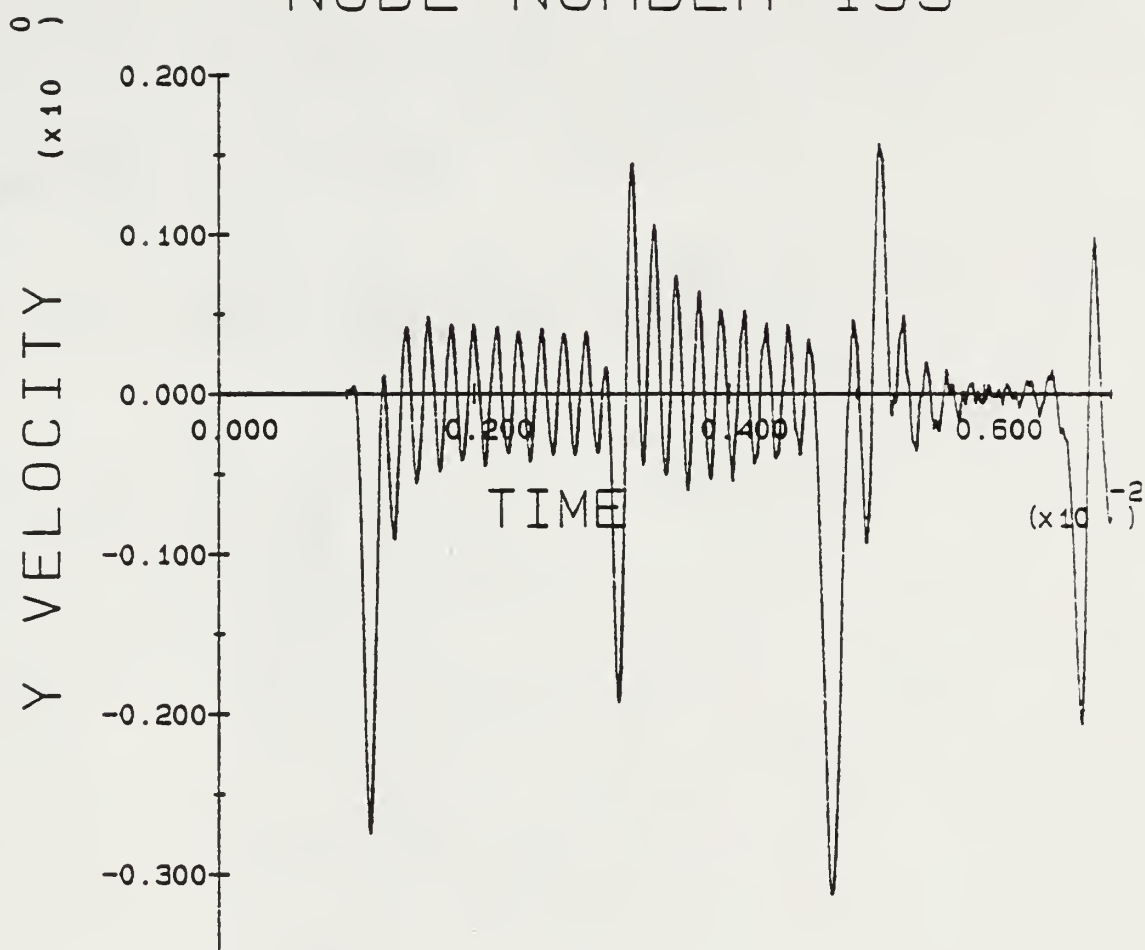


Fig. 4.19 Responce at the Downside of the Void

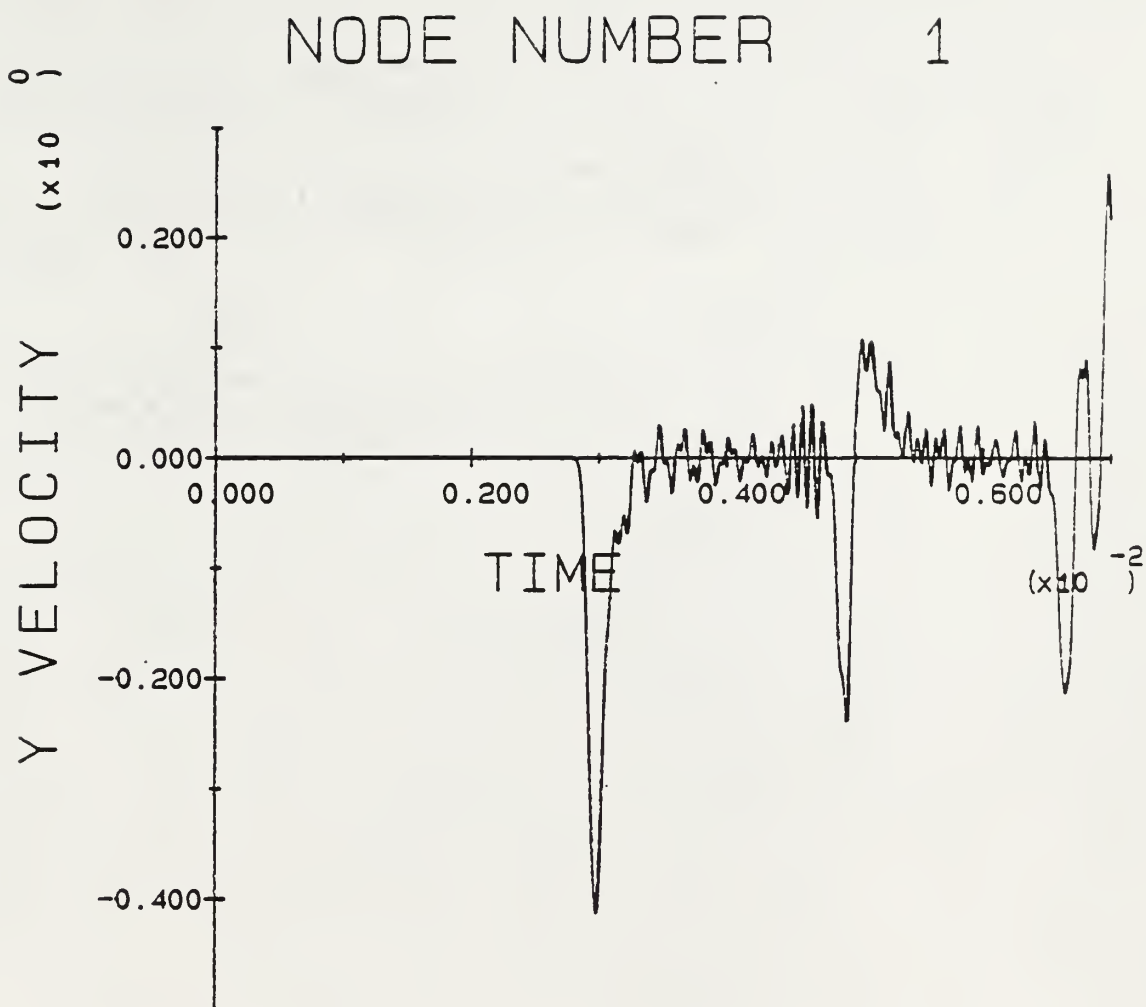


Fig. 4.20 Responce at the Bottom of the Pile with Void

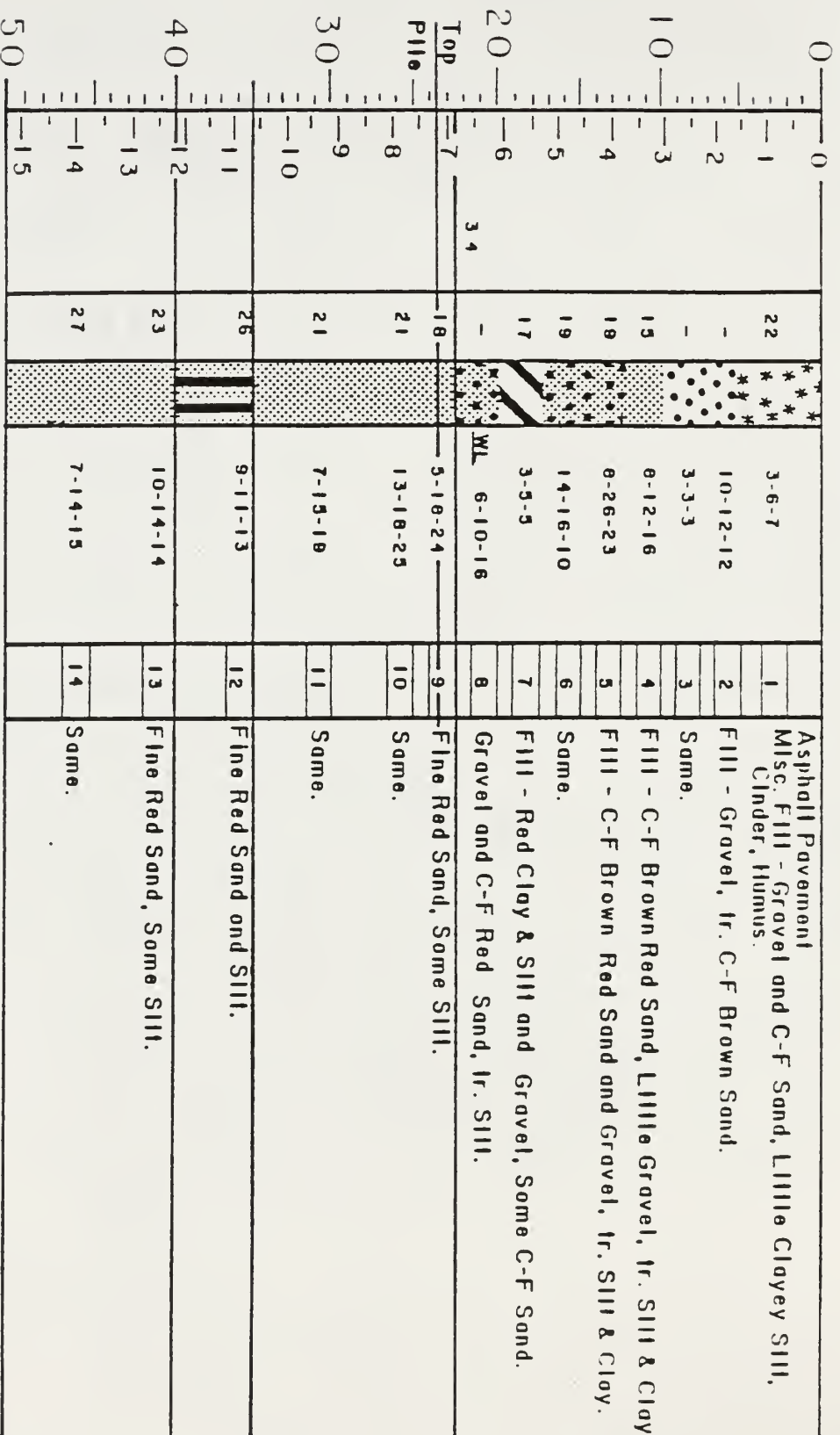


Fig. 4.21 Soil Conditions in Newark, New Jersey

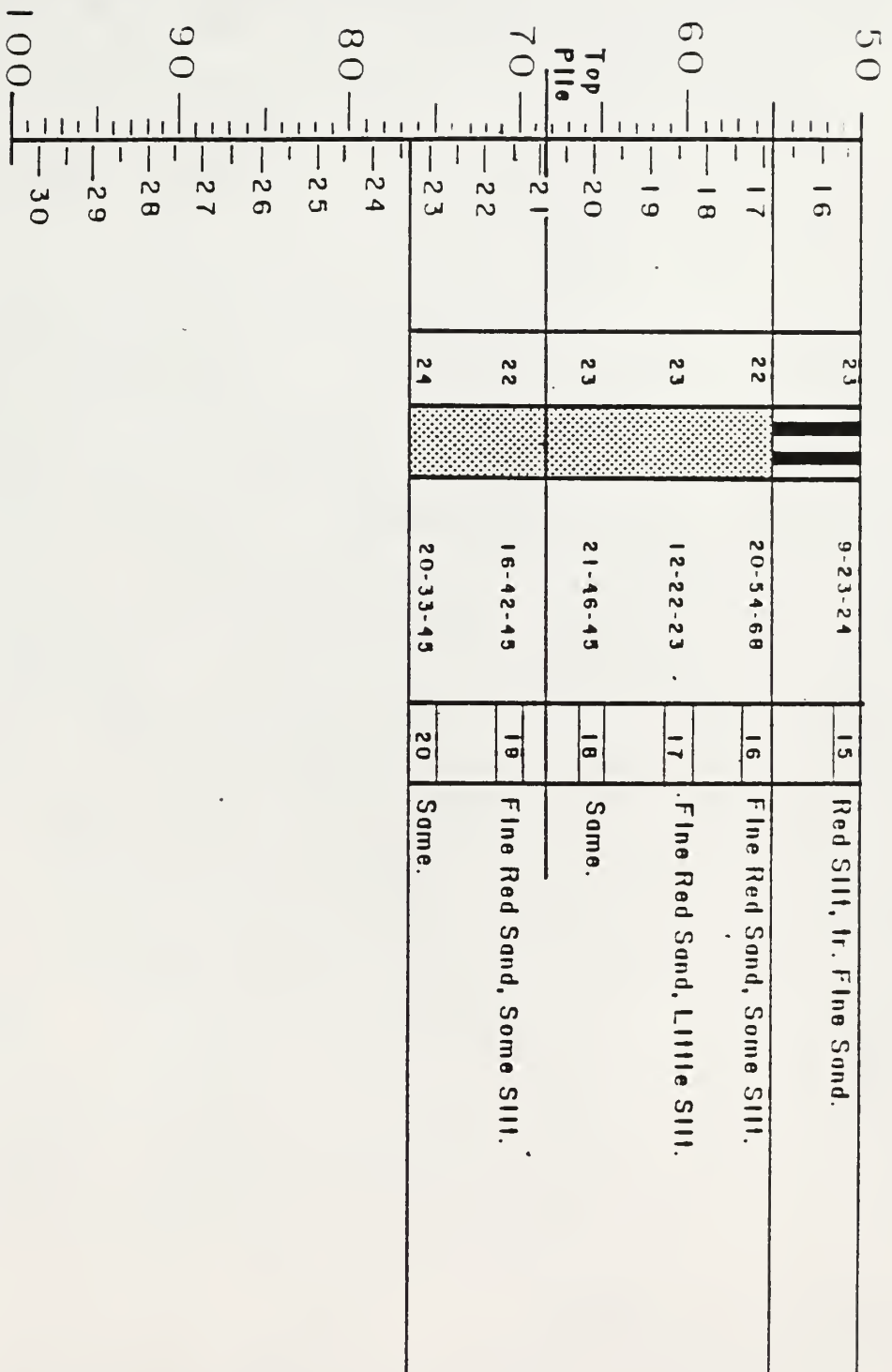


Fig. 4.22 Soil Conditions in Newark, New Jersey (continuous)

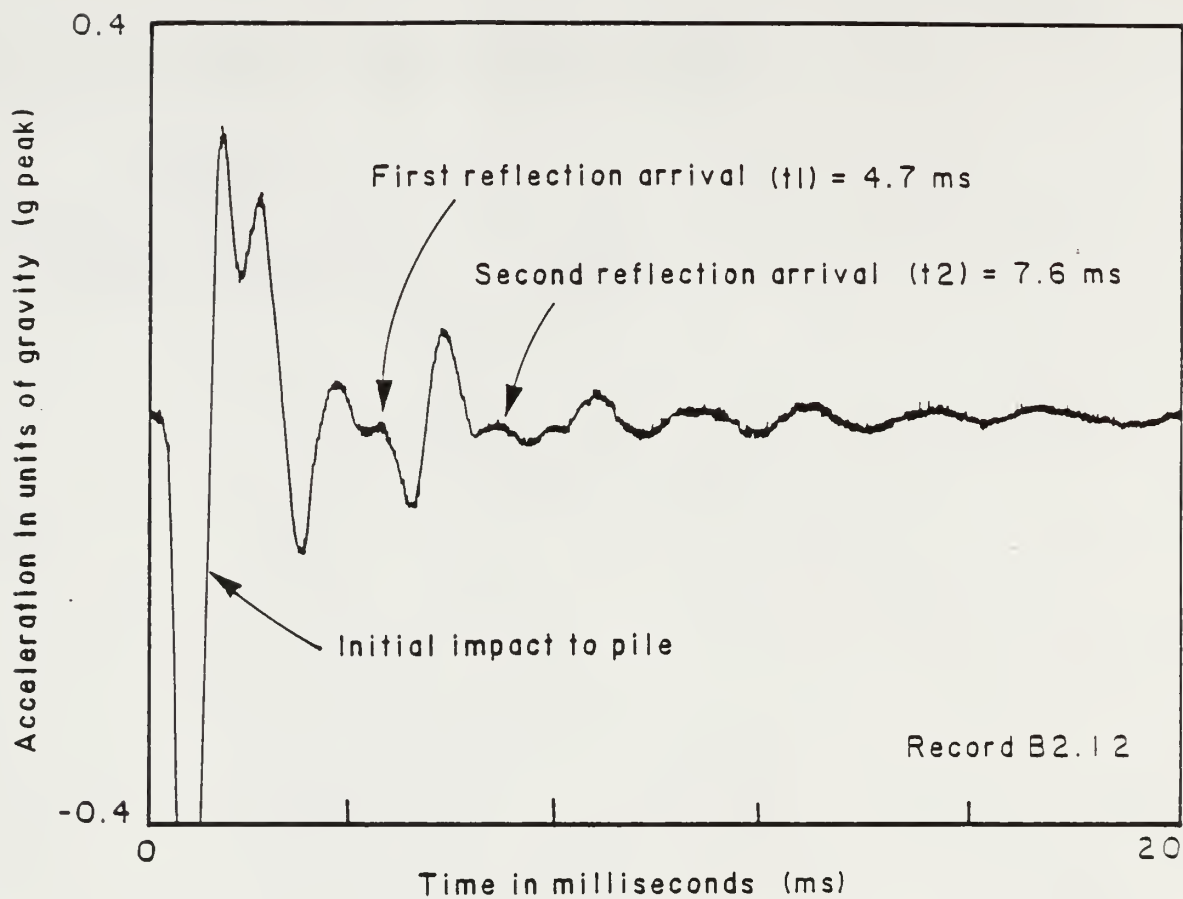


Fig. 4.23 Test Record for Pile 41

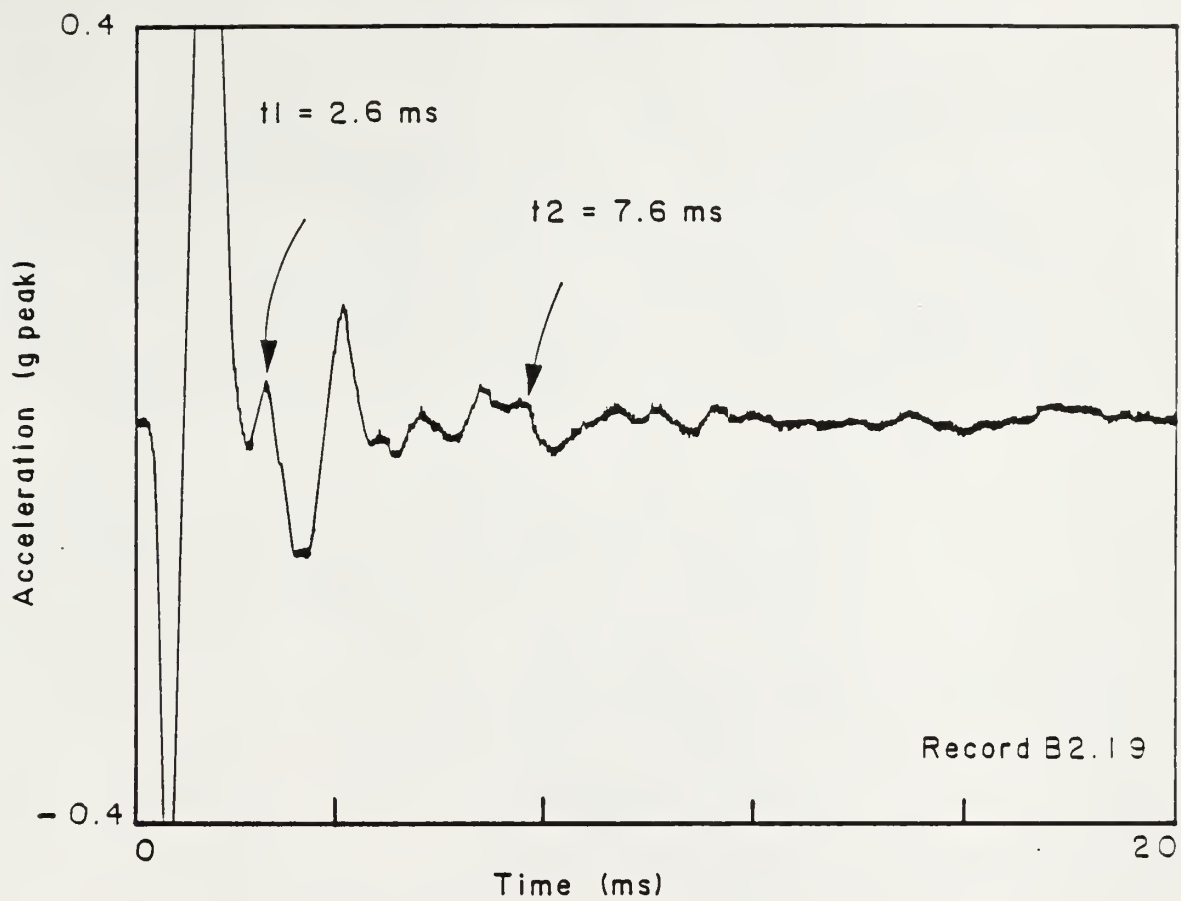


Fig. 4.24 Test Record for Pile 47

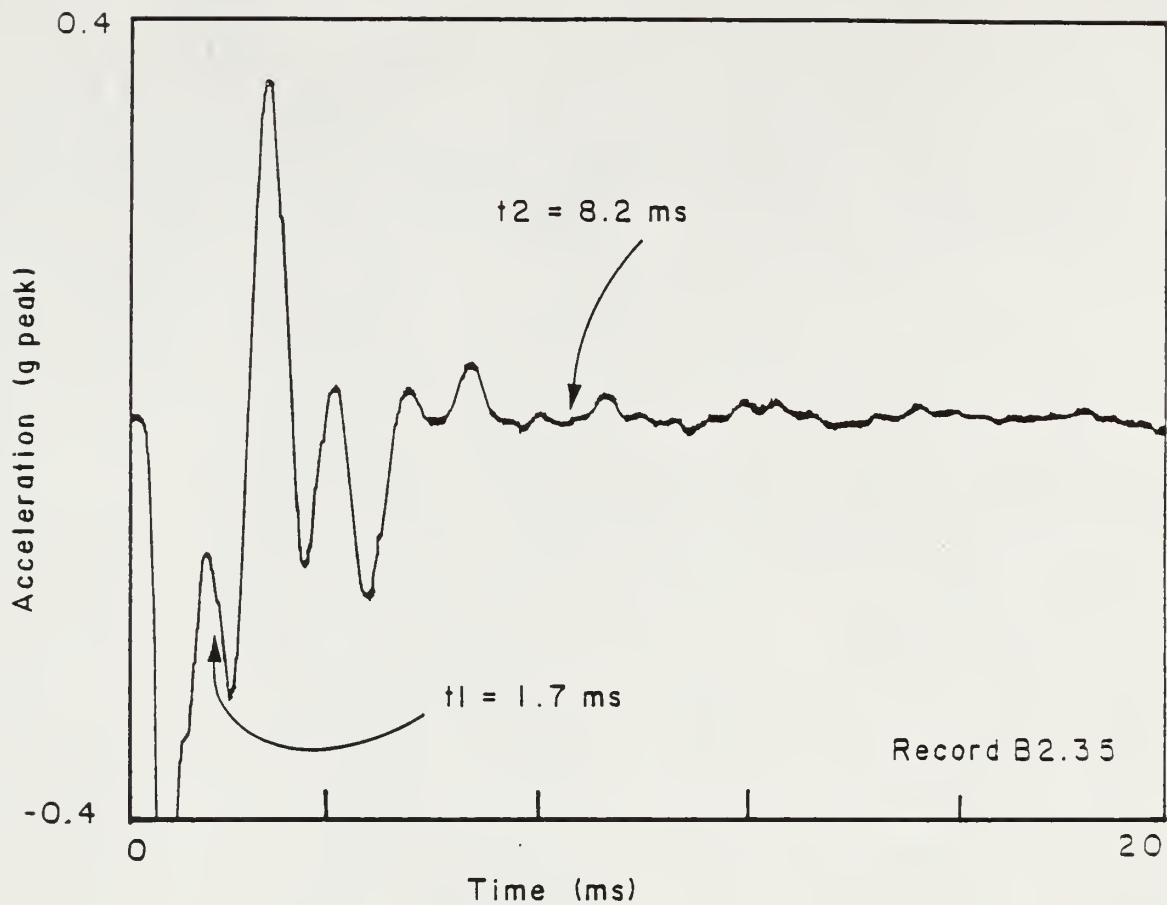


Fig. 4.25 Test Record for Pile 50

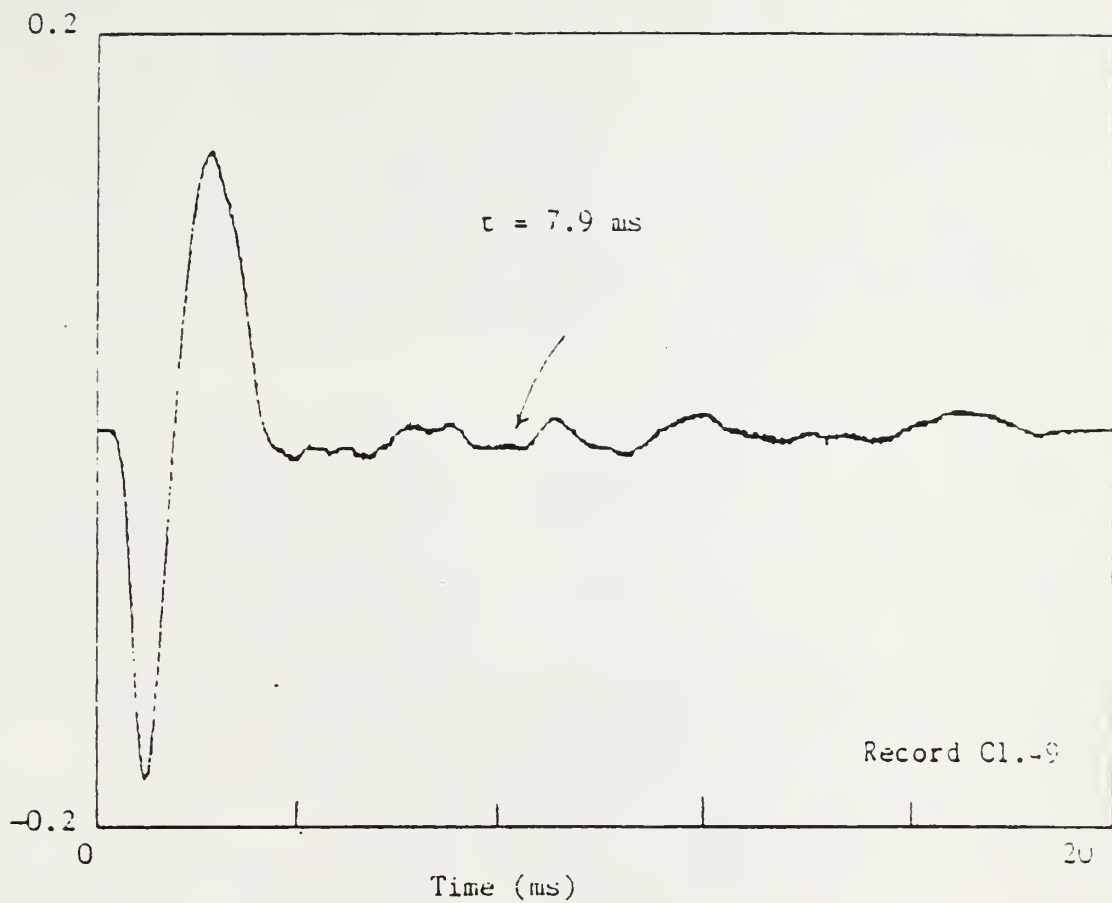


Fig. 4.26 Test Record for Pile 125

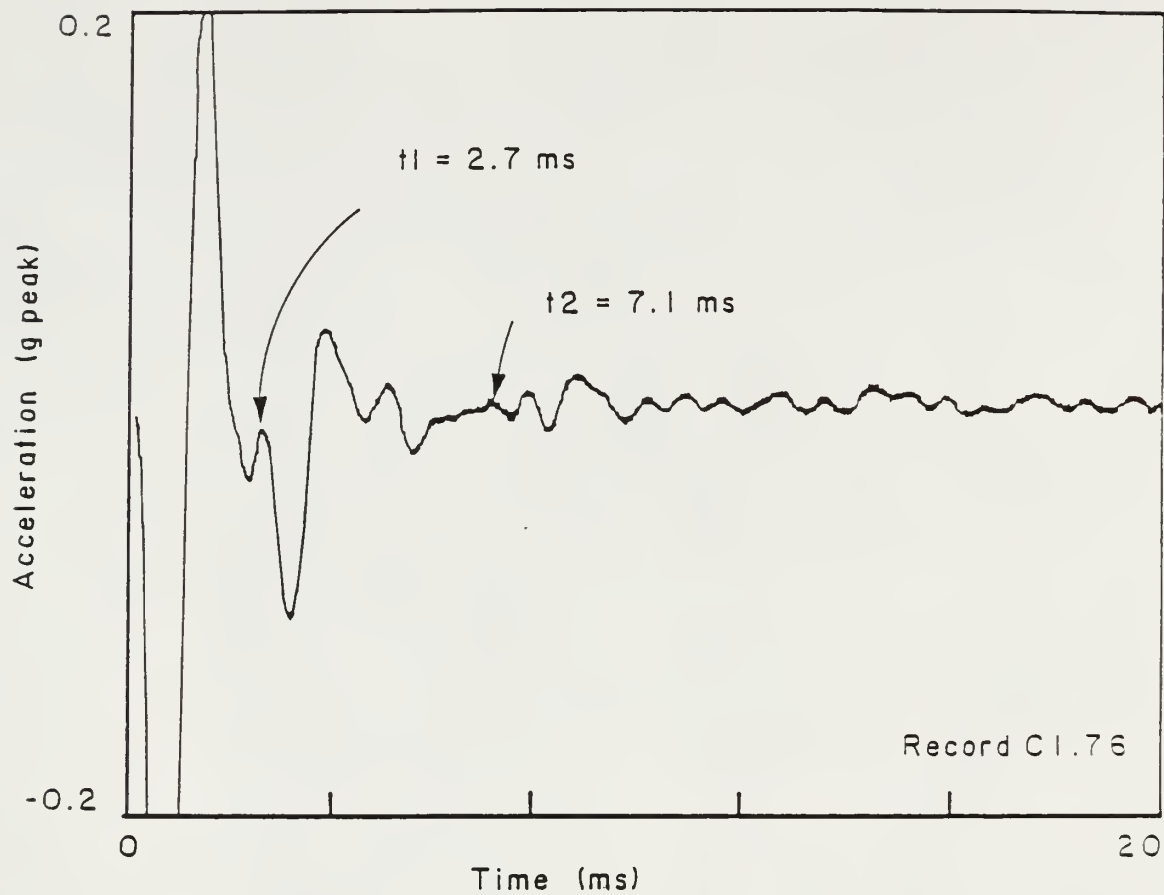


Fig. 4.27 Test Record for Pile 128

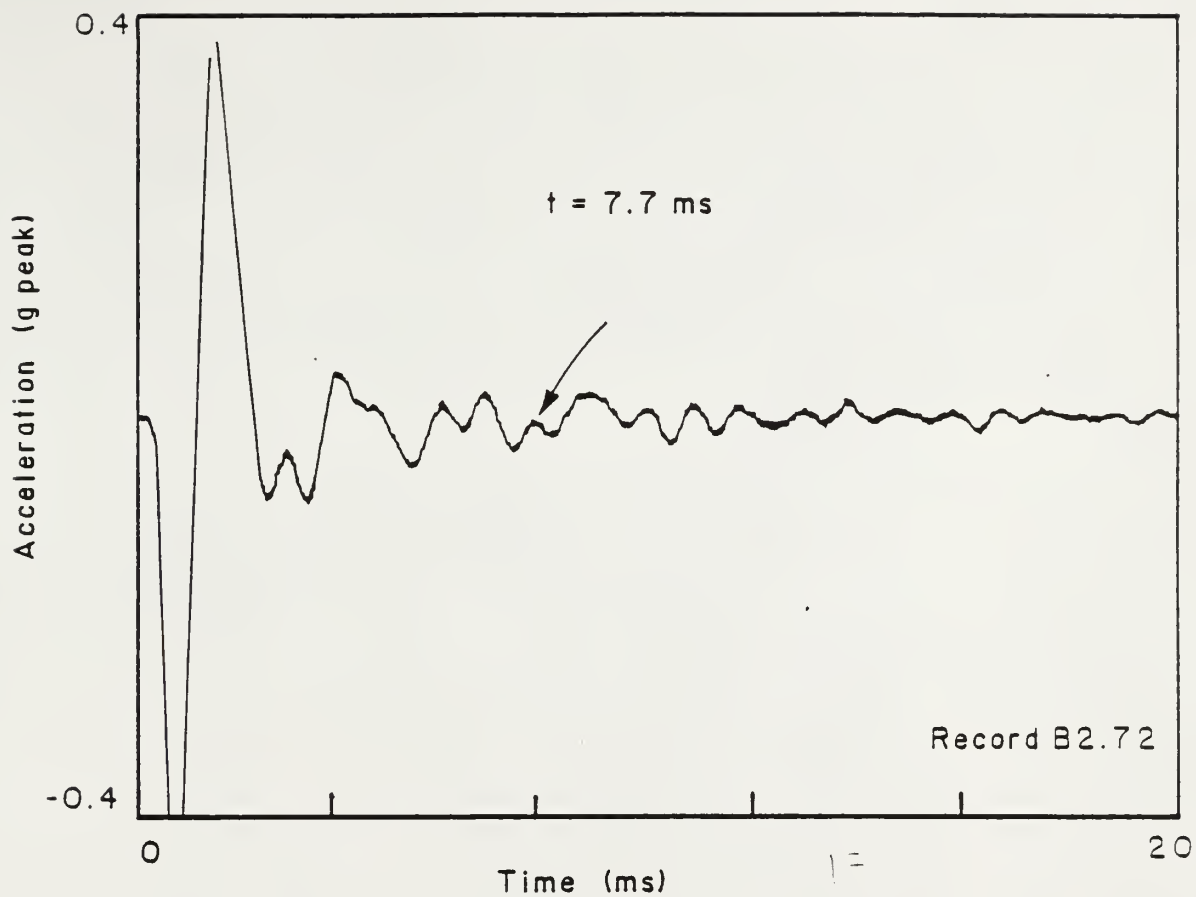


Fig. 4.28 Test Record for Pile 130

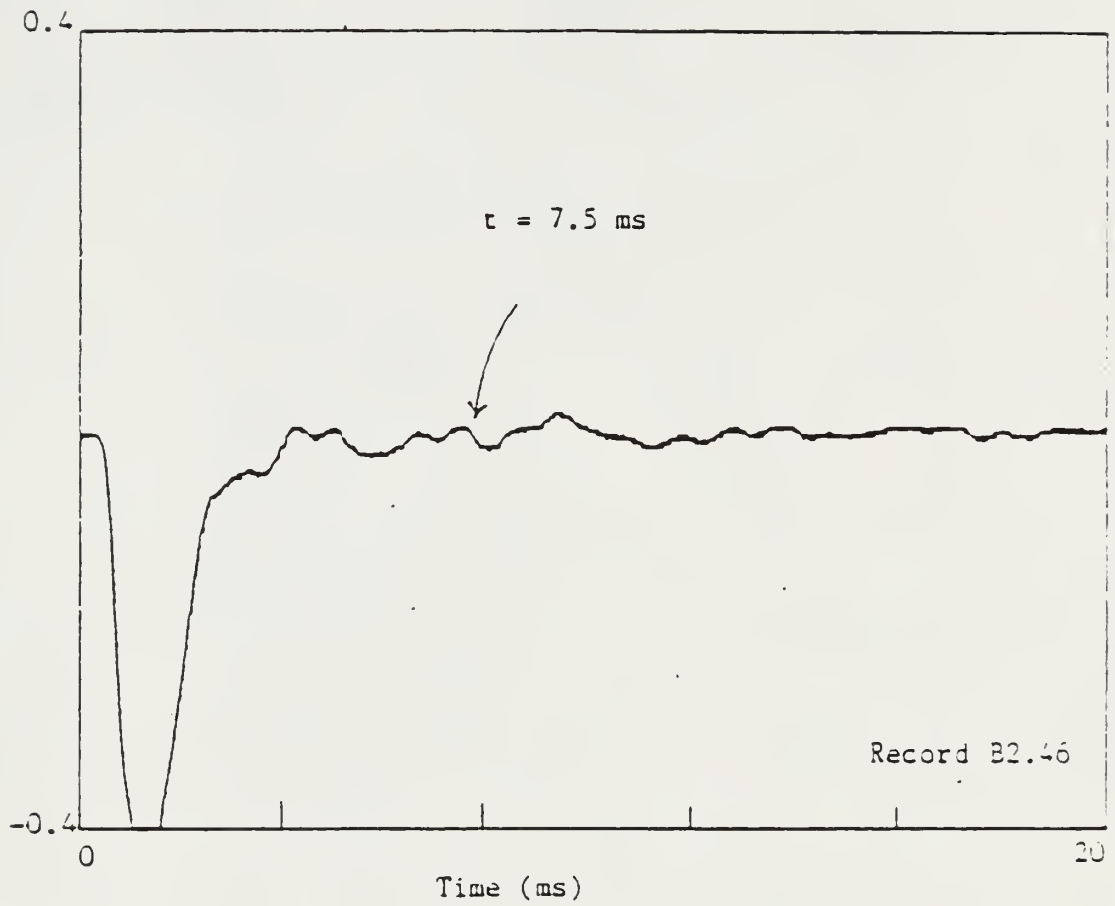


Fig. 4.29 Test Record for Pile 53

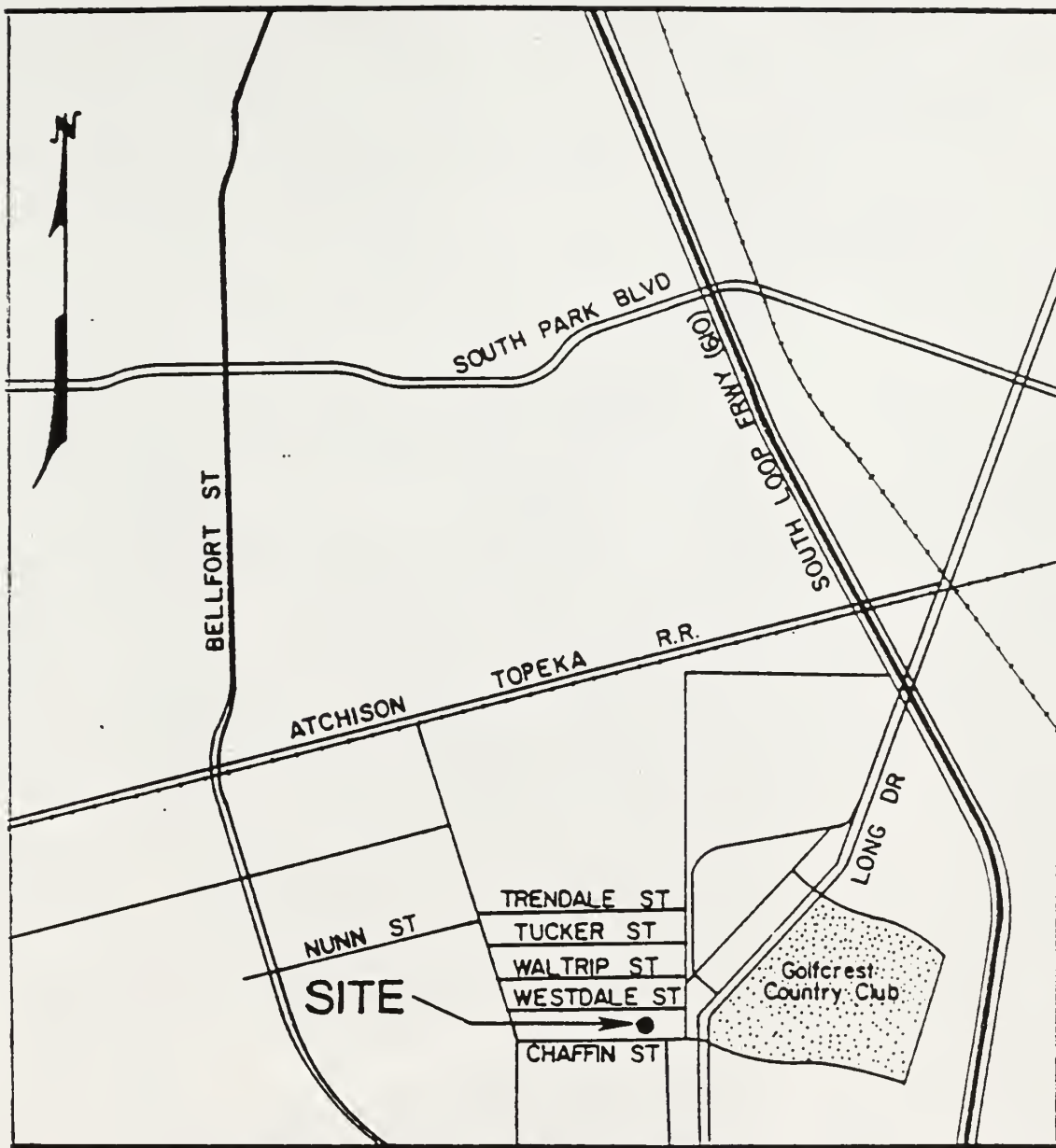


Fig. 4.30 The Location of Test at Houston, Texas

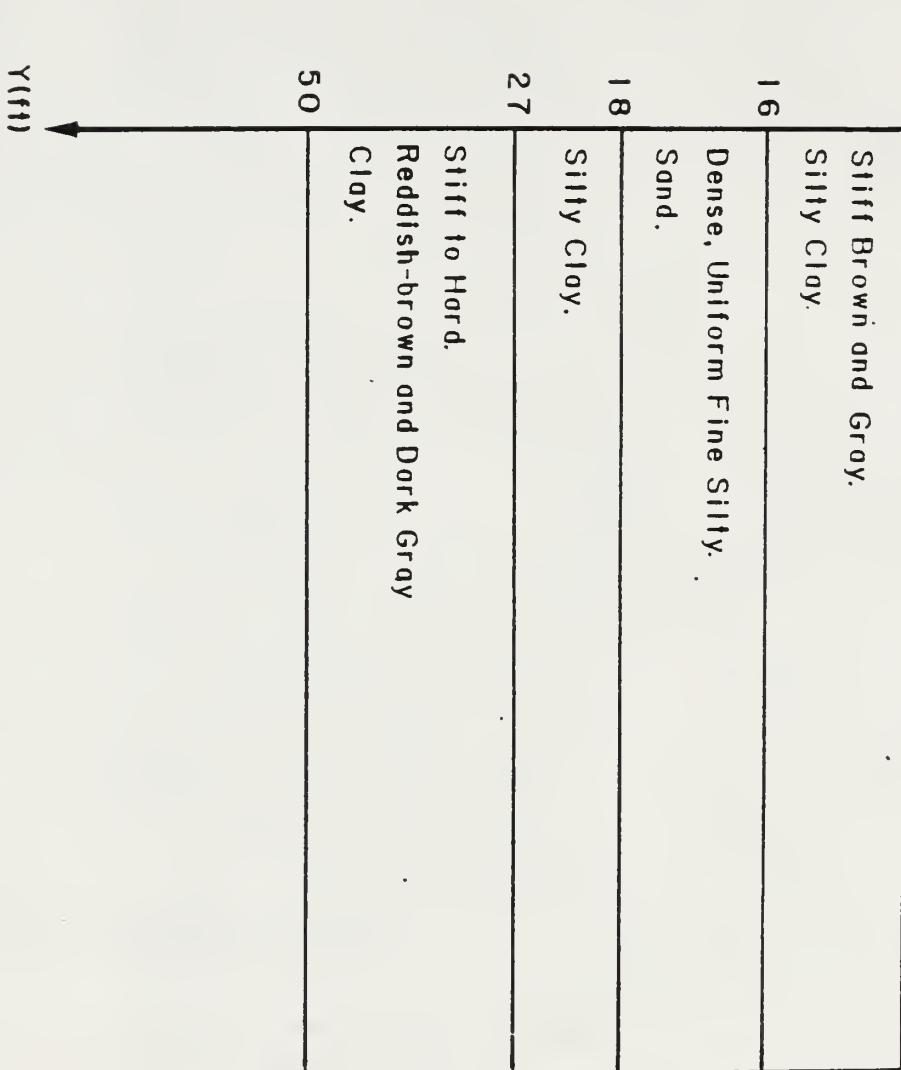


Fig. 4.31 Soil Conditions in Houston, Texas

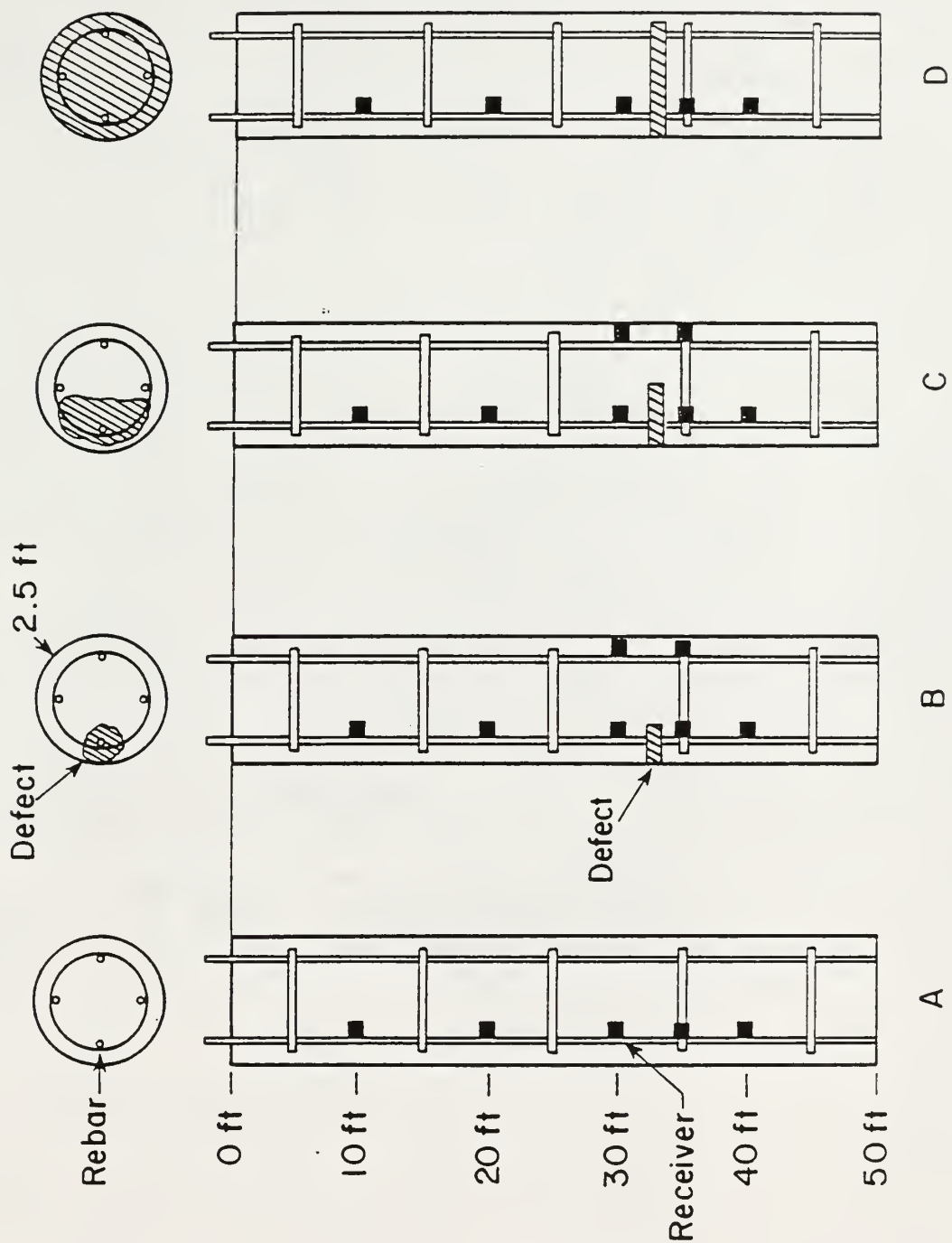


Fig. 4.32 Test Pile Dimensions

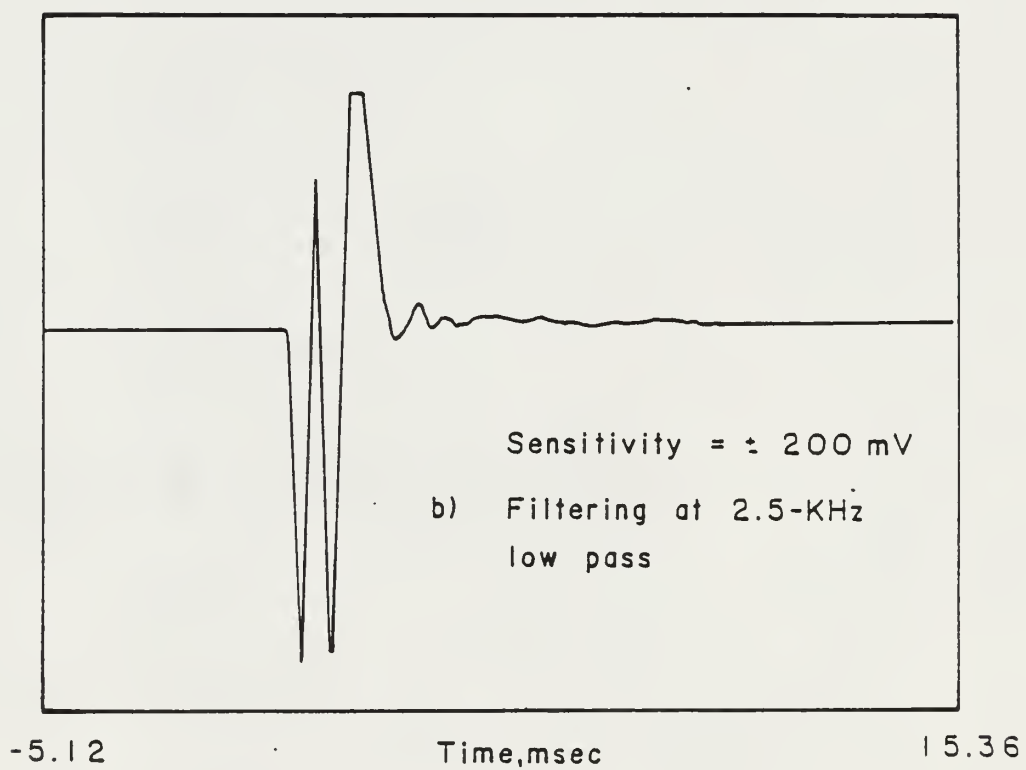


Fig. 4.33 Test Record for Pile A

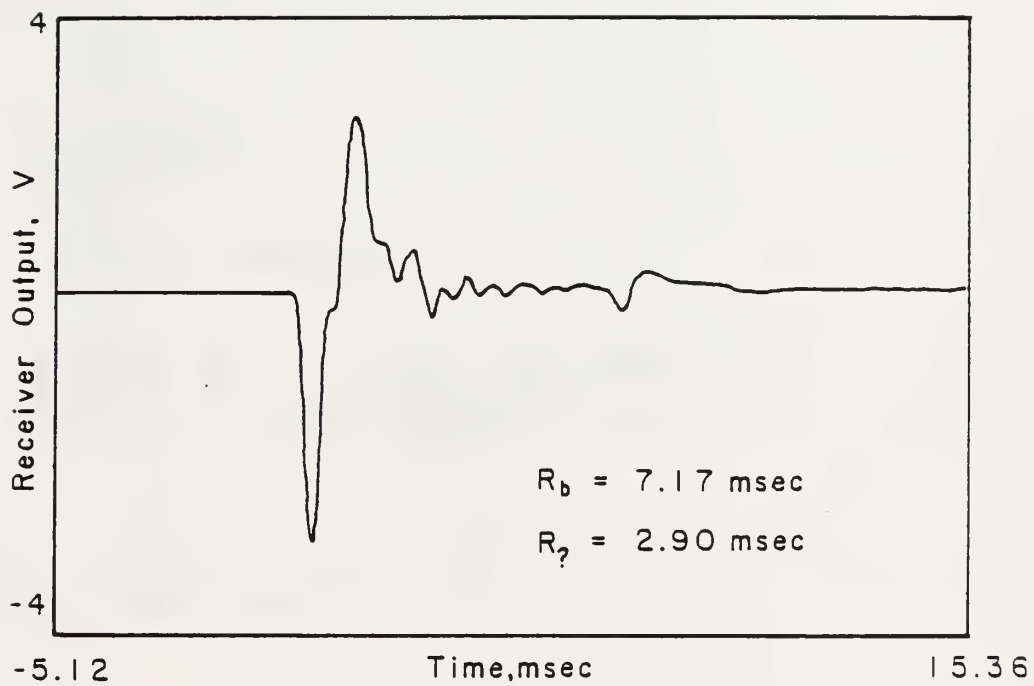


Fig. 4.34 Test Record for Pile B

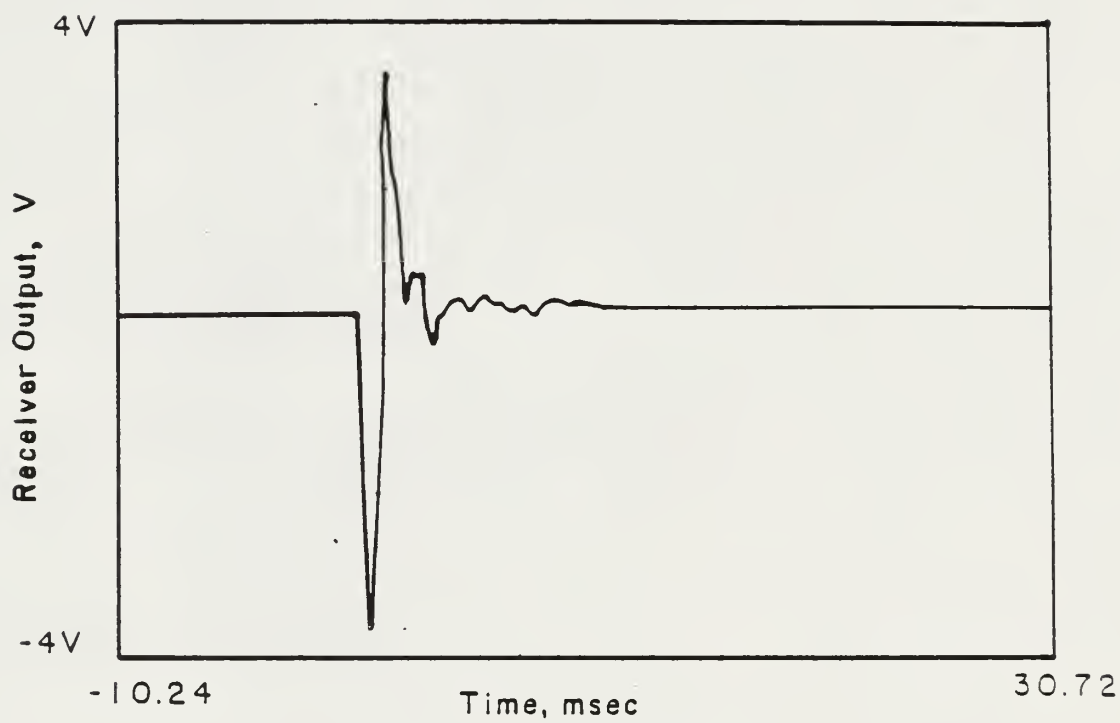


Fig. 4.35 Test Record for Pile C
(Drop Hammer)

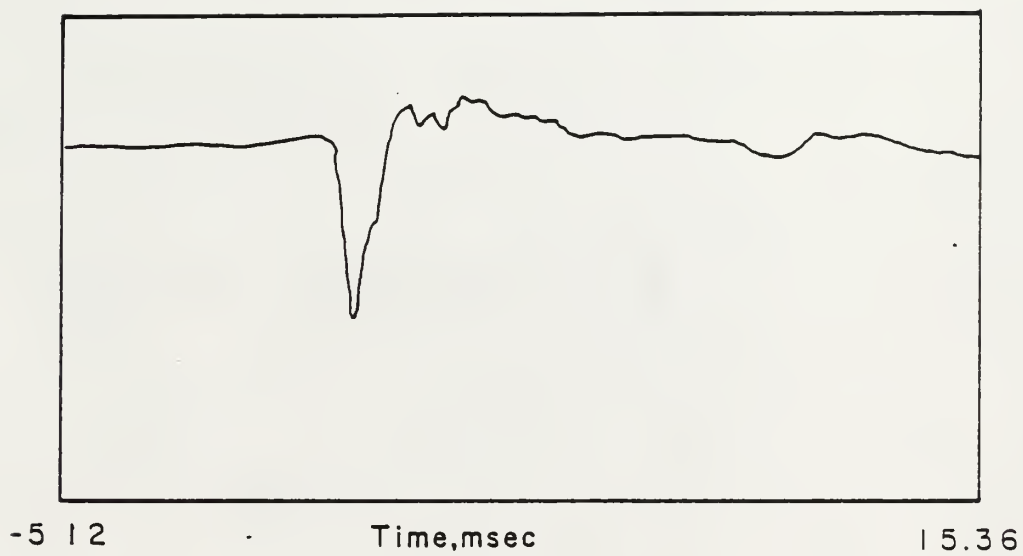


Fig. 4.36 Test Record for Pile C
(Hand Held Hammer)

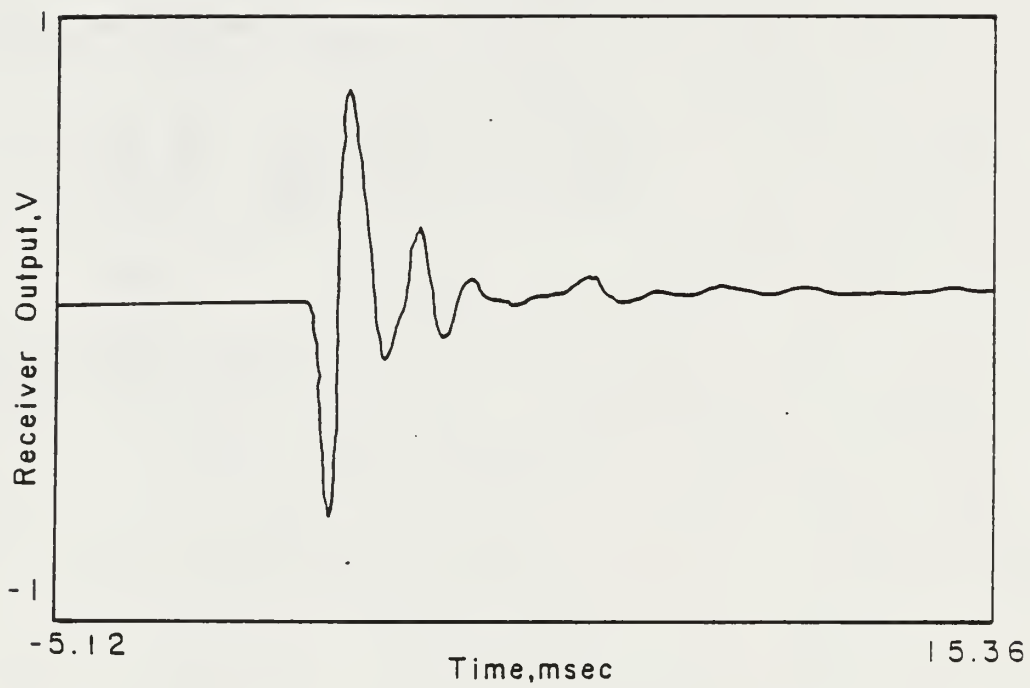


Fig. 4.37 Test Record for Pile D

GRL & Associates: Pile Integrity - PIT

Project: POWERHOUSE

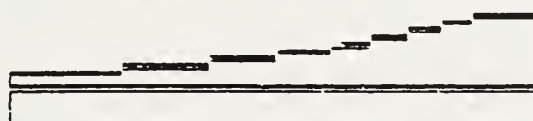
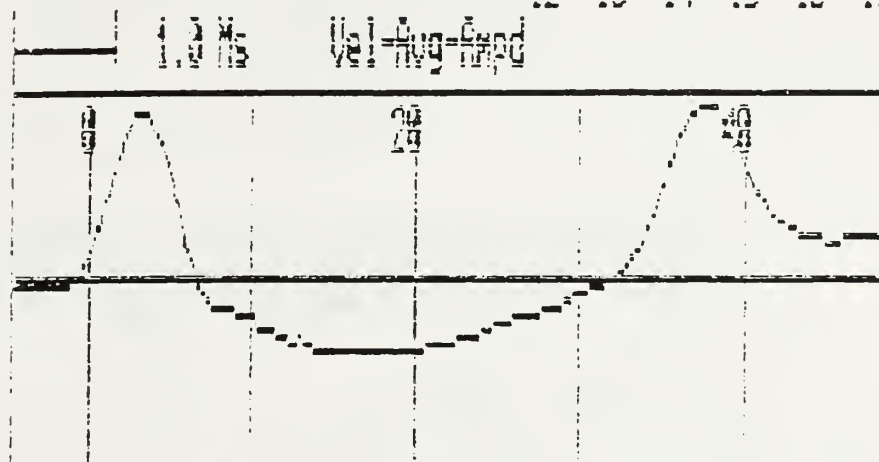
Pile: A1 EAST

Loc: FLA16

Date: 12/07/88

Avgd 7 Rls

12 13 14 15 16 17 18



Acc-Avg-Ampd

5.7
32.0 ft
12.5 ft/ms

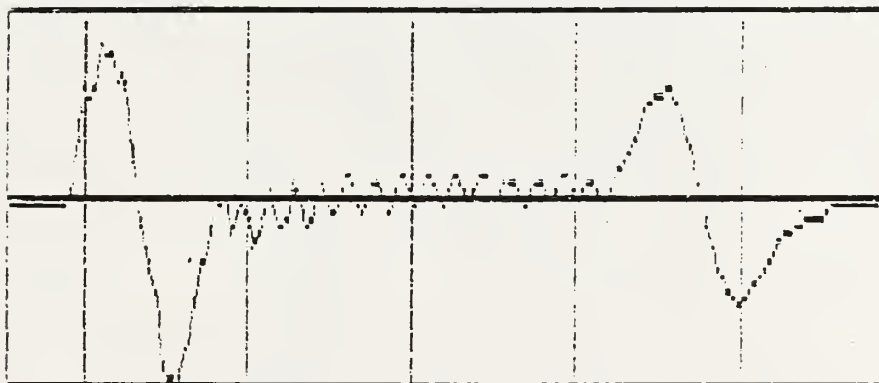


Fig.4.38 Test Record for Pile A1 EAST

GRL & Associates: Pile Integrity - PIT

Project: POWERHOUSE

Pile: C1 EAST

Loc: FLATS

Date: 12/07/88

Avgh 8 Bls

51 52 53 54 55 56 57 58

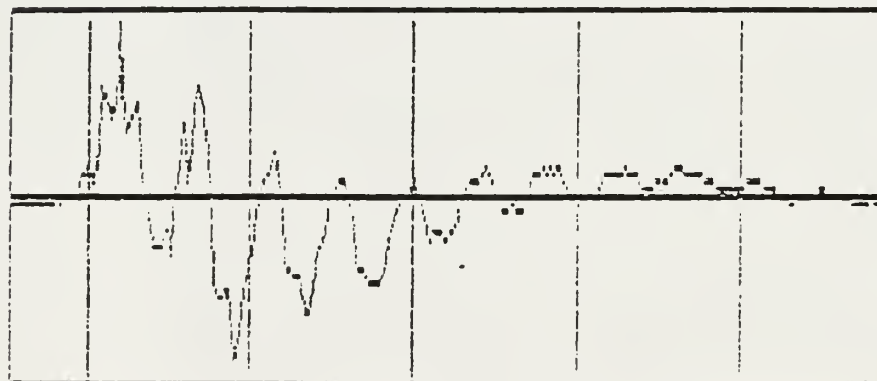
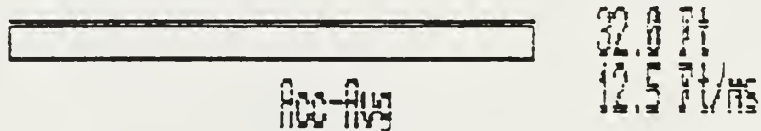
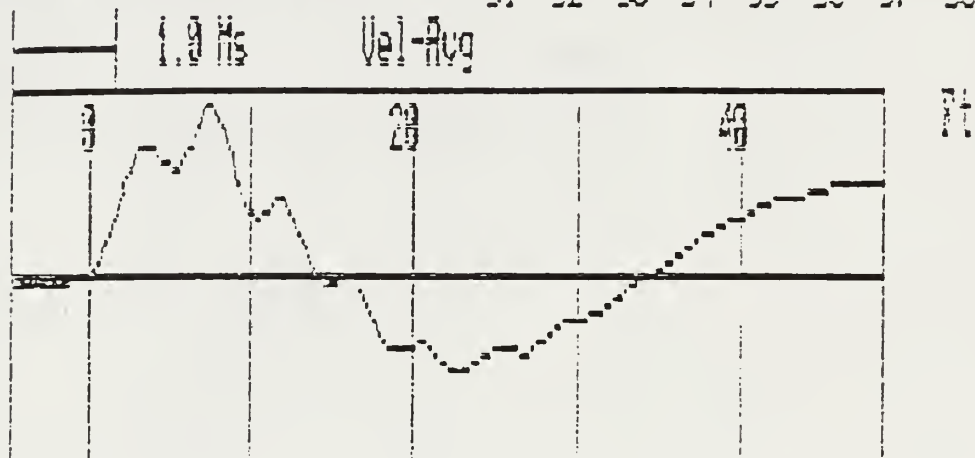


Fig. 4.39 Test Record for Pile C1 EAST

GRL & Associates: Pile Integrity - PIT

Project: POWERHOUSE

Pile:

E1 EAST

Loc:

PLATE

Date:

12/07/88

Run:

3 21s

78

79

80

81

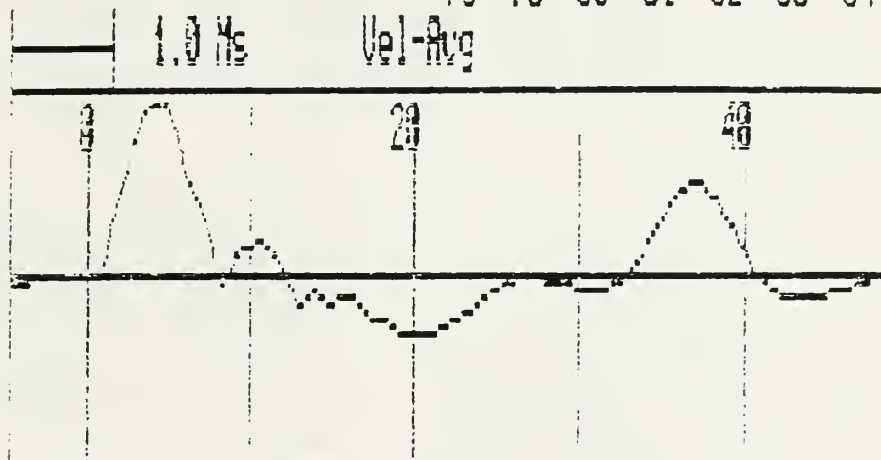
82

83

84

85

86



ft



Acc-Avg

32.0 ft

12.5 ft/ms

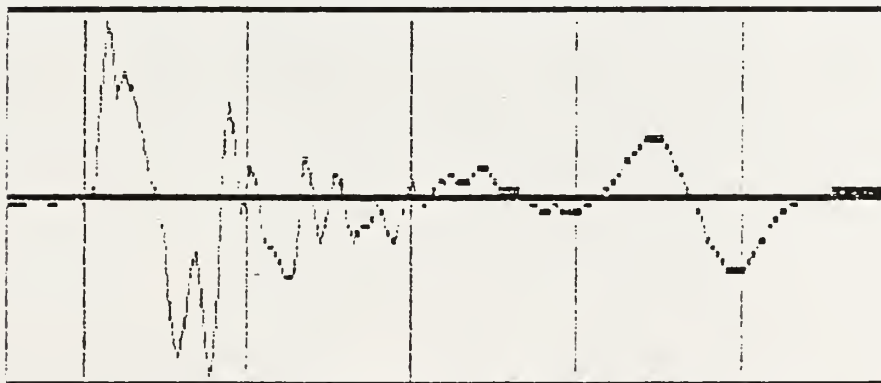


Fig. 4.40 Test Record for Pile E1 EAST

GRL & Associates: Pile Integrity - PIT

Project: POWERHOUSE

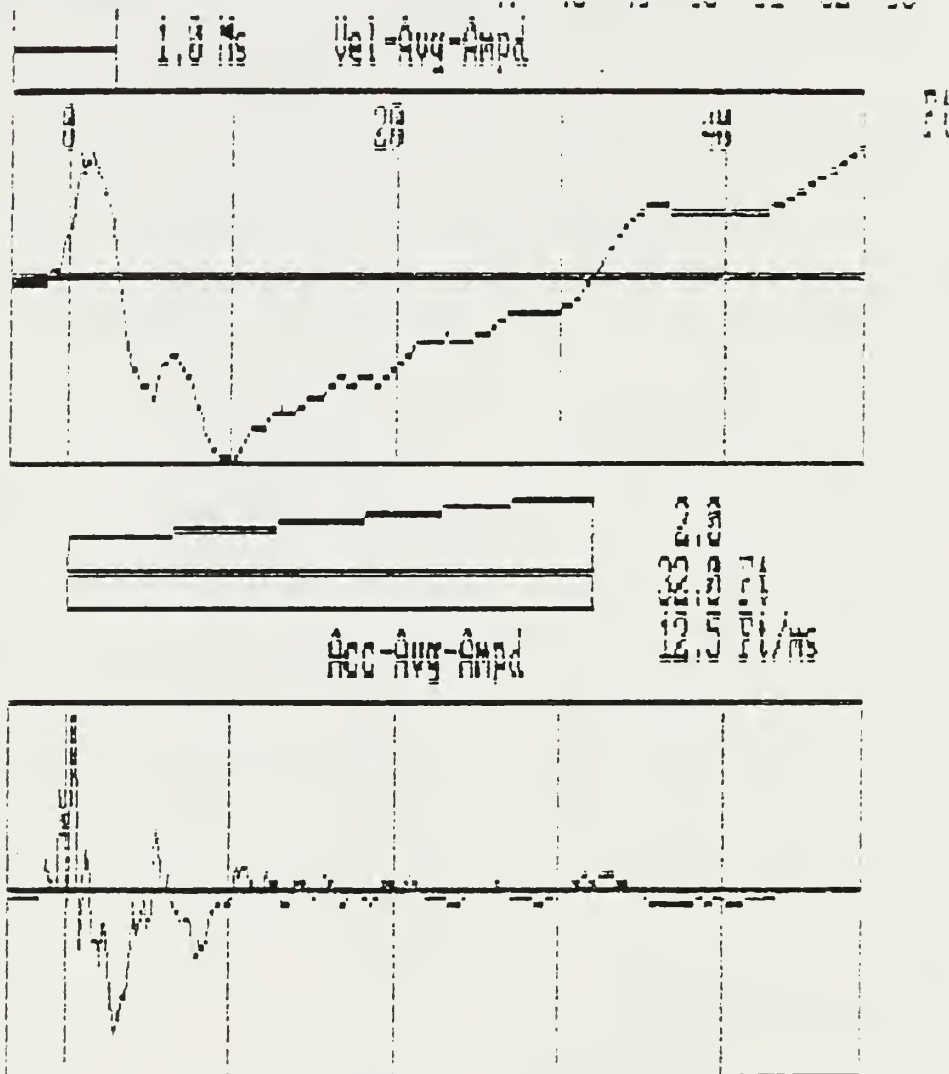
Pile: A4 3A

Lot: PLATS

Date: 12/07/68

Aug: 8 313

47 48 49 50 51 52 53 54



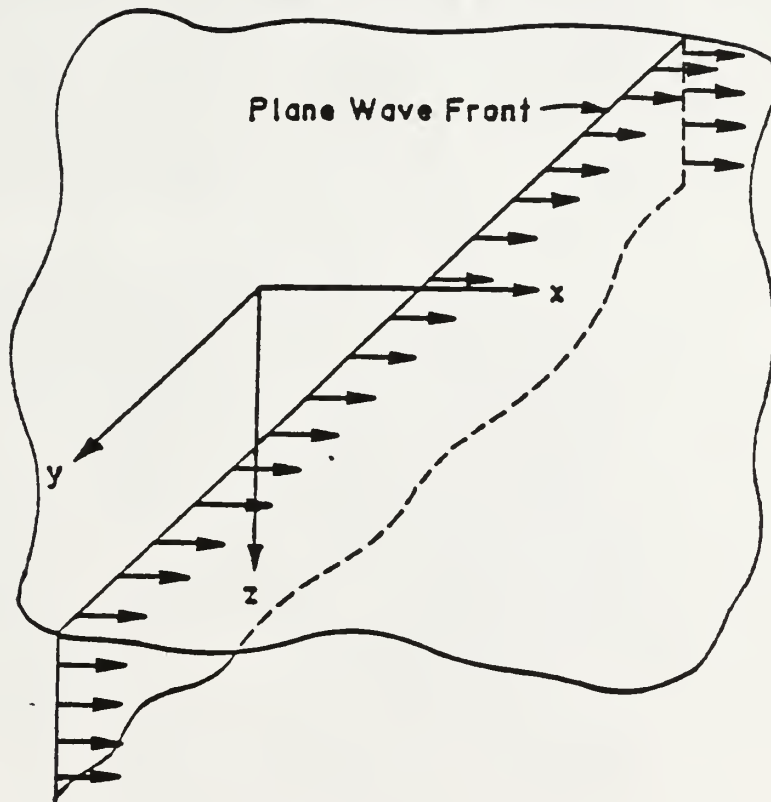


Fig. 5.1 Coordinate Convention for Elastic Half-Space

no1 Time s

1813

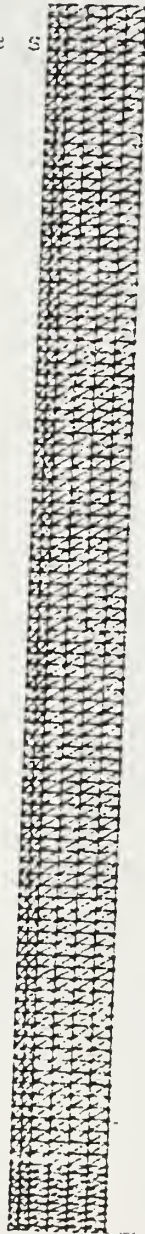


Fig. 5.2 Soil-Pile Interaction System

NODE NUMBER 377

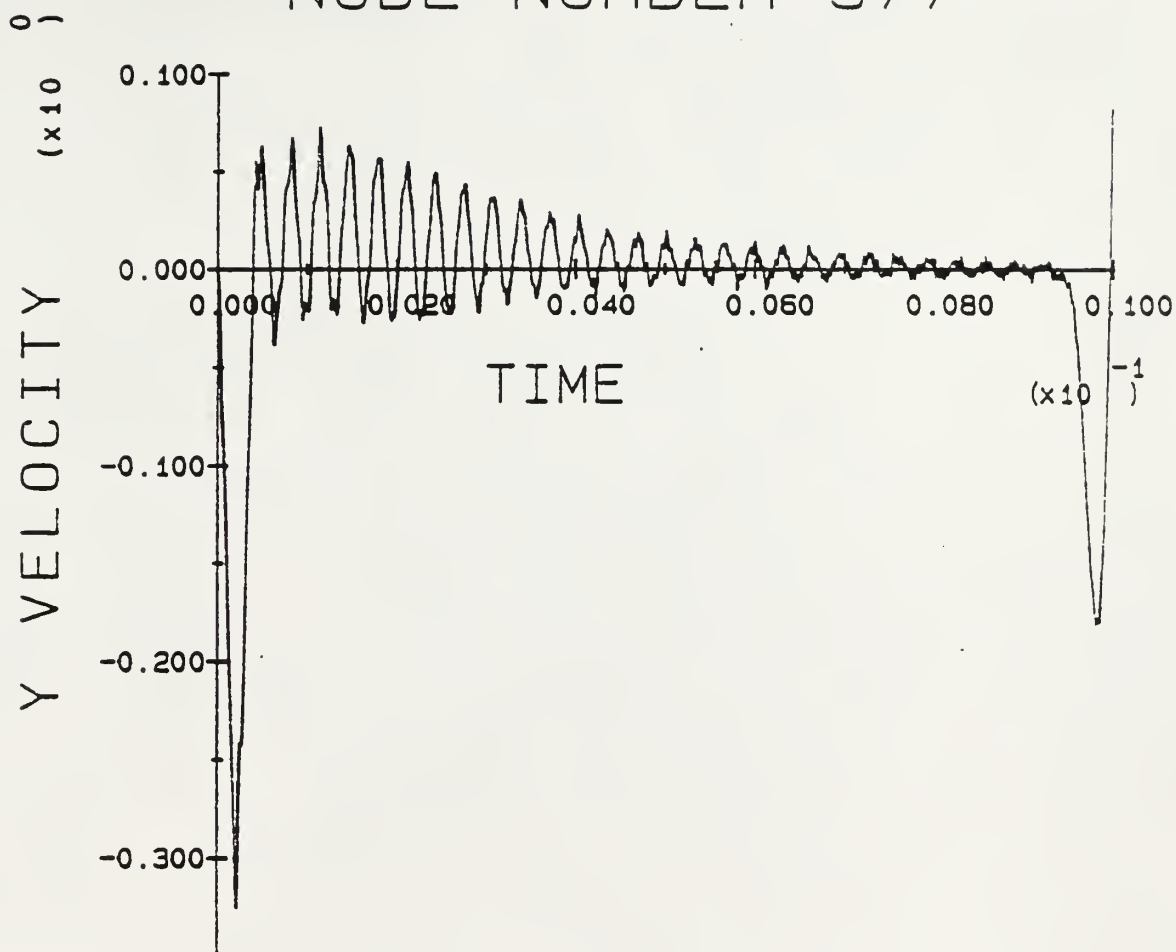


Fig. 5.3 Response on the Top of the Pile
Surrounds by Soil

NODE NUMBER 350

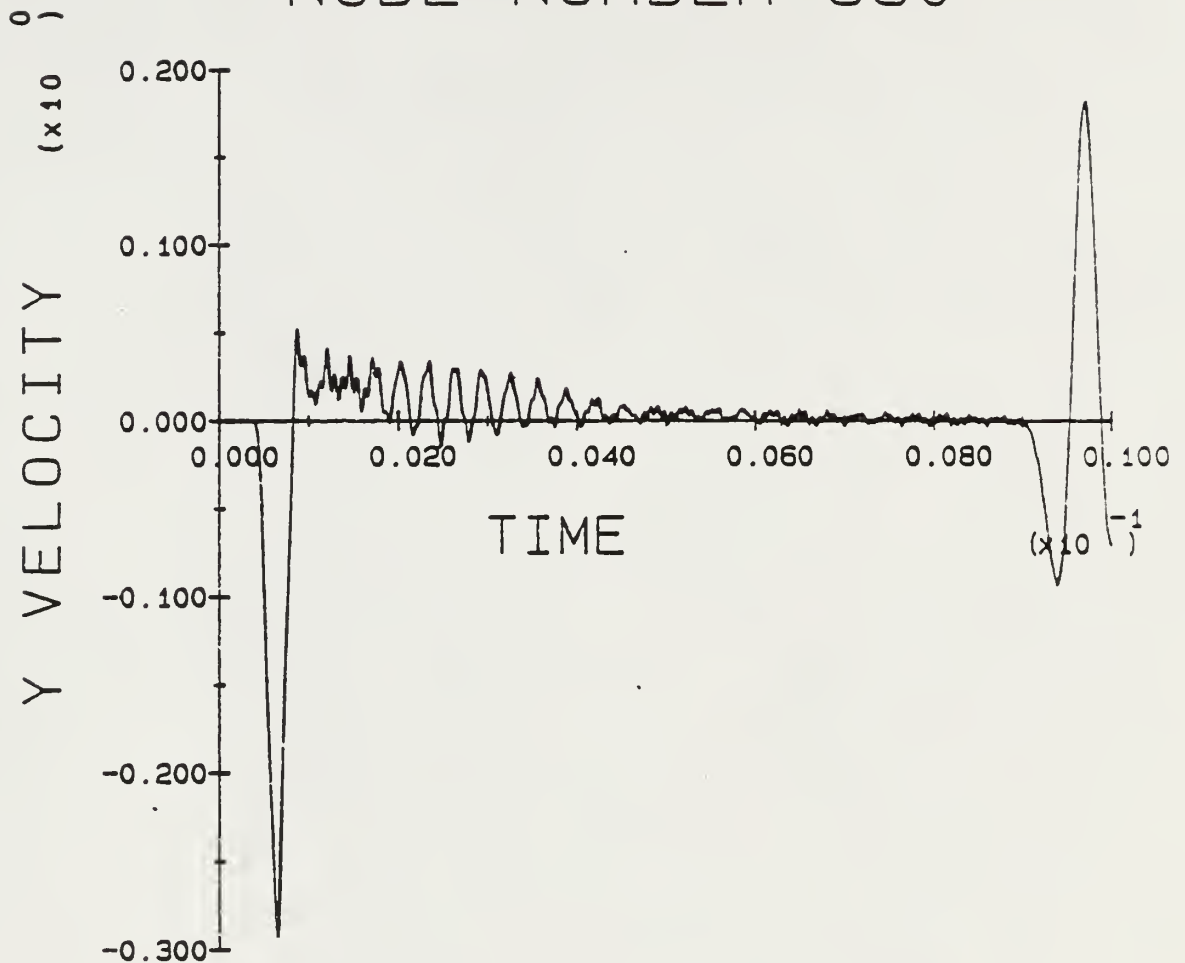


Fig. 5.4 Responce in the Depth 5 ft. (1.52m)
of the Pile Surrounded by Soil

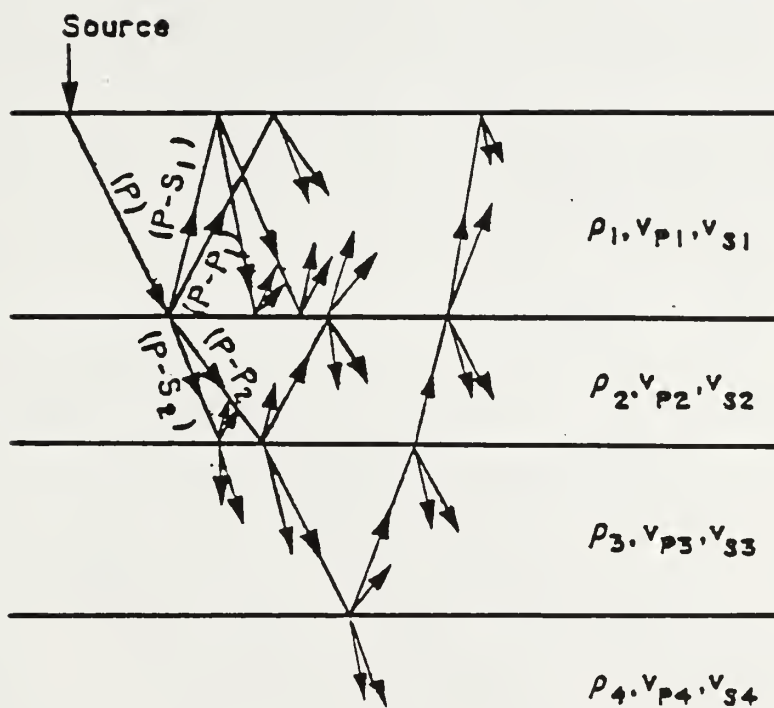


Fig. 5.5 Multiple Wave Reflections and Refractions
in a Layered Half-Space

NODE NUMBER 377

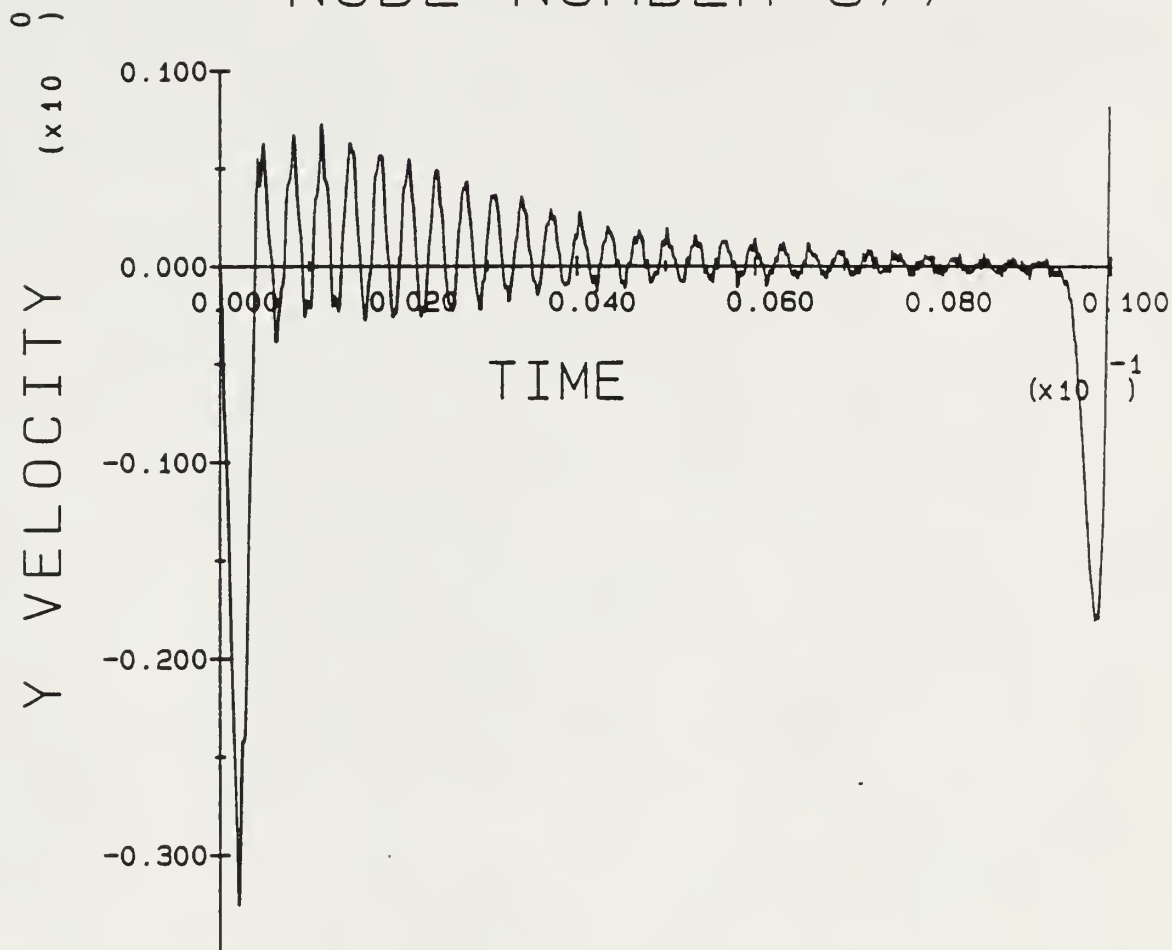
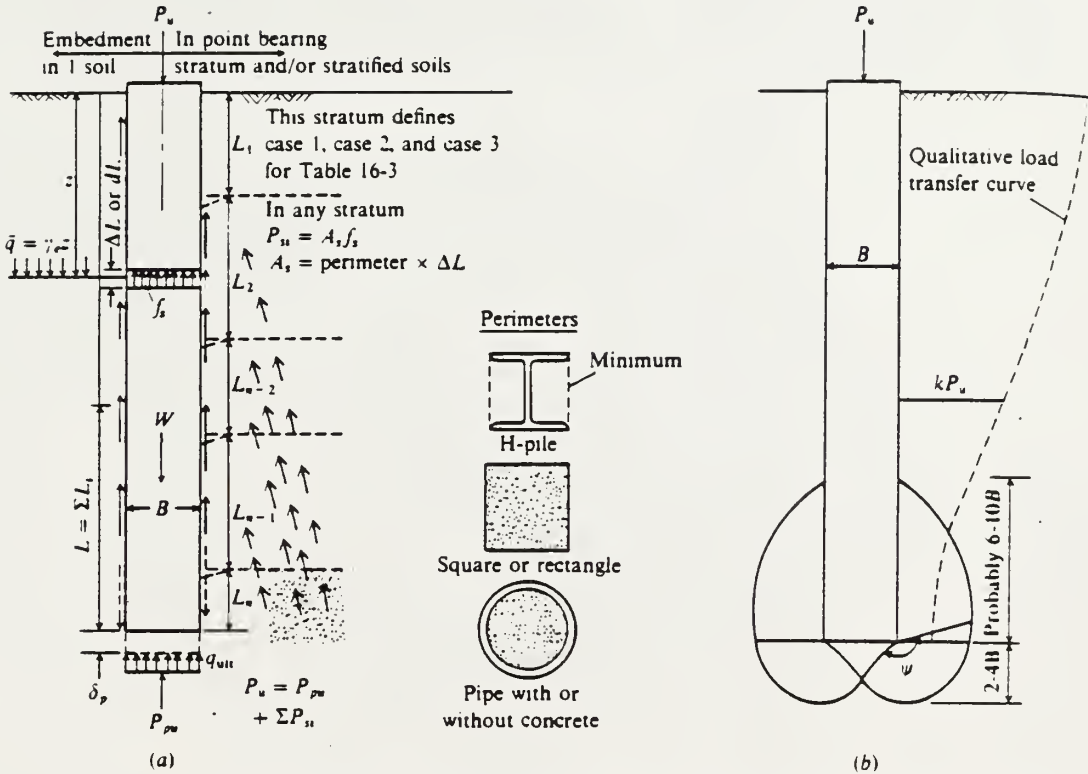


Fig. 5.6 Response on the Top of Pile
Surrounded by Layered Soil



(a) General development of pile capacity in either single or stratified soil mass; also pile permeability defined. (b) Qualitative zone of interest for ultimate point capacity.

Fig. 5.7 Shear Stress Acts Along the
Side Surface of a Pile

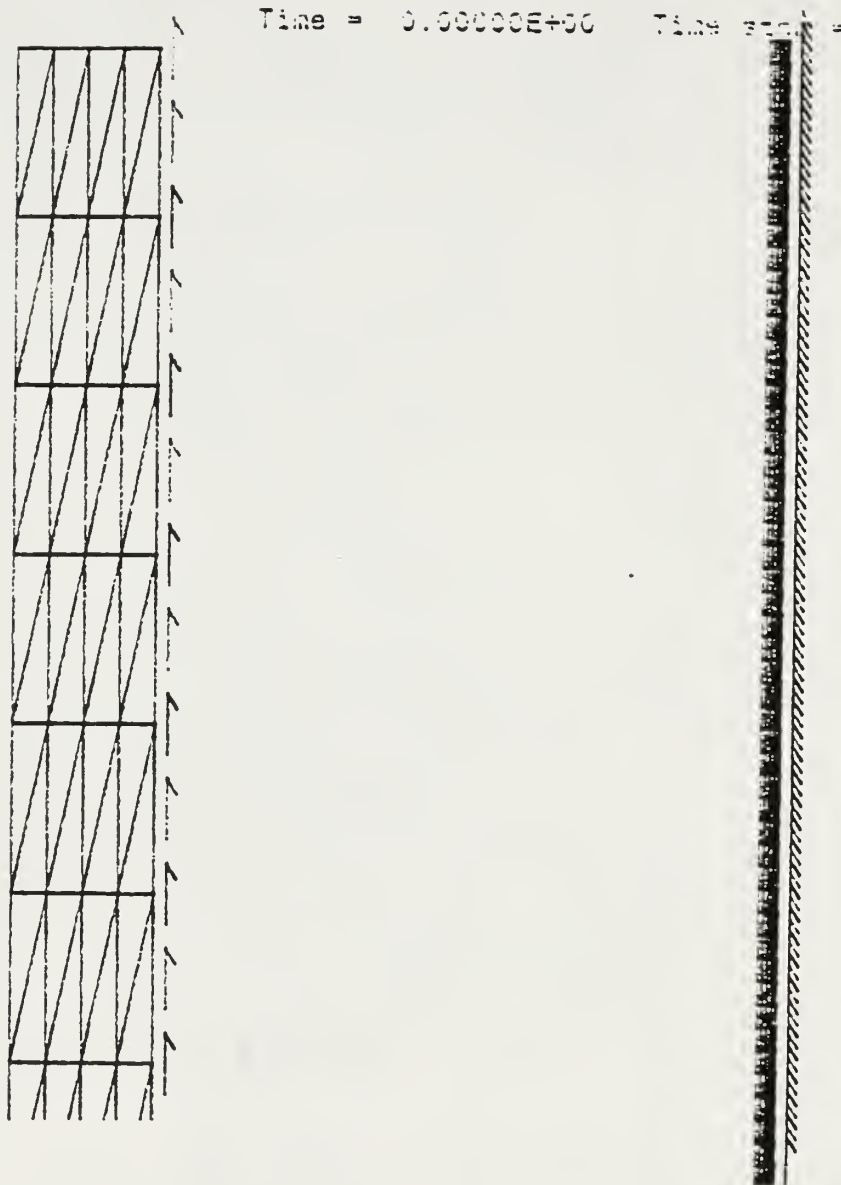


Fig.5.8 Mesh of Shear Stress

NODE NUMBER 255

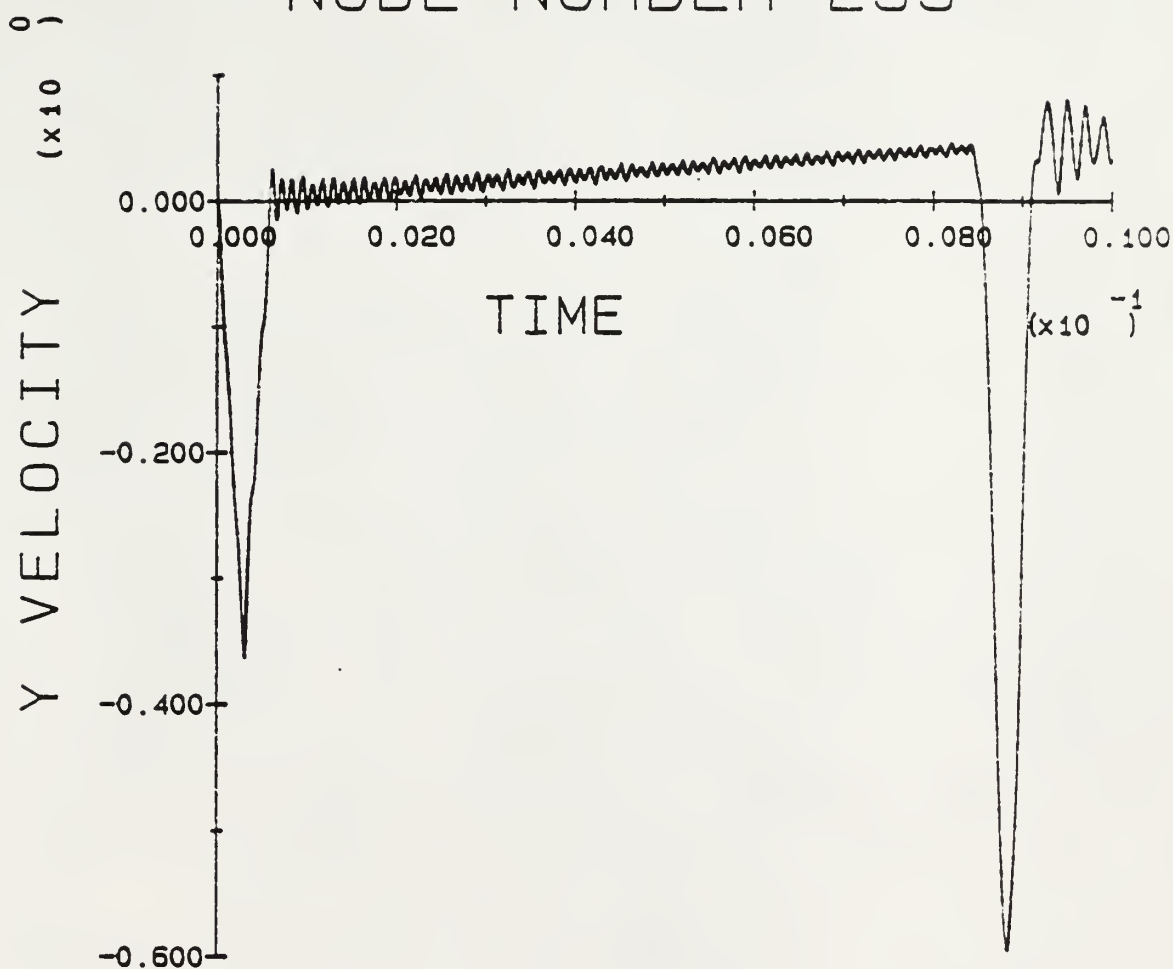


Fig. 5.9 Response on the Top of the Pile with Uniform Shear Stress 0.005 lb/in^2 (0.0344 KN/M^2) along the side surface

NODE NUMBER 255

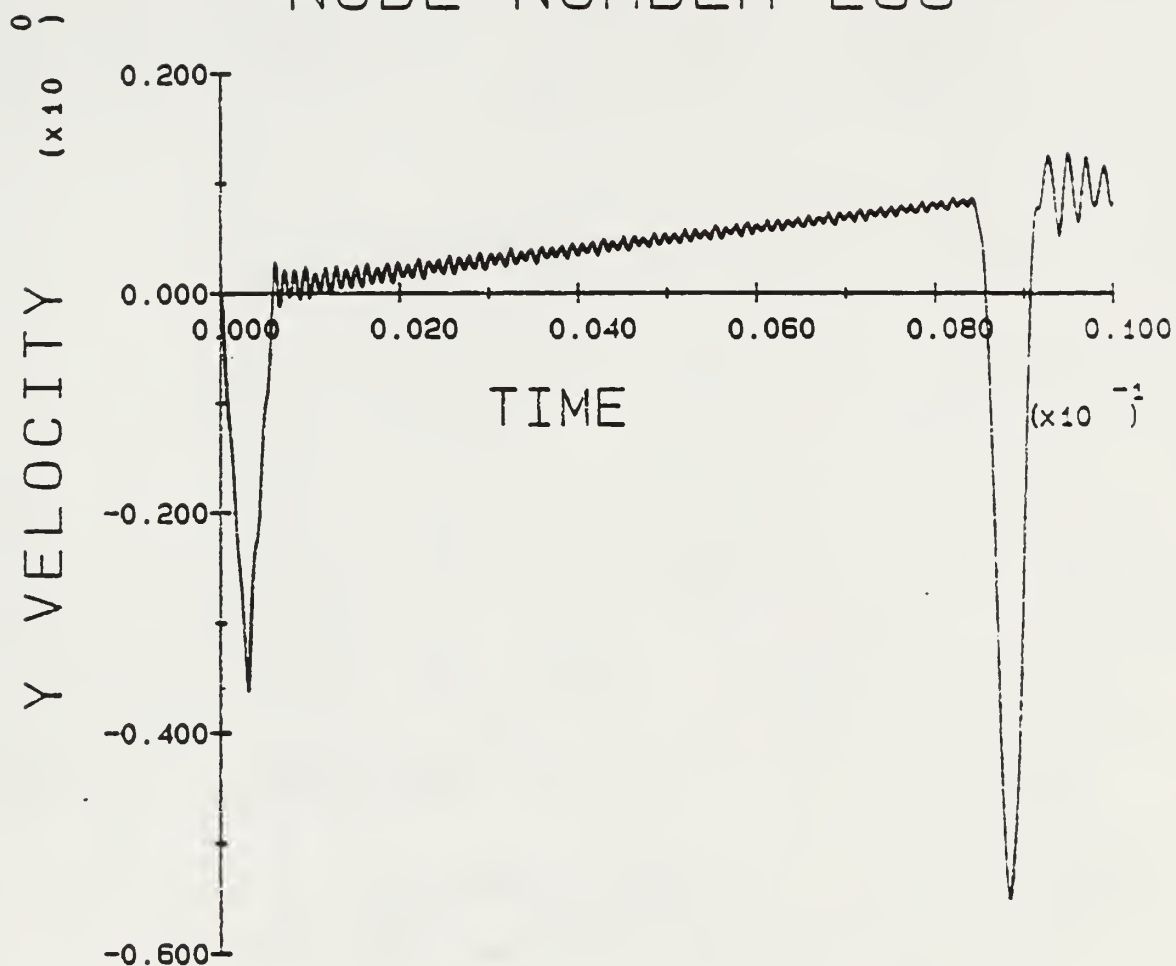


Fig. 5.10 Responce on the Top of the Pile with Uniform
Shear Stress 0.01 lb/in^2 (0.06895 KN/m^2)
Along the Side Surface

NODE NUMBER 255

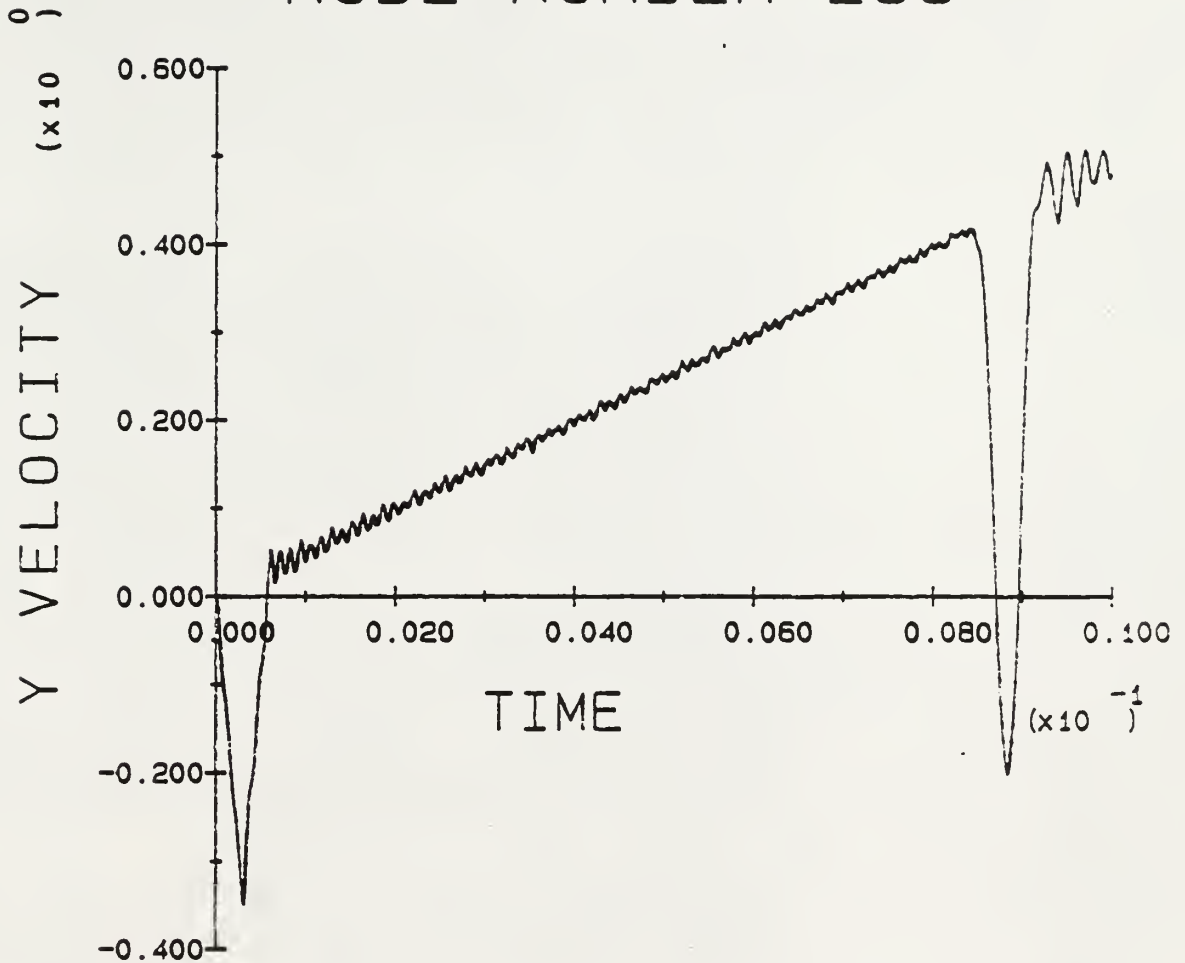


Fig. 5.11 Responce on the Top of the Pile with Uniform
Shear Stress 0.05 lb/in² (0.344 KN/M²)
Along the Side Surface

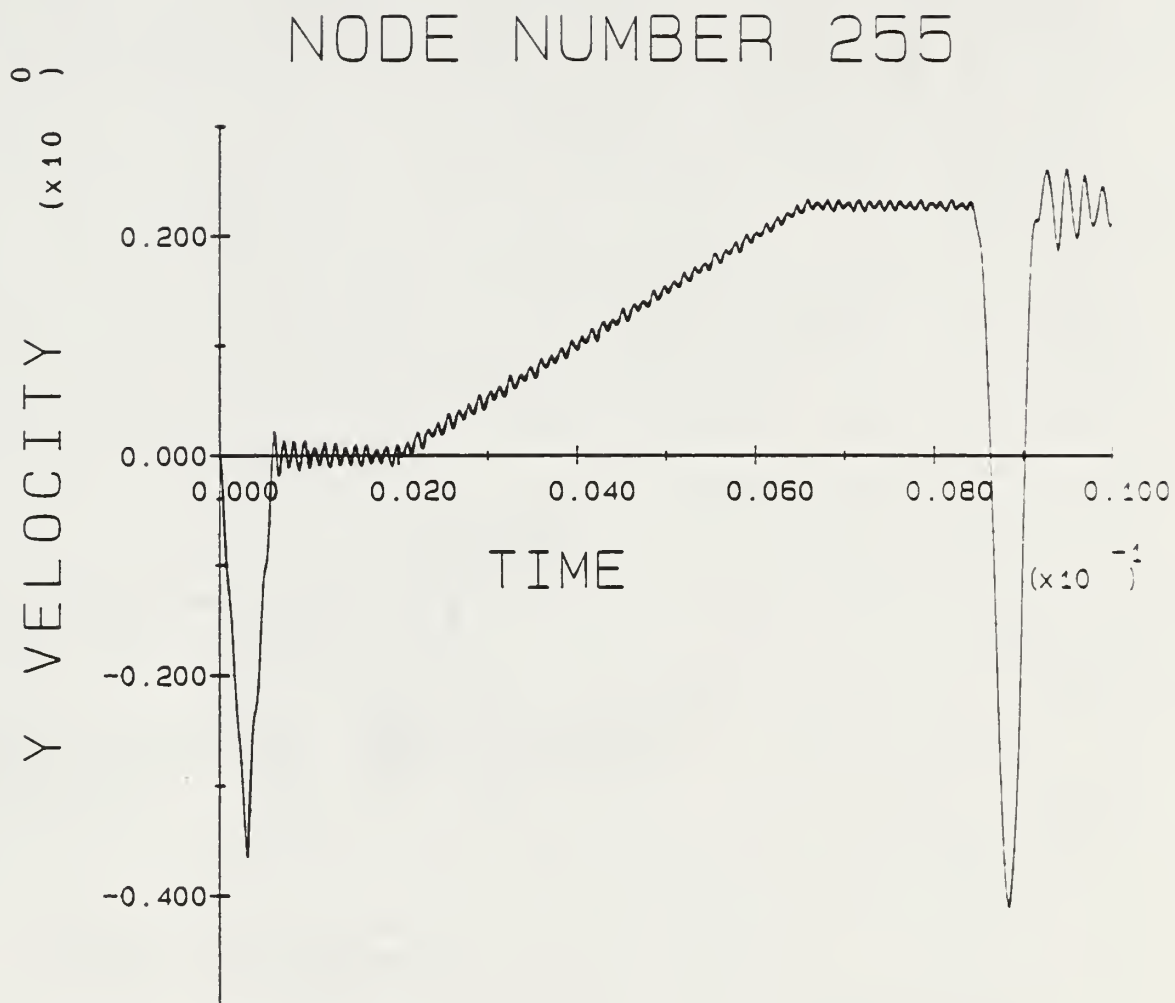


Fig. 5.12 Response on the Top of the Pile with Un-uniform Shear Stress Along the Side Surface

Time = 0.00000e+00

Time = 0.00000e+00

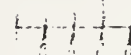
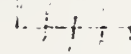
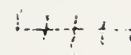
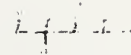
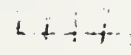
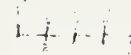


Fig. 5.13 Pile with 1/4 Defect in the
Cross Sectional Area

Time = 2.000000000 Time Elapsed 0



Fig. 5.14 Pile with 1/2 Defect in the
Cross Sectional Area

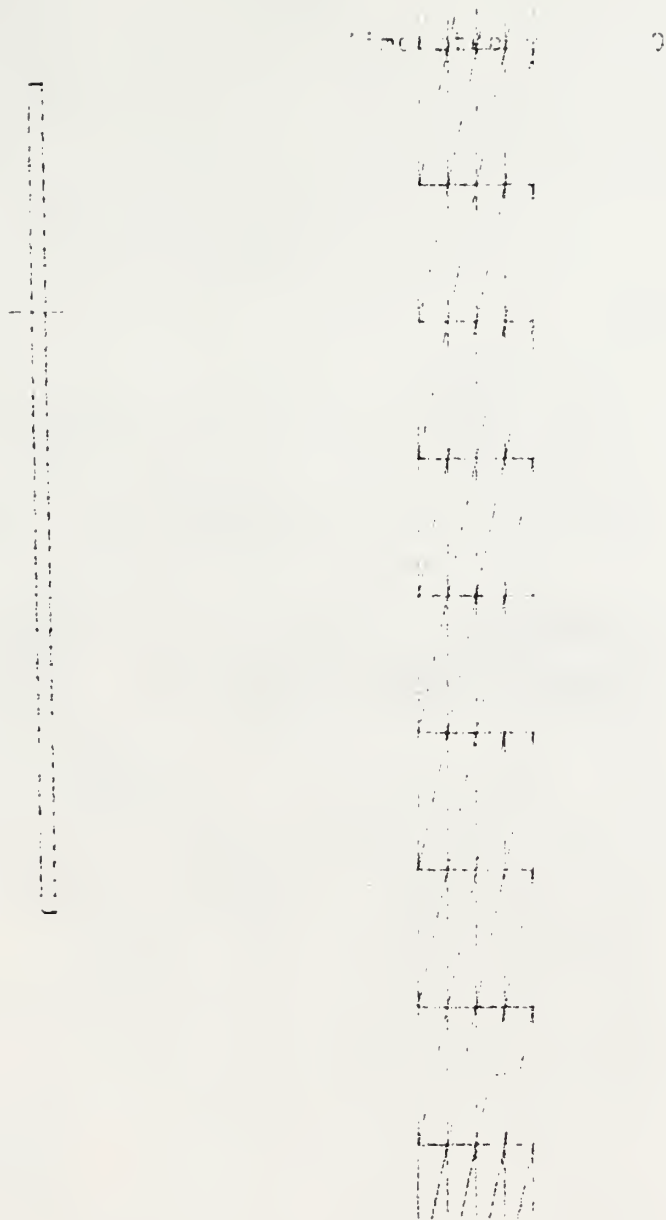


Fig. 5.15 Pile with $3/4$ Defect in the
Cross Sectional Area

Time = 0.000000e+00 Time Location



Fig. 5.16 Pile with Whole Defect in the
Cross Sectional Area

NODE NUMBER 255

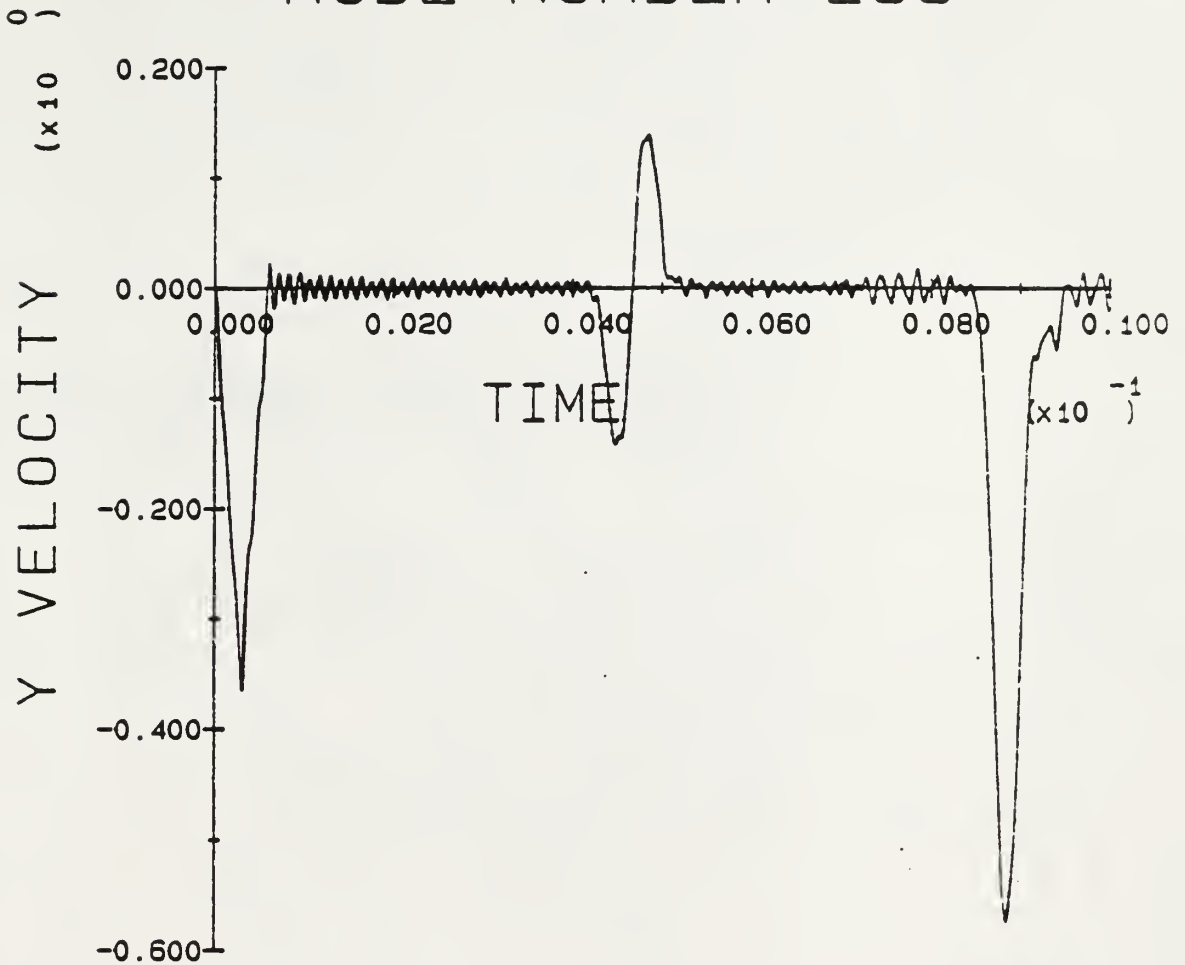


Fig. 5.17 Responce on the Top of the Pile with 1/4
Defect in the Cross Sectional Area

NODE NUMBER 255

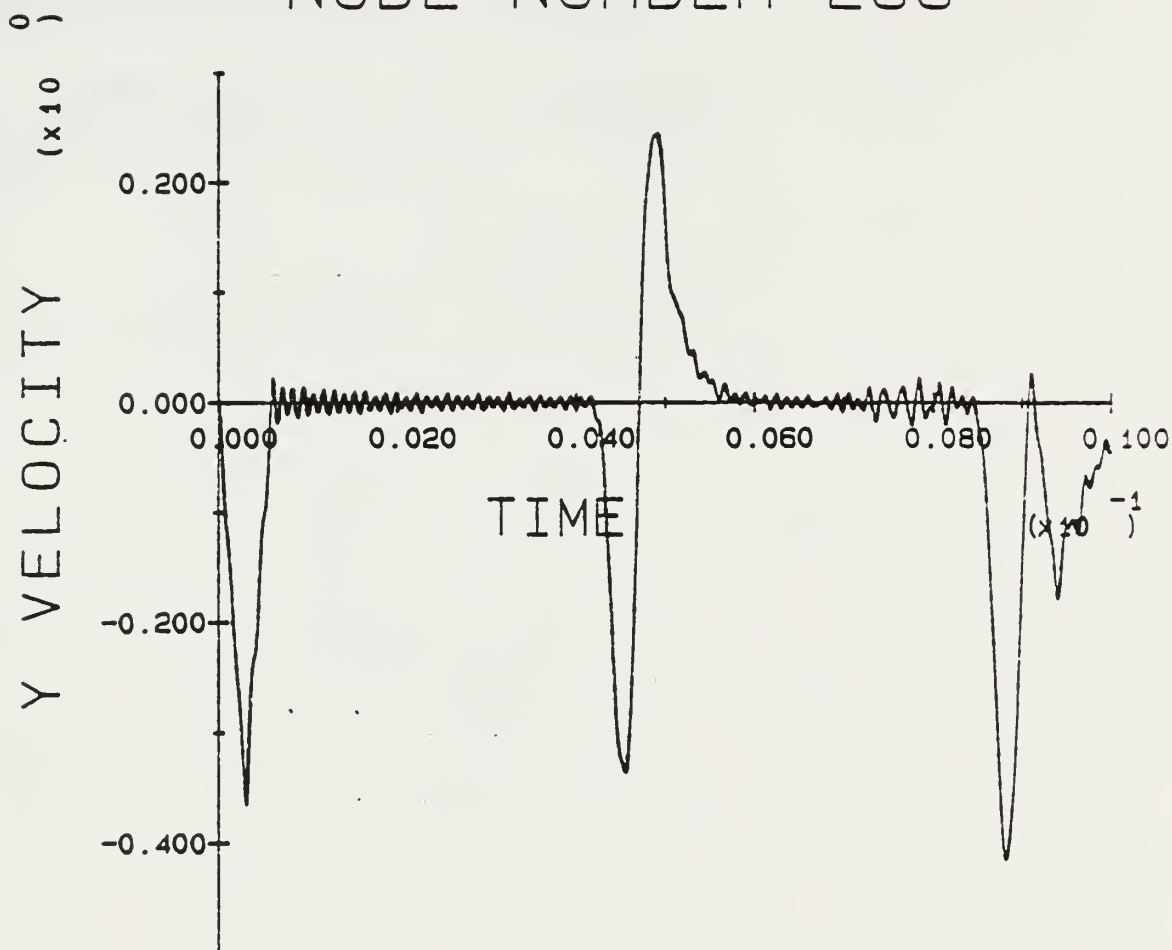


Fig. 5.18 Responce on the Top of the Pile with 1/2
Defect in the Cross Sectional Area

NODE NUMBER 255

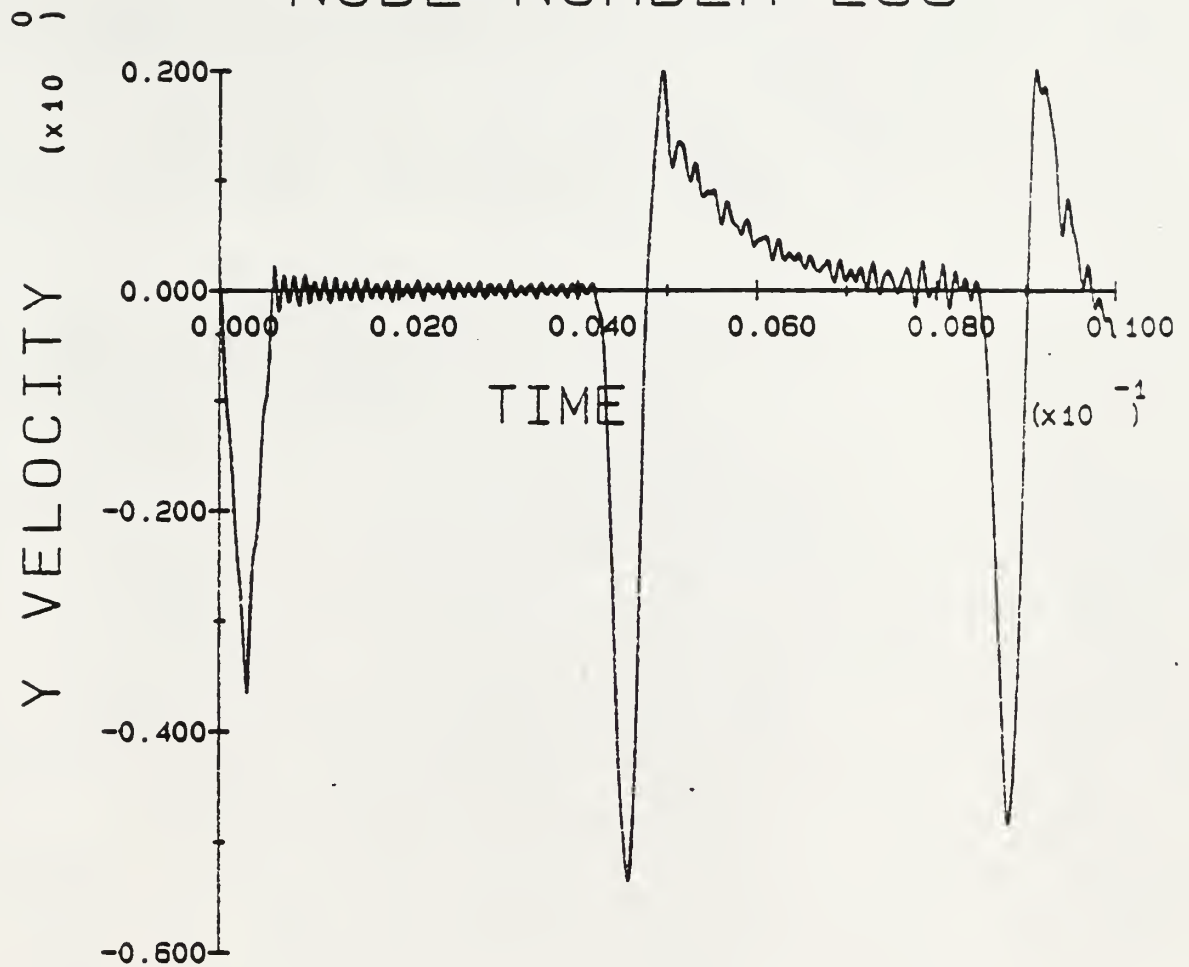


Fig. 5.19 Responce on the Top of the Pile with 3/4
Defect in the Cross Sectional Area

NODE NUMBER 255

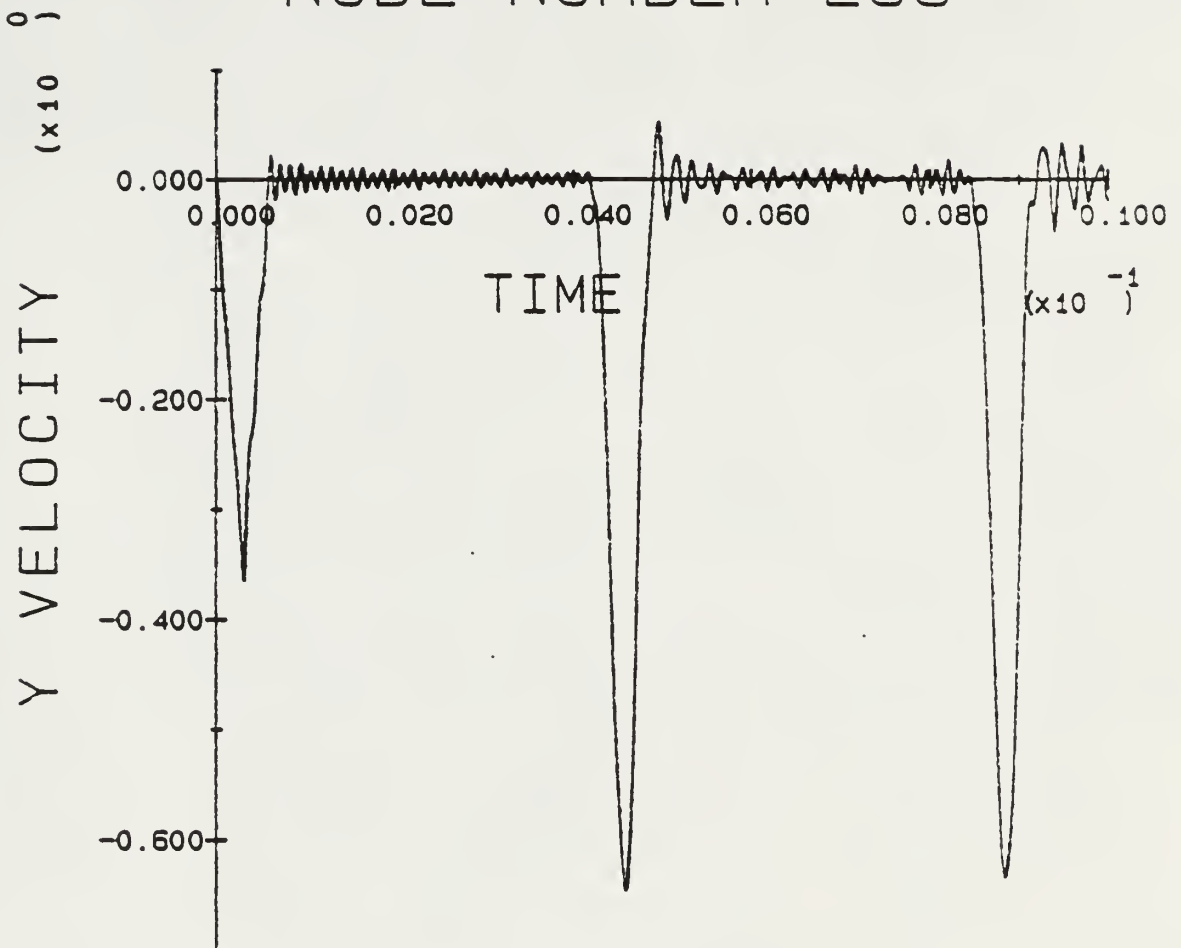


Fig.5.20 Responce on the Top of the Pile with Whole Defect in the Cross Sectional Area

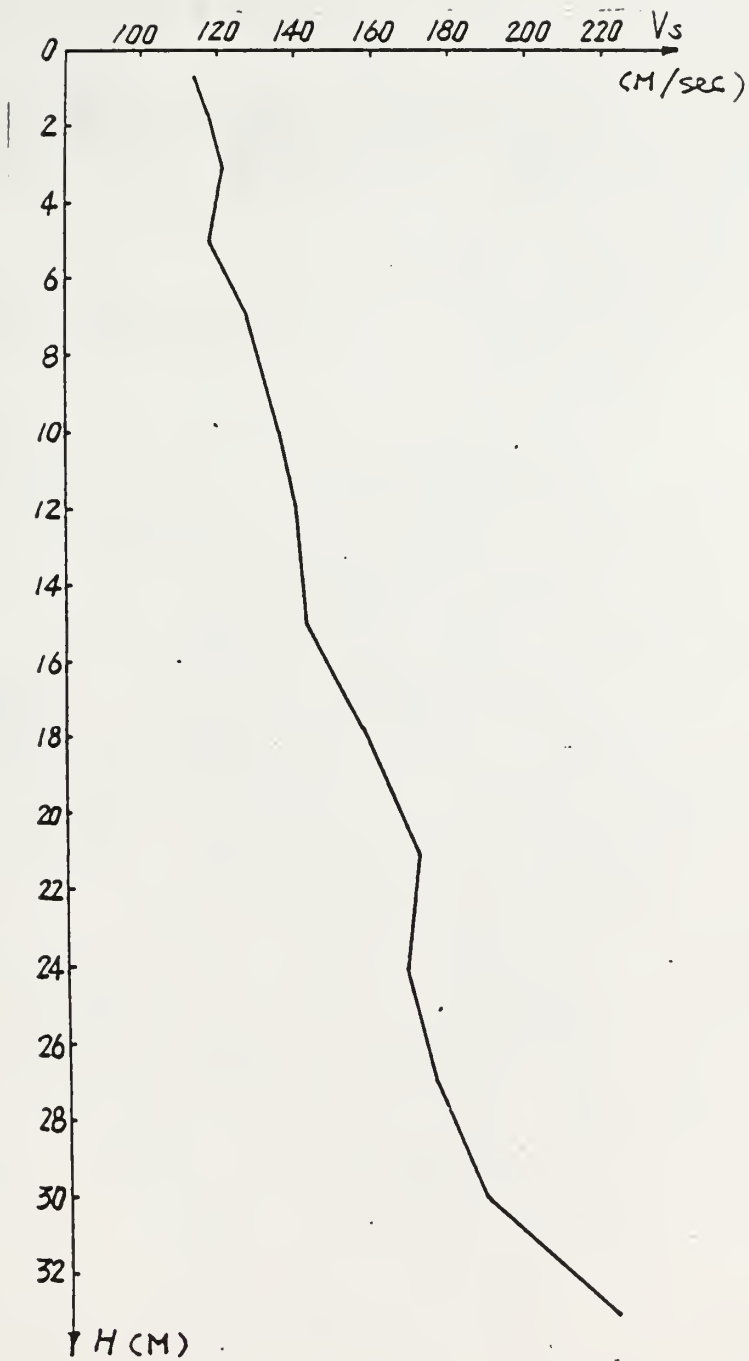


Fig. 5.21 Velocity of Shear Wave vs. Depth
(Up- Down Hole Method)

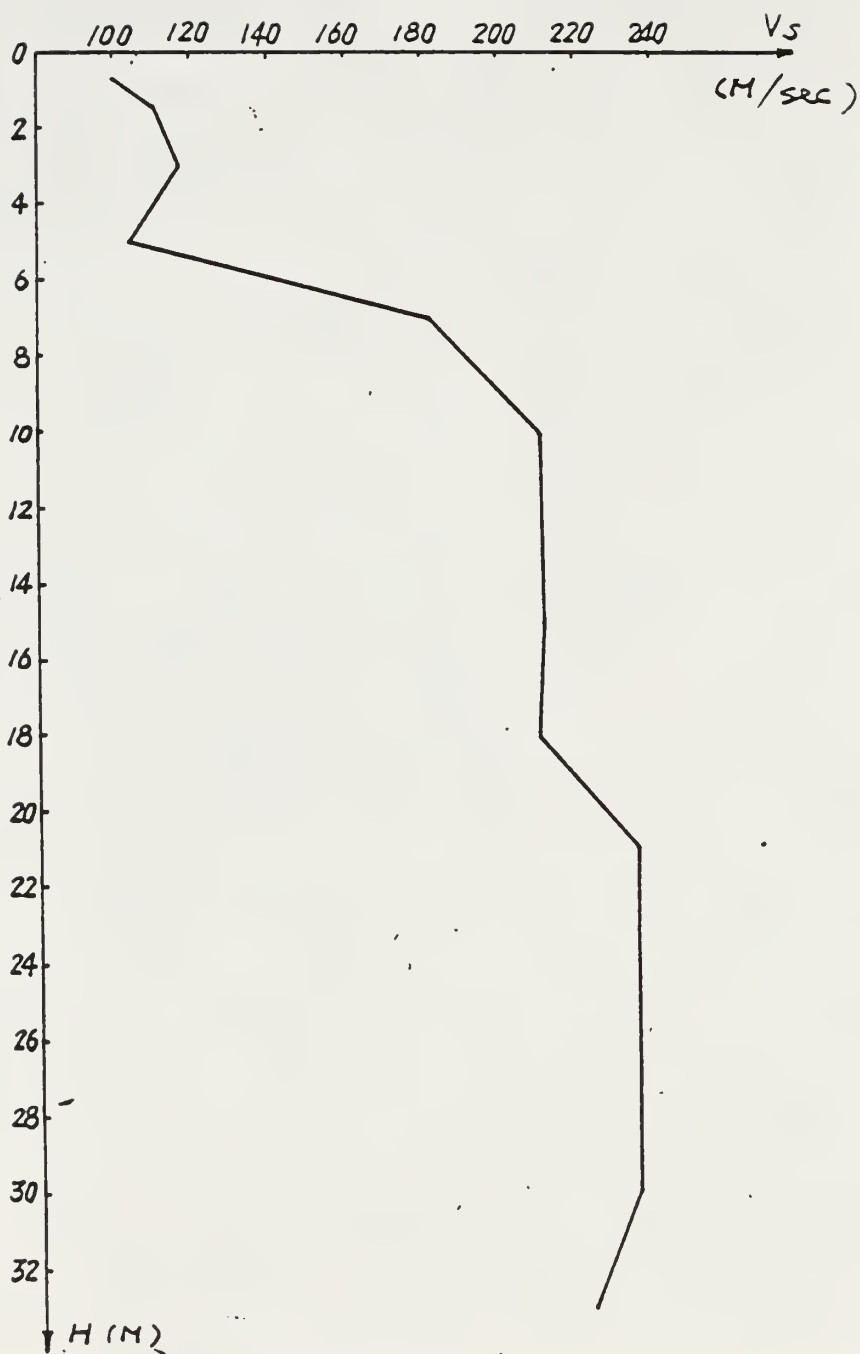


Fig. 5.22 Velocity of Shear Wave vs. Depth
(Cross Hole Method)

THE EFFECT FACTORS OF THE PILE INTEGRITY TEST

by

Xiaoming Zhu

B.S. Tongzi University, 1982

M.S. Tongzi University, 1985

AN ABSTRACT OF A THESIS

submitted in partial fulfillment of the
requirements for the degree

MASTER OF SCIENCE

Department of Civil Engineering
College of Engineering

KANSAS STATE UNIVERSITY

Manhattan, Kansas
1989

ABSTRACT

This paper applied the Finite Element Method to analyse the low strain pile integrity test, which is based on one-dimension wave propagation theory.

Meshing different pile-soil system, including load conditions, boundary conditions, material properties and changed cross-section area, the calculated results from two-dimension finite element methods are obtained by using CRACKER computer program.

The calculated results were compared with the test results from Ohio, New Jersey and Texas. Analysing the wave propagation, it was found that the surface wave noise and the friction between pile and soil are the most important effect factors. This explains the difference between the theory and the field test results of the piles. The wave velocity in the pile-soil system was found not to be a constant. A suggested formula is given in this paper which is closer to the measured wave velocity.

